UNIVERSITY OF CALIFORNIA, SAN DIEGO

# MULTISCALE COMPUTATIONAL MODELS OF TRANSMURAL HETEROGENEITIES AND VENTRICULAR ARRHYTHMOGENESIS

A dissertation submitted in partial satisfaction of the

requirements for the degree Doctor of Philosophy

in

Bioengineering

by

Sarah N. Flaim

Committee in charge:

Professor Andrew D. McCulloch, Chair
Professor Wayne R. Giles
Professor Michael J. Holst
Professor Sanjiv M. Narayan
Professor Jeffrey H. Omens

2006

The dissertation of Sarah N. Flaim is approved, and it is acceptable in quality and form for publication on microfilm:

_____

_____

_____

_____

_____

Chair

University of California, San Diego

2006

For Terry, Judy-Ann, and Bridget

"The hypotheses we accept ought to explain phenomena which we have observed. But they ought to do more than this: our hypotheses ought to **foretell** phenomena which have not yet been observed."

-*William Whewell (1794-1866) English mathematician, philosopher.*

# TABLE OF CONTENTS

# LIST OF FIGURES AND TABLES

# LIST OF ABBREVIATIONS

| | | | |
|---|---|---|---|
| APD | action potential duration | PLB | phospholamban |
| BCL | basic cycle length | RyR | ryanodine receptor |
| CaRU | calcium release unit | SCD | sudden cardiac death |
| CICR | calcium-induced calcium release | SERCA | SR $Ca^{2+}$ ATPase |
| DAD | delayed afterdepolarization | SQTS | short-QT syndrome |
| EAD | early afterdepolarization | SR | sarcoplasmic reticulum |
| ECC | excitation-contraction coupling | TDR | transmural dispersion of repolarization |
| ECG | electrocardiogram | VF | ventricular fibrillation |
| Endo | endocardium | | |
| Epi | epicardium | $Ca^{2+}$ | calcium |
| FE | finite element | $Cl^-$ | chloride |
| Iso | isoproteronol | $K^+$ | potassium |
| KChIP | $K^+$ Channel-Interacting Protein | $Na^+$ | sodium |
| LCC | L-type $Ca^{2+}$ channel | $I_{CaL}$ | L-type $Ca^{2+}$ current |
| LQTS | long-QT syndrome | $I_{Kr}$ | rapidly actifying delayed rectifier current |
| LV | left ventricle | $I_{Ks}$ | slowly activating delayed rectifier current |
| M | midmyocardium | $I_{Kv43}$ | transient outward $K^+$ current |
| NE | norepinephrine | $I_{Na}$ | $Na^+$ current |
| ODE | ordinary differential equation | $I_{NaCa}$ | $Na^+$ $Ca^{2+}$ exchanger current |
| PDE | partial differential equation | $I_{NaL}$ | late or persistent $Na^+$ current |
| PKA | protein kinase A | $I_{to1}$ | transient outward $K^+$ current |

# ACKNOWLEDGEMENTS

Over the last five years, I have benefitted from the help and support of many people, to whom I owe far more gratitude than I can possibly express here. Firstly, I would like to sincerely thank my advisor, Andrew McCulloch. None of this work would have been possible without his enthusiastic mentorship, outstanding intellectual ability and creativity, and occasional whip-cracking that all helped to focus my project and get this dissertation "PhinishD". Thanks also to Wayne Giles, who knows more about cardiac ion channels than I thought was humanly possible, for many insightful and often entertaining discussions of the literature and its contributors. I am also extremely grateful to the other members of my thesis committee: Jeff Omens, Sanjiv Narayan and Mike Holst for their willingness to provide advice. To my earliest teachers of all, my parents, I owe the greatest thanks; their love of learning has inspired me all along.

I am very grateful for the financial support of the US Fulbright Foundation, the New Zealand Government and the American Heart Association. Funding for various conferences was also generously gifted by the Society for Industrial Applied Mathematics, the Gordon Research Conferences and the Bioengineering Institute at the University of Auckland.

During the transition from the lecture theaters to the lab, I discovered that scientific research can be fraught with frustrations and reward isn't always imminent and certainly never instantaneous. I truly appreciate the help and friendship of those who eased the way: other members, past and present, of the Cardiac Mechanics Research Group at UCSD, and all my friends and fellow-students (too many to mention by name) in the Department of Bioengineering. In particular, I would like to

thank Bob Mills, Hunaid Gurji, Jeff Saucerman, Roy Kerckhoffs, Mary Ellen Belik, Jyoti Rao and Kathy Lu for many fascinating discussions and collaborations. A special thanks to Fred Lionetti, Curtis Jensen and Drew Schaffner for their amazing technical support and without whom Continuity would still be back in the dark ages. To my sister Bridget, thank you for your love, support and for our many humorous conversations on Google Chat.

Above all, and as always, my profoundest thanks to my loving, patient, incomparable husband, Chris.

I acknowledge the following journals for granting reprint permissions. Part of the text of Chapter 1 is a reprint of the material as it appears in, "Computational models of cardiac electromechanics" by Roy Kerckhoffs, Sarah Healy, Taras Usyk and Andrew McCulloch in the Proceedings of the IEEE, 94: 769-783, 2006. Copyright © 2006 by IEEE. Reprinted with permission from IEEE.

Part of the text of Chapter 2 is a reprint of the material as it appears in, "Proarrhythmic Consequences of a KCNQ1 AKAP-Binding Domain Mutation: Computational Models of Whole Cells and Heterogeneous Tissue" by Jeffrey Saucerman, Sarah Healy, Mary Ellen Belik, Jose Puglisi and Andrew McCulloch in Circulation Research, Vol 95(12):1216-24, 2004. Copyright © 2004 by Lippencott Williams & Wilkins. Reprinted with permission from Lippincott Williams & Wilkins.

The text of Chapter 3, entitled "Arrhythmogenic consequences of asynchrony and heterogeneity in cardiac myocytes during $\beta_1$-adrenergic stimulation" by Sarah Flaim, Jeffrey Saucerman, and Andrew McCulloch is a reprint of the material as it was submitted to Circulation Research.

The text of Chapter 4, entitled "Contributions of sustained $I_{NaL}$ and $I_{Kv43}$ to heterogeneity of early repolarization and arrhythmogenesis in canine left ventricular myocytes" by Sarah Flaim, Wayne Giles and Andrew McCulloch is a reprint of the

material as it was submitted to the American Journal of Physiology (Heart and Circulation). The dissertation author conducted the research and was the author of these excerpts/manuscripts.

# VITA

| | |
|---|---|
| 2001 | B.E (Hons). University of Auckland, New Zealand |
| 2003 | M.S., University of California, San Diego |
| 2006 | Ph.D., University of California, San Diego |

## AWARDS

- American Heart Association Predoctoral Fellowship (2005-2006)
- Joel Drillings Award for Outstanding Achievement in Cardiovascular Research (2005)
- SIAM Travel Award Winner (Dynamical Systems Meeting, 2005)
- SIAM Travel Award Winner (Annual Meeting, 2004)
- Jacobs School of Engineering Research Review Poster and Library Award (2004)
- New Zealand Government Top Achiever Doctoral Fellowship (2002-2005)
- Fulbright Graduate Fellowship (2001-2002)

## JOURNAL ARTICLES

**Flaim SN**, McCulloch AD. "Computational modeling of arrhythmia formation in an LQT3 *SCN5A* mutation: From genetic mutation to clinical phenotype" (in preparation)

**Flaim SN**, Giles WR, McCulloch AD. "Contributions of sustained $I_{Na}$ and $I_{Kv43}$ to transmural heterogeneity of early repolarization and arrhythmogenesis in canine left ventricular myocytes" (under revision)

**Healy SN**, Saucerman JJ, McCulloch AD. "Arrhythmogenic consequences of asynchrony and heterogeneity in cardiac myocytes during $\beta_1$-adrenergic stimulation" (under revision)

Kerckhoffs RCP, **Healy SN**, Usyk TP, McCulloch AD. "Computational methods for cardiac electromechanics" *P IEEE.* 94: 769-783 (2006)

**Healy SN**, McCulloch AD. "An ionic model of stretch-activated and stretch-modulated currents in rabbit ventricular myocytes" *Europace* Suppl 2:128-34 (2005)

Saucerman JJ, **Healy SN**, Belik ME, Puglisi JL, McCulloch AD. "Proarrhythmic consequences of a KCNQ1 AKAP-binding domain mutation: computational models of whole cells and heterogeneous tissue" *Circ Res* 95(12):1216-24 (2005)

## SELECTED ABSTRACTS AND PRESENTATIONS

**Healy SN**, McCulloch AD "Repolarization abnormalities due to remodeling of $Na^+$-$Ca^{2+}$ exchange gradient in failing hearts" Biophysical Society 50th Annual Meeting, Salt Lake City, UT (2006)

Kaiser T, **Healy SN**, Brieger L. "Using a generalized MPI interface for Python, MyMPI". Scientific Python Meeting, Pasadena, CA (2005)

**Healy SN**, McCulloch AD. "Contributions of cellular and structural heterogeneity to rabbit ventricular arrhythmia". SIAM Meeting on Dynamical Systems, Snowbird, UT (2005)

**Healy SN**, Mills RW, Gurji HA, Usyk T, McCulloch AD "A 3D gating law for stretch-activated currents in the rabbit left ventricle" International Union of Physiological Sciences, San Diego, CA (2005)

**Healy SN**, Saucerman JJ, McCulloch AD "Increased arrhythmic risk during dynamic phosphorylation changes following $\beta_1$-adrenergic stimulation" Computational Physiology: from Genome to Physiome (IUPS Satellite Meeting), San Diego, CA (2005)

**Healy SN**, Saucerman JJ, McCulloch AD "Proarrhythmic effects of a KCNQ1 gene mutation in a 3D model of rabbit ventricular tissue with cellular heterogeneities" Gordon Research Conference on Cardiac Arrhythmia Mechanisms, Buellton, CA (2005)

**Healy SN**, Mills RW, Gurji HA, Usyk T, McCulloch AD "A 3D gating law for stretch-activated currents in the rabbit left ventricle" Biophys J 88: 301a-301a Biophysical Society 49th Annual Meeting, Long Beach, CA (2005)

Saucerman JJ, **Healy SN**, McCulloch AD "Modeling the proarrhythmic effects of a KCNQ1 gene mutation" Biophys J. 88: 474a-474a Biophysical Society 49th Annual Meeting, Long Beach, CA (2005)

**Healy SN**, McCulloch AD. "Computational methods for modeling structural and functional interactions in the heart". SIAM Annual Meeting, Portland, OR (2004)

**Healy SN**, Belik ME, Michailova A, Puglisi JL, Bers DM, McCulloch AD. "3D simulation of action potential heterogeneity in rabbit ventricular tissue" Biophys J. 86: 299a-299a, Biophysical Society 48th Annual Meeting, Baltimore, MD (2004)

**Healy SN**, Belik ME, Puglisi JL, Bers DM, McCulloch AD "High performance computational modelling of transmural action potential heterogeneity in rabbit ventricular tissue" Modelling Cellular Function Conference, Auckland, New Zealand (2003)

# ABSTRACT OF THE DISSERTATION

MULTISCALE COMPUTATIONAL MODELS OF TRANSMURAL HETEROGENEITIES AND VENTRICULAR ARRHYTHMOGENESIS

by

Sarah N. Flaim

Doctor of Philosophy in Bioengineering

University of California, San Diego, 2006

Professor Andrew D. McCulloch, Chair

Transmural differences in the expression patterns of many ion channels distinguish myocytes isolated from the ventricular endocardium, epicardium and midmyocardium of several species. Modifications to ion channel function, e.g. by accessory subunits, phosphoregulation or congenital abnormalities, may alter cellular electrical activity in a myocyte subtype specific manner, increasing dispersion of repolarization. However, in well-coupled myocardial tissue, repolarization gradients are thought to be minimized by electrotonic coupling.

Advances in molecular biology have yielded a wealth of quantitative information on the structure, function and regulation of cardiac ion channels. As the consequences of congenital "ion channelopathies" are often explored in isolated expression systems, it is difficult to establish a connection between the molecular mechanisms of ion channel defects and their clinical phenotypes. Furthermore, the ability to obtain high resolution measurements of electrophysiological phenomena *in vivo* is extremely limited. Thus, the objective was to develop and validate computational multiscale

models to investigate the hypotheses that 1) transmural heterogeneities in the molecular mechanisms underlying cellular electrical activity influence patterns of activation and recovery in well-coupled myocardial tissue, and 2) heritable ion channel mutations amplify these heterogeneities and contribute to potentially life-threatening arrhythmogenesis.

In this work, we integrated biophysically detailed ionic models into geometrically accurate 3D finite element models of cardiac conduction. These models predicted that 1) intrinsic cellular heterogeneities are attenuated in well-coupled myocardial tissue by electrotonic coupling; 2) autonomic-mediated amplification of spatial heterogeneities link a molecular level genetic mutation in KCNQ1 with proarrhythmic cellular events and T-Wave abnormalities; 3) sustained components of $I_{Kv43}$ and $I_{NaL}$ play a major role in shaping the cardiac action potential; and 4) increased dispersion of repolarization resulting from an SCN5A mutation permits pause-dependent episodes of polymorphic ventricular tachycardia. These findings suggest that, despite electrotonic interactions that minimize repolarization gradients, ion channel mutations may amplify intrinsic cellular heterogeneities thus creating an electrically unstable substrate. Multiscale computational modeling is a powerful tool to integrate the molecular mechanisms of ion channel regulation into the native, complex environment of the cardiac ventricular myocyte and intact myocardial tissue, thus bridging the gap between congenital defects and clinical phenotypes.

# CHAPTER 1

# Introduction

Sudden cardiac death (SCD) is a major cause of mortality within the industrialized world (153). The abrupt loss of effective heart function usually arises from chaotic cardiac electrical activity, or ventricular fibrillation (VF). In normal hearts, a propagating electrical wavefront elicits coordinated contraction of the billions of cells comprising the heart. Pacemaker cells in the right atria initiate the impulse which quickly spreads over the heart via the specialized cardiac conduction system. The pattern of activation controls the sequence of cellular contraction, thus any disturbance to either the initiation or propagation of the wavefront, clinically known as *arrhythmia*, can have potentially serious implications on the ability of the heart to function effectively as a pump.

Cardiac myocytes normally support a negative potential across the cell membrane at rest. This resting "transmembrane" potential is maintained by an electrochemical gradient of $K^+$ ions between the intra- and extra-cellular space. Electrical stimulation of an individual cardiac myocyte above a threshold results in a so-called action potential, during which the membrane is transiently depolarized and repolarized. The passage of the ionic species (predominantly $Na^+$, $Ca^{2+}$ and $K^+$) occurs via membrane-spanning protein complexes known as ion channels, which change conformation in a voltage- or time-dependent manner.

Individuals harboring genetic mutations in certain ion channels may be predisposed to developing serious ventricular arrhythmias. Although the mechanisms responsible for arrhythmia formation and destabilization arising from these "ion

channelopathies" are not fully understood, it is thought that amplified dispersion of repolarization may contribute significantly to electrical instability. It is increasingly recognized that even under normal conditions, measurements of action potential duration and morphology within the left ventricle are highly heterogeneous (9). Amplification of these intrinsic electrical heterogeneities is thought to contribute to increased repolarization gradients and predisposition to arrhythmia formation. Although there exist apical-basal (48) and interventricular (242) differences in cellular electrical properties, *transmural* heterogeneities are arguably the most distinct and well studied. Recognition of regional variation in the expression and function of ion channels across the wall of the left ventricle have promoted the notion of transmural dispersion of repolarization (TDR).

Clinically, an increase in TDR is associated with increased risk of malignant ventricular arrhythmias (10). Recent studies evaluating what were thought to be arrhythmia-suppressing drugs yielded the unexpected and disturbing finding that many agents used in the trials were in fact proarrhythmic (53, 167). Many class I and III antiarrhythmic drugs, some of which had been administered to patients for decades, appeared to slow conduction, prolong QT intervals and increase TDR. Although beneficial for some individuals, these agents were linked with induction of ventricular arrhythmias and SCD in other patients. Over the years, pharmacological interventions had been developed without detailed knowledge of the molecular mechanisms underlying the disease phenotypes and drug interactions. Thus, in order to develop effective treatments for serious malignant ventricular arrhythmias, it is of the utmost importance to understand the precise mechanisms of arrhythmia formation and the role of repolarization heterogeneities within the ventricular myocardium.

## 1.1 Molecular basis of cellular heterogeneities

Significant differences in the expression pattern of a number of ion channels is an important functional distinction among cells isolated from the ventricular endocardium, epicardium and midmyocardium of many species, including human (54, 105), dog (16, 204), guinea pig (16), rabbit (124) and mouse (30). The major consequence of this systematic variation in ionic currents is a heterogeneity of action potential duration (APD), morphology and rate-dependence (105). It is hypothesized that these so-called intrinsic differences promote a normal sequence of activation and repolarization in healthy hearts, but that exaggeration of repolarization heterogeneities, via drug actions, inherited mutations or acquired disease, is proarrhythmic. A large number of experimental studies of ventricular myocytes have begun to define the molecular and ionic mechanisms underlying the transmural heterogeneities of ion channel and calcium ($Ca^{2+}$)-handling proteins. The corresponding ionic currents include: the transient outward potassium ($K^+$) current, $I_{Kv43}$ (110); the slowly activating delayed rectifier current, $I_{Ks}$ (109); the late $Na^+$ current, $I_{NaL}$ (273); the $Na^+$-$Ca^{2+}$ exchanger, $I_{NaCa}$ (255, 274); and the SR $Ca^{2+}$-ATPase uptake rate, $I_{SERCA}$ (93). Although the focus of this work is primarily on *transmural* variation in ion channel expression and function, we also refer to apico-basal and interventricular differences where relevant.

### 1.1.1 The transient outward $K^+$ current, $I_{to1}$

Many investigators have measured a strong transmural gradient of the 4-aminopyridine-(4-AP)sensitive transient outward current, $I_{to1}$ (14, 174, 269). A large $I_{to1}$ underlies the prominent spike and dome action potential morphology typical of ventricular epicardial and (to a lesser extent) midmyocardial myocytes, whereas it is nearly absent in the endocardium. The molecular basis of this gradient appears to be

species dependent. In the canine and human ventricles, $I_{to1}$ is primarily carried by Kv4.3 channels with some contribution from Kv1.4 (52, 83). A recent investigation suggests that co-assembly of Kv4.3 with the ancillary (β) subunit KChIP2 is necessary for effective channel function in cardiac myocytes (174). A steep transmural gradient of KChIP2 is thought to contribute to the gradient of $I_{to1}$ in canine and human ventricle, since expression of the Kv4.3 α subunit was found to be homogeneous across the wall (174). As well as this reduction in α subunit expression, endocardial $I_{to1}$ recovers from inactivation significantly slower than epicardial $I_{to1}$ (129). The slower recovery from inactivation on the endocardium appears to play a small role in the steeper rate-dependence of APD in epicardial versus endocardial cells (108).

Heterologous expression of Kv4 α subunits fails to reconstitute the gating kinetics of native $I_{to1}$ unless KChIPs are coexpressed (4, 18, 19, 21, 146, 147). The mechanisms by which KChIPs exert their effects on Kv4 channel activity appear to be by increasing cell surface expression, slowing inactivation kinetics, and accelerating recovery kinetics (4, 18, 19, 21, 146, 147). Patel et al (148) recently conducted a thorough quantitative analysis on the voltage dependence of activation, deactivation, inactivation and recovery kinetics of Kv4.3 expressed alone and in the presence of KChIP2 subunits. Their results indicate that KChIP2 isoforms slow closed-state inactivation, accelerate recovery from inactivation and promote a $Ca^{2+}$ dependent open-state inactivation. Based on their results, these authors propose a continuous time Markov model that separates the $Ca^{2+}$-dependent open state from the $Ca^{2+}$-independent closed state inactivation (Appendix C: Figure C.1). If the relevance of the data extends to cardiac myocytes, this model suggests that the kinetic behavior of $I_{to1}$ is much more complex than current ionic models predict.

Many other mechanisms of Kv4 channel regulation have been demonstrated (for a review see Patel and Campbell (145)). Briefly, these other regulatory subunits include

frequenin (132), MinK-related peptide 1 (MiRP1) (265) , NFAT/calcineurin (177) and DPPXs (131), which may all contribute to $I_{to1}$ regulation *in vivo*. Of these, frequenin is thought to be the most likely candidate (145), possibly due to the structural similarity to KChIPs (both are neuronal $Ca^{2+}$ sensors containing multiple EF hands). Indeed, frequenin has been shown to coimmunoprecipitate with Kv4.3 α subunits in mouse ventricle extracts (68). However, others were unable to detect this association (163). Furthermore, it has been demonstrated that the interactions of KChIPs with Kv4 channels are substantially stronger and/or more efficient than those of frequenin (163). Thus, in addition to KChIPs, there may be other important mechanisms of Kv4 channel regulation in cardiac myocytes.

As well as transmural variation, there also exists a marked increase in right ventricular (RV), as compared to left ventricular (LV), $I_{to1}$ density. These transmural and interventricular differences in the density of $I_{to1}$ lead to voltage gradients during ventricular activation that manifests as a J (or Osborn) wave on the ECG (258).

### 1.1.2 The slowly activating delayed rectifier current, $I_{Ks}$

The slowly activating delayed rectifier current, $I_{Ks}$, is usually measured as the "tail" current resulting from a repolarization step to -20mV following a 5-s depolarizing stimulus. Both the depolarization current and the tail current are significantly smaller on average in midmyocardial cells than in endocardial and epicardial cells (109), which is thought to contribute in part to action potential prolongation in midmyocardial cells. Mutations in KCNQ1, the pore-forming ion channel subunit of the $I_{Ks}$ channel, or KCNE1, the β subunit, result in long QT syndrome type-1 (LQT1) and type-5 (LQT5), respectively.

The slow kinetics of $I_{Ks}$ tail current decay in guinea pigs allow residual activation or "accumulation" of this current during rapid pacing. This is thought to contribute to

APD rate-dependence (82). This phenomenon does not appear to extend to canine, where increased recovery rates result in no accumulation under normal conditions. However, it is observed following application of isoproteronol (210) which results in PKA phosphorylation of KCNQ1 and a subsequent increase in $I_{Ks}$ current density.

In canine and other large mammals, $I_{Ks}$ plays a subsidiary role to the rapidly activating delayed rectifier current, $I_{Kr}$, in the absence of elevated adrenergic tone (205). As such it likely serves as a compensatory repolarization reserve when other currents are inhibited, as evidenced by the greatest APD prolongation response of midmyocardial cells to $I_{Kr}$ blockers such as sotalol and E-4031 (185).

As well as transmural variation, $I_{Ks}$ tail currents are significantly larger in cardiac myocytes isolated from the RV than from the LV (242).

### 1.1.3 The late $Na^+$ current, $I_{NaL}$

The voltage-dependent cardiac $Na^+$ channel carries the large inward current $I_{Na}$ responsible for the rapid depolarization of the myocyte membrane potential at the start of the action potential. Emerging evidence suggests there is a sustained component of $I_{Na}$ active later during the action potential originating from channels that fail to inactivate or channels that recover from inactivation during phases 2 and 3 (180, 181). These openings have been measured in single channels (179, 270) and constitute the late $Na^+$ current ($I_{NaL}$). The probability of cardiac voltage-gated $Na^+$ channels opening at potentials matching the action potential plateau is estimated to be roughly 1% (117). This is thought to be increased in midmyocardial (109) and failing ventricular cells (230), in both instances leading to APD prolongation.

Inherited mutations in *SCN5A*, the gene encoding the α subunit of the channel, Nav1.5, may also disrupt $Na^+$ channel inactivation, delay cellular repolarization and be associated with an increased risk of arrhythmia (84, 247). One such example is the

I1768V mutation, which increases the rate of recovery of inactivation, leading to an increase in Phase 3 (but not Phase 2) $I_{NaL}$ (39). In addition, $I_{NaL}$ has been recognized as one of the major factors contributing to abnormal repolarization in heart failure (117).

The substantial difference in magnitude between the large fast transient current (1 nA, 1 ms) and the smaller late component (~10 pA, 1 s) have hindered thorough experimental examination of $I_{NaL}$ (117). A recent modeling study consisting of three gating modes of $Na^+$ channels (transient, burst and late scattered) suggested that late components of $I_{Na}$ transfer about the same amount of charge as the transient current (117). It also predicted that heart failure significantly slows gating of $I_{NaL}$, resulting in greatly increased $Na^+$ influx during prolonged membrane depolarization.

Information is slowly coming to light as to the relationship between the structure of Nav1.5, its electrophysiological function, and modulation by regulatory molecules. The cardiac $Na^+$ channel has four structural domains, each consisting of six membrane-spanning subunits and has both intracellular N and C termini. It appears that interactions between the intracellular C-terminal domain and the intracellular III-IV linker confer stability on $Na^+$ channel inactivation (248). The gating modes of single cardiac $Na^+$ channels have specific activation and inactivation kinetics (28). Modal gating of cardiac $Na^+$ channels may be regulated by phosphorylation through protein kinase C (224) and/or by protein kinase A (225), mechanisms involving intracellular $Ca^{2+}$ (51, 223) or mechanical stress on the plasma membrane during contraction of the heart muscle cell (28). The enzyme Nedd-4.2 appears to play a role in the trafficking of Nav1.5 to the cell surface (234).

### 1.1.4 The $Na^+$-$Ca^{2+}$ exchange current, $I_{NaCa}$

The $Na^+$-$Ca^{2+}$ exchanger (NCX), permits a reversible current, $I_{NaCa}$, that functions under normal conditions primarily to remove intracellular $Ca^{2+}$. However, it is also an

important modulator of excitation-contraction coupling (ECC) and arrhythmia due to its effects on $Ca^{2+}$ signaling. A recent report described the presence of a transmural gradient of $I_{NaCa}$ in the canine LV free wall (decreasing from epicardium to endocardium) (255). This appears to be disrupted in failing hearts via regional upregulation of $I_{NaCa}$ on the endocardium resulting in uniform expression (255). However, a prior investigation into $I_{NaCa}$ gradients measured the greatest current densities in midmyocardial cells (274). Moreover, a recent study reported a reversal of the $I_{NaCa}$ gradient in normal guinea pig hearts, decreasing from endocardium to epicardium (246) (although this may be due to interspecies variability). It is therefore difficult to establish the true nature of the transmural gradient of $I_{NaCa}$ from these reports.

### 1.1.5 The SR $Ca^{2+}$-ATPase, SERCA

There also exist important regional variations in the mechanisms responsible for myocyte $Ca^{2+}$ homeostasis. Time to peak and the duration of the $Ca^{2+}$ transient are longer in endocardial cells (46). In addition, SR $Ca^{2+}$ content, as measured by rapid application of caffeine, is greatest in epicardial cells (46). Experimental evidence suggests that a combination of electrical heterogeneity and intrinsic differences in ECC underlie the distinctions in the SR $Ca^{2+}$ concentration and kinetics of the $Ca^{2+}$ transients. Greater SERCA expression on the epicardium may contribute to a higher SR $Ca^{2+}$ content and faster decay (93), while the spike and dome morphology of the epicardial action potential waveform permits a greater L-Type $Ca^{2+}$ current (LCC) current (64). It is presumed that these differences result in a more coordinated contraction of the ventricular myocardium, i.e. the faster kinetics of epicardial cells compensate for the delay in activation. There may also be other regional variations in protein expression or modulation that have not yet been identified.

## 1.2 Autonomic regulation of ion channel function

Neurohormonal control is an important functional regulator of cardiac electrophysiology via the downstream effects on ion channel function. In cardiac myocytes, norepinephrine (NE) binds to the $\beta_1$-adrenergic receptor, initiating a cascade of signaling events resulting in the phosphorylation of a number of proteins, including the L-type $Ca^{2+}$ channel (LCC), phospholamban (PLB) and KCNQ1, which all play a role in the generation of the action potential and/or $Ca^{2+}$ cycling (26). Furthermore, activation of the sympathetic nervous system (SNS) and the subsequent release of NE are implicated in increased arrhythmogenic risk (71, 218). While β-blockers are highly successful anti-arrhythmic agents, the electrophysiological responses to $\beta_1$-adrenergic agonists and the mechanisms of arrhythmia formation, particularly with respect to temporal and spatial heterogeneities, remain poorly understood.

In structurally normal hearts, enhanced SNS activity is thought to facilitate electrical instability by increasing automaticity, decreasing the threshold for activation and increasing the heterogeneity of refractoriness (71). Han et al (70) demonstrated increased dispersion of recovery with stimulation of the cardiac sympathetic nerves. Recently, Taggart et al (218) demonstrated that the adrenergic agonists isoprenaline and adrenaline increased the steepness of the slope of the APD restitution curve, which has been shown to promote wave break and ventricular fibrillation (VF) (142). Although local applications of NE to the ventricular subepicardium elicited reproducible ventricular tachyarrhythmias (135), infusion of β-adrenergic agonists reversed the arrhythmia (135) and does not appear to increase dispersion of repolarization (71, 135). One explanation that accounts for the differential response is that increased sympathetic activity via stimulation of cardiac nerves results in

heterogeneity of neurotransmitter release and cellular response, whereas intravenous infusion may result in a more uniform modulation of myocardial electrophysiological properties.

From investigations into the anatomy of the cardiac nervous system, it appears that sympathetic nerves follow the common pulmonary artery into the plexus supplying the main left coronary artery, where they are distributed to the myocardium in superficial epicardial layers. Experimental evidence suggests that the overlap in the location of sympathetic nerves and the coronary network extends into the myocardium (271). The distribution of β-adrenergic receptors appears to be nonuniform, with the highest density occurring in the most innervated regions of the heart (34). This results in a transmural gradient of receptor density, decreasing from epicardium to endocardium (34).

Post-infarction injury to peripheral nerves has been shown to trigger neural remodeling via the reexpression of nerve growth factor (NGF) or other neurotrophic factor genes (103), which leads to possible hyperinnervation in the heart (69). Many investigators have observed spatially heterogeneous innervation in the ventricles with regional hyperinnervation in the periphery of injured myocardium and denervation in necrotic areas (33, 243). It has recently been confirmed that a significant portion, if not all, of regenerated nerves are sympathetic (267).

Clinical and experimental observations suggest that this heterogeneous neural remodeling, while associated with improved hemodynamic performance in transplant patients (192), results in an electrically unstable substrate. Cao *et al* noted an association between the density of regional hyperinnervation in injured ventricular myocardium and the history of ventricular tachyarrhythmias in patients with severe heart failure (33). It also appears that a combination of both neural and electrical remodeling interact adversely to facilitate spontaneous ventricular tachyarrhythmias

and sudden cardiac death (32), although it is unclear what the underlying mechanisms are.

Patients with LQT1 harbor mutations in KCNQ1, which encodes the α subunit of the $I_{Ks}$ channel, and are particularly at risk to SCD during exercise or emotional stress, suggesting a connection with sympathetic stimulation (195). While healthy individuals have shortened or unchanged QT intervals with sympathetic stimulation, QT intervals in many LQT1 patients prolong further, implying a defect at the interface between the SNS and electrophysiology. Other disorders linked to SNS activation include LQT2, catecholaminergic polymorphic ventricular tachycardiac (CPVT) and congestive heart failure (CHF).

## 1.3 Intracellular $Ca^{2+}$ cycling and arrhythmia formation

Depolarization of the cardiac ventricular myocyte activates voltage-gated L-type $Ca^{2+}$ channels (LCCs) and the resulting influx of $Ca^{2+}$ from the extracellular space triggers the release of $Ca^{2+}$ from the sarcoplasmic reticulum (SR). This phenomenon, termed $Ca^{2+}$-induced $Ca^{2+}$ release (CICR), transiently increases cytosolic $Ca^{2+}$ to a level which initiates myocytes contraction. The local control hypothesis predicts that an individual LCC located in the T-tubule will trigger $Ca^{2+}$ release from a small cluster of ryanodine receptors (RyRs) in the closely apposed SR terminal cisternae (211). A collection of functionally linked LCCs and RyRs make up a so-called $Ca^{2+}$ release unit (CaRU). The $Ca^{2+}$ concentration in the subspace surrounding the CaRU is an order of magnitude larger than that in the bulk cytoplasm (64).

Intracellular $Ca^{2+}$ cycling is an important regulator of normal and abnormal excitation-contraction coupling (ECC). Briefly, recent experimental data has demonstrated inactivation of the sarcolemmal LCC to be primarily $Ca^{2+}$-dependent (107). Fluctuations in intracellular $Ca^{2+}$ levels can modulate the shape and duration of

the cardiac action potential via altering transmembrane $Ca^{2+}$ fluxes. Free $Ca^{2+}$ may also bind to regulatory molecules, such as calmodulin and KChIPs, to modify ion channel function on a beat-to-beat basis, or over longer time periods (149).

In extreme instances, highly proarrhythmic $Ca^{2+}$-mediated afterdepolarizations, both early and delayed, may be observed. These are both examples of triggered arrhythmias (abnormal impulse initiation). Early afterdepolarizations (EADs) occur during Phases 2 and 3 of the action potential and are thought to be mediated by reopening of the LCCs. The resulting influx of $Ca^{2+}$ halts the repolarization process and results in oscillating fluctuations of membrane potential. EADs are facilitated by hypertrophy, slow pacing rates, hypokalemia, hypomagnesaemia, hypoxia, acidosis, the presence of catecholamines and any drug that prolongs repolarization (7, 251). Delayed afterdepolarizations (DADs) occur after full repolarization and are thought to originate from spontaneous release of $Ca^{2+}$ from the SR, either due to $Ca^{2+}$ overload or abnormalities in luminal $Ca^{2+}$ control. Both these $Ca^{2+}$-mediated after-depolarizations may trigger a serious polymorphic ventricular tachycardia known as torsade de pointes (38).

EADs and DADs may also substantially increase dispersion of repolarization, predisposing the tissue to so-called reentrant arrhythmias (abnormal impulse propagation). Many dangerous forms of aberrant electrical conduction are driven by rotating spiral waves of excitation, that form under conditions of inhomogeneous refractoriness (3) and slowed conduction (251). It is hypothesized that reentrant arrhythmias may further disintegrate into complex chaotic wavelets of activation, resulting in VF and potentially SCD (3, 63).

In addition, $Ca^{2+}$ transient alternans in the absence of action potential alternans may be observed at high stimulation rates, promoting the concept that dynamic instabilities in $Ca^{2+}$ cycling can influence instabilities in membrane potential (37).

Further experimental investigation has suggested that intact $Ca^{2+}$ cycling is required for action potential alternans formation (62).

## 1.4 Inherited and acquired "ion channelopathies"

There exist a number of heritable disorders that predispose certain individuals to potentially life-threatening repolarization-related arrhythmias. These disorders include the long-QT syndrome, Brugada syndrome, the short QT syndrome and catecholaminergic polymorphic ventricular tachycardia. These conditions are characterized by normal heart structure and seemingly innocuous electrocardiographic alterations. In some cases, these conditions can also be "acquired" secondary to use of certain medications in susceptible individuals.

In the last decade, there has been significant progress in determining the genetic bases of inherited ion channelopathies (for a review, see LeRoy and Russell (102) or Roberts (167)). Although there is significant overlap in the affected ion channels, the clinical presentations of each syndrome and the electrical heterogeneities underlying the ECG abnormalities are distinct.

### 1.4.1 The Long QT Syndrome

The most common class of ion channelopathies is the *long-QT syndrome* (LQTS). The name arises from the characteristic QT interval prolongation on electrocardiogram (ECG) recordings. QT prolongation is indicative of a delay in ventricular repolarization. This disorder occurs in 1/3000-5000 individuals and accounts for a large number of incidences of SCD in children and young adults (36).

To date, there are seven known variants of LQTS, representing mutations in seven different genes. The most commonly diagnosed conditions are LQT1 (KCNQ1 mutations) and LQT2 (HERG mutations), which, along with the less prevalent LQT5

(KCNE1 mutations), LQT6 (KCNE2 mutations) and LQT7 (KCNJ2), delay repolarization by slowing $K^+$ efflux. LQT3, which represents approximately 8% of genetically confirmed diagnoses, affects repolarization by increasing the persistent $Na^+$ current, $I_{NaL}$. LQT4 is associated with mutations in ankyrinB and impaired function of multiple ion channels including the $Na^+$ pump and NCX. It is likely that more LQTS genes remain to be identified since genetic testing was inconclusive in around 30% of individuals (102).

There is considerable variability in the clinical presentation of LQTS (169, 222). The cause of LQTS symptoms, which include seizures, chest pain, syncope and SCD, is the polymorphic ventricular tachycardia torsades de pointes. The onset of torsades de pointes in patients with LQTS often develops in a pause-dependent fashion, i.e., immediately after a sinus beat after a postectopic pause. However, it can be associated with either bradycardia (with marked QT prolongation) or sinus tachycardia due to adrenergic stress. The mechanisms underlying the transition from normal rhythm to torsades de pointes to VF are unknown, although the prolonged APs are likely to predispose regions of the myocardium to EAD formation.

Clinical diagnoses are based on patient history and measurement of the rate-corrected QT interval (QTc by Bazett's formula) >0.46 seconds. However, syncope or cardiac arrest has been reported in 10-50% of LQTS carriers who have an apparently normal or borderline QT interval. This suggests reduced penetrance or contributions by modifier genes or environmental factors (such as electrolyte abnormalities) to the clinical manifestations of LQTS (102).

In addition to QT prolongation, T wave morphology is often abnormal, consistent with the concept that repolarization in LQTS displays substantial spatial and temporal heterogeneity. QT dispersion, as assessed by the difference between the longest and shortest QT intervals on a 12-lead ECG, is normally 46±18 ms. In patients with

LQTS, it is 133±21 ms (169). Furthermore, the T wave often has a notched or biphasic appearance. These findings, in turn, suggest that abnormal AP prolongation in LQTS may occur to a greater extent in some cells than in others. It is increasingly recognized that even under normal conditions, APs in the ventricle are highly heterogeneous, which suggests that different ion channel lesions might produce different and distinctive ECG patterns.

Another diagnostic ECG manifestation of LQTS is T-wave alternans (TWA). Here, the T wave is not only prolonged and abnormal, but also varies on a beat-to-beat basis, which indicates temporal variability in repolarization (169). The presence of visible T-wave alternans often predicts the occurrence of lethal ventricular arrhythmias (150), although the amplitude of TWA in LQTS patients tends to be of the order of microvolts and its predictive value uncertain (134).

### 1.4.2 Brugada syndrome

*Brugada syndrome* (BS) is another familial cause of SCD in young, apparently healthy individuals. It appears to be linked to SCN5A mutations that result in a reduction of $Na^+$ influx across the right ventricular epicardium (102). It is thought that premature repolarization in this region contributes to electrical heterogeneity of repolarization and creates an electrical substrate conducive to reentrant arrhythmias (6).

BS is characterized by ST segment elevation, prominent J-waves and SCD (6). The incidence is around 1/5000 individuals in the Western World (167) but may be much higher (1/200) in Thai and Japanese males from certain regions (6). It is also thought to be responsible for a significant proportion of cases of sudden infant death syndrome (167). Most drugs are not effective with BS and an implantable defibrillator is the only recommended form of therapy (167).

### 1.4.3 Short QT syndrome

The *short-QT syndrome* (SQTS) is a very rare condition characterized by surface ECG recordings of QT intervals < 300 ms (186), tall peaked T-waves (186) and a high risk of atrial and ventricular arrhythmias (167). So far, three variants have been identified, all of which result in a gain of function of $K^+$ channels that accelerate repolarization and shorten APD. The mechanisms whereby these defects induce arrhythmia are unknown, although regional repolarization heterogeneities between the epicardium and midmyocardium have been implicated (186). ICD implantation is recommended, although quinidine has been shown to normalize QT intervals in some SQTS patients (167).

### 1.4.4 Catecholaminergic polymorphic ventricular tachycardia

*Catecholaminergic polymorphic ventricular tachycardia* (CPVT) is characterized by exercise- or stress- induced bidirectional and polymorphic VT. These ECG manifestations are consistent with intracellular $Ca^{2+}$ overload and DAD events in response in increased adrenergic tone. Unlike LQT1, genetic mutations linked to CPVT result in abnormal $Ca^{2+}$ handling and release (167). Gain of function mutations in the RyR appear to result in enhanced $Ca^{2+}$ leak from the SR and are thought to account for ~50% of genotyped reports of CPVT (158). Loss of function mutations in the calsequestrine gene, CASQ2, that reduce SR $Ca^{2+}$ buffering capacity, have also been identified as a variant of CPVT (154). As with BS, CPVT is likely to account for some cases of sudden infant death syndrome (186).

### 1.4.5 Acquired long-QT syndrome

Marked QT prolongation and torsades de pointes may also occur as a consequence of administering certain drugs. The mechanism of this “acquired” LQTS is delayed

repolarization secondary to either a reduction in the rate of $K^+$ efflux, or, less commonly, an increase in $Na^+$ influx (167). Drug-induced QT prolongation occurs only in susceptible individuals, suggestive of a genetic predisposition. Case reports of patients with subclinical congenital LQTS that present with symptoms upon administration of exposure to $I_{Kr}$ blocker support the hypothesis of a genetic contribution to elevated risk of acquired LQTS. Genetic testing has identified gene mutations and single nucleotide polymorphisms (SNPs), mostly related to $K^+$ channels, that predispose to acquired LQTS (167).

Normal hearts employ multiple mechanisms to accomplish repolarization. For instance, over 20 $K^+$ channels are expressed in cardiac tissue, most of which contribute to AP repolarization (167). If one of these mechanisms is impaired, the redundancies in the system should protect against extreme perturbations. This so-called "repolarization reserve" may be jeopardized if there are abnormalities, either congenital or environmental, in several of the repolarization processes.

## 1.5 Structural heterogeneities

Activation of the ventricles is non-uniform, although well-coordinated by specialized cells in the cardiac conduction system. Purkinje fibers rapidly conduct electrical impulses from the atrioventricular node to the bulk of the myocardium. The fibers extend down the interventricular septum, penetrate into the heart apex and then branch up the lateral walls of the ventricles (25). Purkinje cells are located in the bundles of His, in the deepest layer of the endocardium. Thus, the first regions of the ventricles to be activated are the septum and the endocardial surfaces of both ventricles; the last, the epicardial surfaces (25).

Another source of electrical heterogeneity in ventricular myocardium arises from the varying orientation of cardiac muscle "fibers" and "sheets" (176) (138). Cardiac

electrical propagation within the ventricular myocardium is anisotropic, occurring fastest along the long axis of the fibers and slower in the transverse directions (96).

A typical cardiac myocyte is electrically connected to roughly 9-11 adjacent myocytes via proteins known as gap junctions (77). Electrotonic interactions between neighboring cells may lead to changes in the electrical activity of the myocytes. Specifically, if two electrically coupled cells have different electrophysiological properties, the electrotonic current will tend to minimize these differences (251). Furthermore, the intrinsic electrical properties of individual cells can be modified by their location with respect to the beginning and end of propagation and collision of wavefronts (251).

## 1.6 Controversies

In recent years, the mechanisms underlying the intrinsically long APDs and extreme rate-dependence of midmyocardial myocytes have been the focus of many experimental investigations. Previous hypotheses have been centered on the large (mostly $K^+$) outward currents that dominate late repolarization (Phase 3). However, evidence is emerging that some currents previously measured and defined as being transient, such as both $I_{Na}$ and $I_{to1}$ (specifically $I_{Kv43}$), exhibit smaller sustained components that may play a role maintaining the AP plateau. It is unknown to what extent these currents contribute to defining the electrical characteristics of cardiac myocytes.

The intrinsically long APDs, reduced repolarization reserve and strong rate dependence of isolated midmyocardial cells (M-cells) has implicated them in determining the polarity and width of the electrocardiographic T-wave in normal hearts (9, 13), and reentrant arrhythmia formation in pharmacologically altered hearts (representative of ion channelophathies e.g. long QT syndromes) (61, 202, 239).

However, there exists considerable debate as to the extent that midmyocardial cells play a role in intact myocardium given the tendency of intrinsic electrical differences to be masked by electrotonic effects. Experimental studies that have addressed this issue have varying results with evidence both for and against M-cell dominated electrical gradients (for review see Taggart et al (219)), leading to the question of whether M-cell-mediated increases in TDR occur *in vivo* or not. Previous modeling work has suggested that M-cells are not required for an upright T-Wave (40) and geometric factors such as wall thickness may alter the extent that intrinsic heterogeneities influence repolarization patterns (182).

Deflections in the ECG following the T wave are sometimes referred to as U waves. The origin of these U waves remains poorly understood. Both midmyocardial cell repolarization and DADs have been implicated as possible mechanisms.

## 1.7 Computational modeling of cardiac electrophysiology

Computational models in cardiac electrophysiology are valuable in understanding the normal and diseased heart, and as data accumulate on molecular and cellular mechanisms, the potential for powerful predictive mechanistic models is growing rapidly (122). Various parameters are measured *in vitro*, such as morphology and biochemistry, and then this information is used to implement these models *in silico*. The results are then validated *in vivo*, leading to iterative model refinement.

### 1.7.1 Ventricular anatomic models

Anatomically detailed 3D models of geometry and myofiber orientation for different species have been described for mouse (227), rabbit (237), dog (86, 97, 139), pig (212), sheep (244), and human (253). Geometries of these models have been obtained from histological measurements (97, 139, 212, 237), CT (253), or MRI scans

(86, 244). Myofiber orientations have been reconstructed from histological measurements (97, 139, 212, 237), diffusion weighted MRI (162, 196), or by calculations (165). In the latter study, myofiber orientation was calculated by using the hypothesis that myofibers are oriented such that shortening during ejection is as homogeneous as possible. Sheet orientations have been obtained by histological measurements (98) or can be obtained by calculations (17), but there is recent evidence that sheets can also be measured with diffusion weighted MRI (73). In addition, Usyk et al (231) included Purkinje fibers to their model, which were fitted to measurements.

### 1.7.2 Cellular models of cardiac electrophysiology

Cellular models of cardiac electrophysiology typically describe the action potential either phenomenologically (e.g. with FitzHugh-Nagumo equations (57)), or – more biophysically detailed – as a result of changing transmembrane ionic currents (23, 140). Most of these ionic models are based on the formalism originally established by Hodgkin and Huxley for the squid nerve (76). In these models currents are described according to Ohm's law, where (for example for a voltage-gated channel) the conductance is dependent on time and voltage and is typically described as a function of the open-probability of gates (in the form of ordinary differential equations, or ODEs). Later models (from 1977 (22)) also include ion concentrations. Ionic models have become increasingly complex, through iterative interactions between experiment and simulation (140), describing more ion channels and ion concentrations, the latter in different compartments of the cell (80, 113). Recent models also include transmural heterogeneity of channel expression (72, 143, 226, 240) or describe certain channels in a more complex manner with so-called Markov models (38, 80), reflecting channel behavior more realistically than Hodgkin-Huxley

formulations. These latter models typically have >30 ODEs and are computationally expensive.

Ionic models have been developed for different species, for mouse (227), rat (143), guinea pig (113), rabbit (160), dog (58, 80), and human (22, 156, 226).

### 1.7.3 Multicellular models of cardiac electrophysiology

Cellular level models can be incorporated into larger scale models – either as a discrete set of cells or tissue bundles or as a continuum. Creating a model that treats each cell as discrete unit results in what is called a network, or discrete model (101, 228, 235). Tissue models with over 140,000 cells have been produced using this approach (128). An alternative to this type of modeling is to treat the tissue as a syncytium and assume that at any given point there exists a transmembrane electrical potential (monodomain models) or both an intracellular and extracellular space (bidomain models (60, 74)), for which the electrical potentials are computed.

One of the drawbacks of traditional finite element implementations of monodomain and bidomain equations is that they fail to represent the discontinuous nature of electrical propagation. Trew et al (229) have overcome this by using a finite volume technique that explicitly represents microstructural features such as the electrically non-conducting cleavage planes between sheets of myocardial fibers. They demonstrate that these discontinuities have important implications for defibrillation.

### 1.7.4 Whole heart models of cardiac electrophysiology

Bidomain and monodomain models have been used to examine a wide variety of cardiac tissues and phenomena in the whole heart, including investigations of Purkinje fiber (152), reentrant ventricular activity (24, 101, 144) and defibrillation in dog (171) and rabbit (170), although in general these whole heart simulations use simplified

ionic models. One exception are the recent mouse and rabbit models of Sampson and Henriquez (183) where they demonstrate that the smaller the heart, the stronger the effects of electrotonic coupling (i.e. reducing dispersion of APD).

### 1.7.5 Implementation issues

Although computer memory and speed continue to grow with advances in technology, simulations of 3D cardiac electrophysiology problems remain large and time consuming and continue to grow rapidly along with advances in biology. Issues of convergence and parameter sensitivity are also of increasing concern as the number of variables increases. Such memory and computationally intensive models require high performance computing techniques utilizing distributed and shared memory parallel computing architectures (92, 214).

## 1.8 Scope of the dissertation

The fundamental difficulties in simultaneously mapping dynamic myocardial electrical activity in three-dimensions limit high resolution experimental investigation of important scientific questions. Thus, the objective was to develop and experimentally validate computational multiscale models to investigate the hypotheses that 1) transmural heterogeneities in the molecular mechanisms underlying cellular electrical activity influence patterns of activation and recovery in well-coupled myocardial tissue, and 2) heritable ion channel mutations may amplify these heterogeneities and contribute to potentially life-threatening arrhythmogenesis. This was achieved via the integration of biophysically detailed ionic models into geometrically accurate finite element models of cardiac conduction. Concomitant development of high performance computing techniques was required in order to solve the complex system of ODEs at each gauss point in the mesh within a

reasonable time frame. These models have been used to gain insight into cellular mechanisms of arrhythmia formation within intact heterogeneous ventricular tissue.

Chapter 2 describes the initial development and validation of a heterogeneous rabbit left ventricular wedge. We use this model to investigate the hypothesis that a single gene defect resulting in long-QT syndrome type 1 (LQT1), in the presence of structural and cellular heterogeneities, leads to conditions facilitating the development of serious ventricular arrhythmias via increased transmural dispersion of repolarization and $Ca^{2+}$-mediated afterdepolarizations in a rabbit left ventricular tissue wedge. We also describe the high performance computing techniques developed to permit timely solution of equations and provide information on the computational performance of the algorithm on a distributed memory cluster.

In Chapter 3, the analysis is extended to explore the arrhythmogenic consequences of asynchrony and heterogeneity in rabbit LV myocytes and tissue during $\beta_1$-adrenergic stimulation. Here, we hypothesize that time-varying responses to $\beta_1$-adrenergic stimulation occur as a result of differences in the time course of phosphorylation of PKA targets, specifically the LCC, PLB and IKS, and that this asynchronous response results in a transient period of increased dispersion of repolarization, and thus vulnerability to reentrant arrhythmias.

Chapter 4 examines the contributions of sustained $I_{Na}$ and $I_{Kv43}$ to transmural heterogeneity of early repolarization and arrhythmogenesis in canine left ventricular myocytes and the effect of the LQT3 mutation, I1768V. We hypothesize that due to the relatively high resistance characteristic of the ventricular action potential plateau these small currents can play a role modulating the AP waveform. We also predict that the increased ratio of $I_{Kv43}$ to $I_{NaL}$ may protect epicardial myocytes from EADs resulting from the I1768V mutation-induced increase in $I_{NaL}$.

This model is then upwardly integrated into a canine LV tissue model in Chapter 5 to explore the effects of electrotonic interactions on action potential propagation in intact heterogeneous tissue. Here, we surmise that (1) electrotonic interactions will play a major role in modifying the intrinsic electrophysiological behavior of canine LV myocytes, and (2) regional heterogeneities will play a role in the development of malignant polymorphic ventricular arrhythmias (such as torsade de pointes) in the presence of the I1768V mutation.

Finally, Chapter 6 summarizes the work and provides a perspective on its role in enhancing our understanding of cellular heterogeneities and their contributions to arrhythmia formation.

# CHAPTER 2

# Proarrhythmic consequences of a KCNQ1 AKAP-binding domain mutation: 3D computational models of structural and cellular heterogeneity in rabbit ventricular tissue

## 2.1 Introduction

Long QT syndrome (LQTS) is a cardiac disorder in which the QT interval on the ECG is prolonged. Patients with mutations in KCNQ1, which encodes the $\alpha$ subunit of $I_{Ks}$, develop an LQTS (LQT1) particularly susceptible to sudden cardiac death during sympathetic stimulation (194). While healthy individuals have shortened or unchanged QT intervals with exercise or stress, QT intervals in LQT1 patients prolong further (1), suggesting a problem at the interface of the sympathetic nervous system and electrophysiology.

Further investigation of the molecular mechanisms at this interface led Kass *et al* (84) to discover a signaling complex of KCNQ1, protein kinase A, and protein phosphatase-1 (PP1) mediated by the A-kinase anchoring protein (AKAP) *yotiao*. In reconstituted systems, the LQT1 associated mutation KCNQ1-G589D disrupted the signaling complex, preventing β-adrenergic regulation of $I_{Ks}$. This raised the question of how the mutation may trigger arrhythmogenic cellular events, and how these cellular mechanisms interact with tissue-level properties of the heart such as fiber architecture and electrical heterogeneities.

Electrical heterogeneity within the ventricular myocardium arises from a number of sources. There are intrinsic electrophysiological differences between myocytes isolated from different regions (most markedly between the epicardium, midmyocardium and endocardium) of the left ventricle (9). Regional variation in

electrical load due to wavefront propagation and collisions modifies intrinsic action potential characteristics, as does the degree of electrotonic coupling between cardiac myocytes (251). Furthermore, the arrangement of cardiac myocytes into fibers and sheets results in anisotropic conduction (138). The likelihood of reentrant arrhythmia formation increases under conditions of nonuniform refractoriness, highlighting the importance of these heterogeneities, especially with regards to pathological conditions that may amplify dispersion of repolarization.

Recent examples have shown a promise of computational models for investigating the impact of gene mutations (38), tissue heterogeneities (120) and dynamical instabilities (254) on arrhythmic mechanisms. Here, we use an integrative computational model of $\beta_1$-adrenergic signaling, excitation-contraction coupling, and action potential propagation to investigate the proarrhythmic consequences of KCNQ1/KCNE1 signaling complex disruption in intact ventricular myocardium. Model analysis indicates that while the KCNQ1-G589D mutation did not necessarily prolong the QT interval at rest, sympathetic-stimulated increases in $I_{Ca,L}$, left uncompensated by increased $I_{Ks}$, resulted in QT prolongation. This impaired response to sympathetic stimulation precipitated $Ca^{2+}$-mediated afterdepolarizations and increased TDR in ventricular tissue, significant factors related to arrhythmic risk. However, moderate increases in heart rate protected against these proarrhythmic mechanisms.

## 2.2 Methods

### 2.2.1 Cellular model of $\beta_1$-adrenergic signaling

We used a previous mechanistic mathematical model of $\beta_1$-adrenergic signaling in rat (188, 190), adapted for the rabbit ventricular myocyte (189). Briefly, the following

changes were motivated by experimental data: adjusting protein expression levels for β-adrenergic receptors (55), PDE4 (198), PKA (44) and phospholamban (42); inclusion of the PDE3 isoform (127); and the addition of a KCNQ1/KCNE1 signaling complex containing KCNQ1, KCNE1, yotiao, PKA, and PP1 (119). Methods for modeling these signaling networks have been described in detail previously (190). The new signaling model included a total of five PKA phosphorylation targets: the L-type calcium channel ($I_{Ca,L}$), phospholamban (PLB), ryanodine receptor (RyR), troponin I (TnI), inhibitor-1, and KCNQ1. The KCNQ1-G589D defect associated with LQT1 syndrome was modeled as a $10^6$ fold increase in the dissociation constant for KCNQ1 and yotiao (Figure 2.1A).

A previously published model of excitation-contraction coupling in the adult rabbit ventricular myocyte (160) was modified to include a simple model of calcium-induced calcium release (56) and a reversible $Ca^{2+}$ SR-ATPase pump (200). Phosphorylated $I_{Ks}$ channels were modeled as being 3.6x more likely to be actively gating, with a 35.6 mV leftward shift in the activation curve for the $I_{Ks}$ gating variable, consistent with whole-cell patch clamp recordings with cAMP and isoproterenol (245). The signaling and excitation-contraction coupling models were fully connected with one another (Figure 2.1B).

### 2.2.2 Multiscale computational model of action potential propagation

All our finite element (FE) models were repetitively refined until the APD and conduction velocity were converged to within 2%. The finite element mesh forms the computational foundation for the spatially coupled solution of the governing PDE of cardiac electrical propagation in a monodomain. Propagating action potentials can be described by a non-linear reaction diffusion equation:

$$\frac{\partial V_m}{\partial t} = \nabla \bullet D \nabla V_m - \frac{I_{ion}}{C_m}$$

where $V_m$ is the transmembrane voltage (mV), $I_{ion}$ is the sum of the currents that cross the membrane through ion channels ($\mu A/cm^2$), $C_m$ is the capacitance of the membrane ($\mu F/cm^2$), $D$ is the diffusion coefficient ($cm^2/ms$). The complex fiber-sheet architecture of cardiac tissue results in anisotropic condition with greater conductivity along the orientation of the fibers. The diffusion coefficient was chosen to obtain a 2:1 ratio of longitudinal to transverse conduction velocity (40).

We use a collocation-Galerkin scheme that has been shown to result in faster convergence than other FE methods (172). The tissue is treated as a continuum but the regional action potential properties are derived from a cellular ionic model consisting of a system of ordinary differential equations (ODEs) that are integrated over time using an implicit Runga-Kutta method. No-flux boundary conditions were prescribed along the edges of the tissue. The derivation of the governing equations and finite element formulations is presented in Appendix H.

### 2.2.3 Model validation

The cellular model was previously validated with independent experimental data from the literature at a variety of functional levels, obtained from isolated rabbit ventricular myocytes whenever possible. In our ventricular wedge model, the diffusion coefficient was chosen to yield a transmural conduction velocity of 27 cm/s at 3 Hz agreeing with results from Sung et al. (215), who measured transverse velocities of 23 ± 6 cm/s in an isolated Langendorff-perfused rabbit heart. All measurements of electrophysiological function were consistent with the experimental results from the literature performed in arterially perfused rabbit wedge preparations

of similar size at 1 Hz (260): endocardial $APD_{90}$ (217 vs 212 ms), epicardial $APD_{90}$ (166 vs. 191 ms), QT interval (245 vs. 251 ms) and transmural dispersion of repolarization (TDR) (36 vs. 43 ms) (see Figure 2.2C)

### 2.2.4 High performance computing techniques

Models of action potential propagation are computationally and memory intensive because of the combination of a small space constant of conduction and the rapid temporal kinetics of the membrane currents. We have used various strategies to improve computational performance including:

- The use of an operator-splitting algorithm to decouple the ODE solution of the cellular model with the PDE solution of electrical propagation (161)
- Development of a python module allowing parallel programming with the Message Passing Interface (MPI) for parallelization of the ODE solution (to reduce computational time)
- An implicit scheme for time-stepping
- An implicit Runga-Kutta ODE solver RADAU
- A very efficient linear solver SuperLU

## 2.3 Results

### 2.3.1 Experimental validation of $APD_{90}$ in isolated and ventricular wedge simulations

To confirm that our model adequately predicted regional action potential characteristics of isolated and coupled rabbit ventricular myocytes, we upwardly integrated the Puglisi-Bers ionic model into a three-dimensional model of a rabbit ventricular wedge. $APD_{90}$ rate-dependence of WT endocardial, midmyocardial, and epicardial cell models were validated with published experimental data (124) (Figures

2.2A and 2.2B). With these regional cell types, the ventricular wedge model predicted action potential and ECG properties observed experimentally in WT wedge preparations (260) (Figure 2.2C).

### 2.3.2 G589D mutation prolongs QT and elevates TDR in a rabbit ventricular wedge model

Consistent with whole-cell simulations (189), β-adrenergic stimulation prolongs the QT interval and creates broad T-waves in the G589D mutant but not the WT wedge model, clearly visible on the simulated ECG (Figure 2.3A). Strong β-adrenergic stimulation at low pacing rates triggered small EAD-like responses in the endocardial and midmyocardial regions, but the large EADs seen in single cell simulations appear blunted due to electrotonic coupling. Sympathetic stimulation increases APD in the G589D mutant ventricular wedge heterogeneously (Figure 2.3B), elevating transmural dispersion of repolarization (TDR) at large cycle lengths (Figure 2.3C). TDR is often used as an indicator of arrhythmic risk (236). TDR increased with cycle length in both WT and mutant tissue models, suggesting a protective role for higher heart rates (Figure 2.3C). Increased TDR (from 19 to 39 ms) was also observed in G589D wedge models following a 1.5 second pause from 500 and 333 ms basic cycle lengths.

The likelihood for the G589D proarrhythmic cellular mechanisms to manifest ECG abnormalities appears further increased in simulations of a larger heart. A very large, broad T-wave was observed (Figure 2.3D, second beat), due to strong EADs elicited by endocardial regions (Figure 2.4A). On the subsequent beat, small EADs isolated to a region of midmyocardium and nonuniform refractoriness (Figure 2.4B) cause a bifurcated T-wave with an inverted T2 component (Figure 2.3D, third beat).

Electrotonic coupling appears lower in the larger heart, allowing more irregular repolarization patterns with the G589D mutation.

### 2.3.3 Parallel performance of the MyMPI module

By definition, the operator splitting method replaces the continuous interaction between transmembrane potential "diffusion" and "reaction" with discrete interactions, thus allowing us to solve the ODEs of the ionic model separately from the linear system representing the PDEs. Solution times for the ODEs accounted for 95-99% of the total execution time in the rabbit ventricular wedge with our modified version of the Puglisi-Bers ionic model. Parallelization of the ODEs using the MyMPI module on a distributed memory cluster reduced this fraction to ~75% (Figure 2.5). Further speedup was limited by relatively slow interconnects (Ethernet), the somewhat small problem size, non-dedicated access to computing facilities and additional communication overhead of typecasting between Python and Fortran.

## 2.4 Discussion

### 2.4.1 Mechanisms of arrhythmia formation in the G589D mutation

This study explored the contributions of electrical heterogeneities to mechanisms that may bridge the KCNQ1-G589D gene mutation to aspects of the LQT1 clinical phenotype. Incorporating the molecular consequences of the KCNQ1-G589D defect into a mathematical model of the rabbit ventricular myocyte, we found increased APD and a susceptibility to afterdepolarizations only with sympathetic stimulation (189). However, it is unclear how these proarrhythmic cellular events modify action potential propagation within intact heterogeneous myocardial tissue and manifest ECG abnormalities indicative of serious ventricular arrhythmias. This motivated us to upwardly integrate the cellular model into a model of a rabbit ventricular wedge

preparation. Specifically, we examined the contributions of interactions between these cellular mechanisms, cell-type heterogeneities, and fiber angle distributions to action potential propagation and simulated ECGs. These analyses suggest a mechanistic link from the KCNQ1-G589D gene defect to increased TDR and possible T-wave abnormalities in the ventricle, clinical indicators of arrhythmic risk in the LQT syndrome.

Our results also indicated that electrocardiographic abnormalities were more severe in simulations of action potential propagation in larger hearts. This is consistent with modeling work by Sampson and Henriquez (183). These investigators report that in mouse hearts, electrotonic effects on APD are the primary determinant of dispersion of repolarization, despite the presence of large intrinsic cellular heterogeneities and reduced coupling. As heart size increases, intrinsic heterogeneities increasingly augment repolarization gradients. It is plausible that the same argument can be applied to situations where ion channel defects result in regional APD prolongation.

### 2.4.2 Limitations

A number of limitations in this study must be considered when interpreting the results. While heterogeneities in the myocardium can greatly affect action potential propagation, we have only accounted for the most prominent differences. We have modeled endocardial, midmyocardial, and epicardial myocytes arranged in transmural layers (8), although these cells may not be arranged in distinct layers in the real heart (2). We have modeled fiber angle distributions (237) but not the discontinuous architecture of laminar sheets (100). The experimental perfused-wedge preparation has been used in numerous studies of ventricular heterogeneity and acquired LQTS (12). However, the ventricular wedge used here and in previous experimental work lacks many anatomic and physiologic features of the intact heart. We did not observe

torsades de pointes, perhaps due to the size of our ventricular wedge (260). Despite these limitations, our computational models successfully predicted many known aspects of cardiac excitation-contraction coupling and its regulation by β-adrenergic signaling in rabbit.

Our model of $Ca^{2+}$ handling uses a simplified representation of CICR (56), which is unable to predict stochastic behavior such as $Ca^{2+}$ sparks or the role of $Ca^{2+}$ in the junctional subspace. However, our model is sufficient to predict graded $Ca^{2+}$ release (56), cytosolic $Ca^{2+}$ transients (160), and generation of EADs and DADs (38).

Dispersion of repolarization may also be dynamically altered by the restitution properties of individual myocytes. While we did not conduct a thorough analysis of this phenomenon in the FE model, we did investigate restitution properties of epicardial myocytes at pacing rates ranging from 0.5 to 4 Hz and at various concentrations of isoproteronol (see Appendix A). Briefly, although the model predicted some isoproteronol-induced steepening of the restitution curve at short diastolic intervals, it was not as marked as in experimental preparations (218). The model also failed to predict restitution of intracellular $Ca^{2+}$ release, as observed by Goldhaber et al (62), which we surmise may account for the altered dynamic properties following application of isoproteronol. Specifically, we speculate that steepening of the restitution curve at small diastolic intervals arises in part from elevated diastolic $Ca^{2+}$ (from the previous $Ca^{2+}$ transient) that reduces $I_{Ca,L}$ via a $Ca^{2+}$-dependent mechanism. The application of $\beta_1$-adrenergic agonists increases the rate of intracellular $Ca^{2+}$ uptake in the SR, thereby shortening the $Ca^{2+}$ transient. This will contribute to a steeper dependence of $APD_{90}$ on DI at very short S1-S2 intervals (while $[Ca^{2+}]_i$ is still decreasing) but a flattening at longer DIs (once $[Ca^{2+}]_i$ has returned to diastolic levels).

Heterogeneity of cardiac innervation and expression of signaling proteins may also contribute to arrhythmia (236). Specifically, heterogeneity may arise from 1) a nonuniform distribution of nerve terminals and/or receptors or 2) nonuniform release of signaling molecules such as norepinephrine (NE). From investigations into the anatomy of the cardiac nervous system, it appears that sympathetic nerves follow the common pulmonary artery into the plexus supplying the main left coronary artery, where they are distributed to the myocardium in superficial epicardial layers. Experimental evidence suggests that the overlap in the location of sympathetic nerves and the coronary network extends into the myocardium (271). The distribution of β-adrenergic receptors appears to be nonuniform, with the highest density occurring in the most innervated regions of the heart (34). This results in a transmural gradient of receptor density, decreasing from epicardium to endocardium (34). However, preliminary investigations into the consequences of heterogeneity of adrenergic activation indicated very small differences in TDR (Appendix B). Although local application of NE is likely to elicit a more severe response, it is also somewhat of an unphysiological perturbation.

### 2.4.3 Computational considerations

Experimental investigations have yielded a wealth of quantitative data regarding the function and regulation of cardiac ion channels. As a consequence, models that represent individual ion channels (and consequently whole cell models of ionic currents) are becoming increasingly complex and computationally intensive. Progress in upwardly integrating these cellular models into tissue and organ level models has been hindered by the need to develop efficient algorithms and parallelization techniques to permit timely solution of these large problems.

However, due to the nature of whole cell models, there is considerable potential for the use of parallelization techniques to speed up execution time. The solution of the ODEs is “data parallel” in that the currents passing through the ion channels of a cell in one location can be calculated independently of those occurring within a cell in another location. In data parallel applications, the same computations can be performed on data that is partitioned among several processors. Distributing these calculations over many processors makes feasible the integration of sophisticated ionic models (with large numbers of ODEs) into tissue and organ scale models. As the ODE calculation time grows with the sophistication of the ionic model, the solution of the linear systems do not change size or complexity. Thus for complex ionic models, the data parallel solution of the ODE portion of the problem is also where improvements in speed are most needed.

In order to simulate action potential propagation in larger regions of tissue, a different parallelization approach is required. In this instance, the monodomain equation representing the spread of activation is a partial differential equation. Here, the equations at each point in space are not independent and either algebraic or geometric parallelization can be employed. In algebraic parallelization of the linear solve, the global matrix is factorized on several processors, via a special parallel linear solver, such as the distributed memory version of SuperLU (106), whereas in geometric parallelization methods, as the name suggests, regions of the full mesh are distributed over the processors. The main challenge of such domain decomposition techniques is the assignment of appropriate boundary constraints to the inner non-physical boundaries. This technique requires iteration toward a converged solution with frequent updates at the boundaries.

In control parallelization, instructions (not data) are partitioned to separate processors. This can be used to help overcome the computational hurdles for creating

a functionally integrated model. These problems are typically solved with different time and space scales (87, 137, 232) and therefore require schemes for synchronizing calculations and translating meshes. For smaller spatial scales, as needed for electrophysiological problems, linear hexahedral elements in the finite element method are sufficient for convergence, since higher order elements (e.g. cubic Hermite) are specifically designed to gain enough accuracy with few elements in a mesh and for the solution of higher order differential equations. Control parallelization can be exploited to allow the electrical and mechanical portions of the problem to be solved on different (groups of) processors with carefully developed communication between instances of these major problem classes.

### 2.4.4 Conclusions

In conclusion, electrotonic coupling appears to mask the effects of intrinsic heterogeneities in well-coupled myocardium. These ventricular heterogeneities appear to combine with cellular arrhythmic mechanisms arising from the KCNQ1-G589D gene defect to prolong the QT-interval, increase transmural dispersion of repolarization and promote T-wave abnormalities. Although we successfully employed data parallelization techniques to decrease simulation execution times, further efforts are required to decrease memory requirements for simulations in larger 3D tissue models.

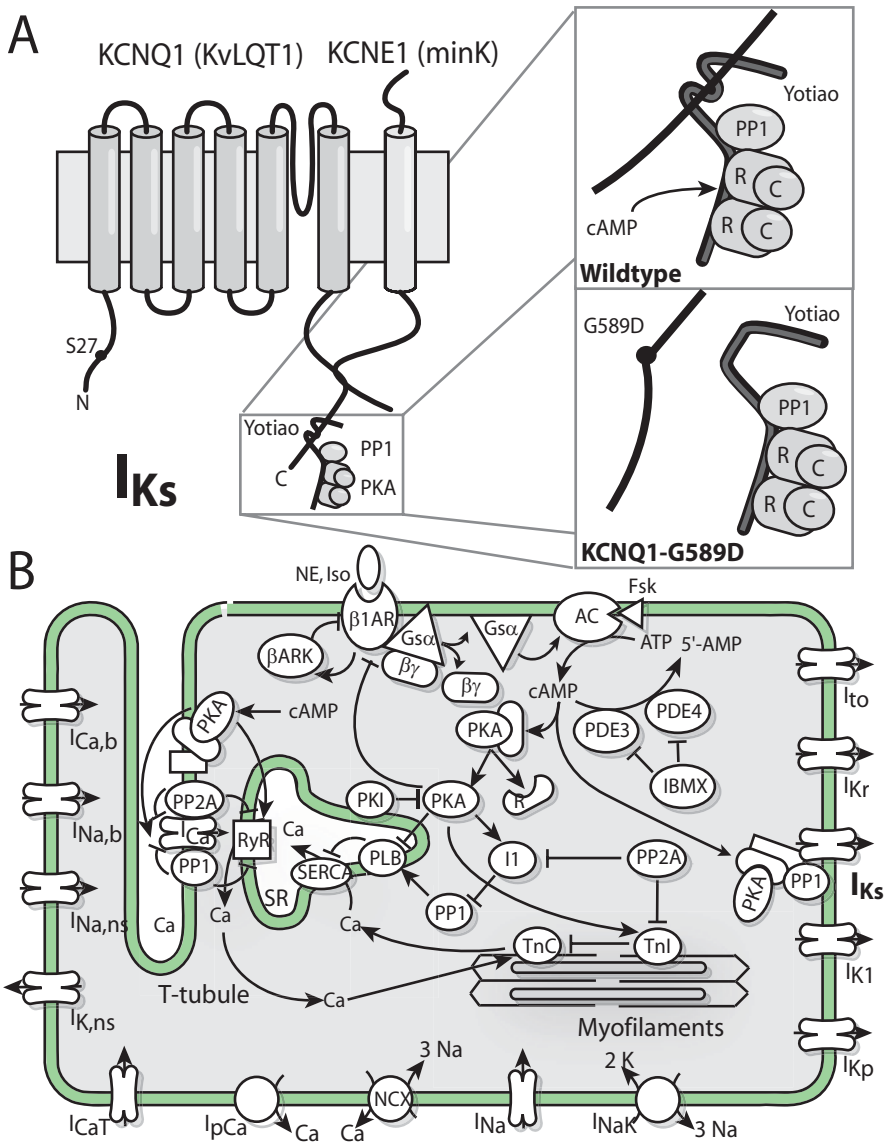


**Figure 2.1:** (A) Known molecular consequences of the KCNQ1-G589D mutation and (B) their incorporation into an integrative computational model of cardiac myocyte $\beta_1$-adrenergic signaling and excitation-contraction coupling. G589D disrupts interaction between KCNQ1 and the scaffolding protein yotiao, which binds protein phosphatase-1 (PP1) and the regulatory subunits of protein kinase A (PKA) (119). The $\beta_1$-adrenergic signaling network acts through cAMP and PKA to regulate phospholamban (PLB), $I_{Ca}$, the ryanodine receptor (RyR), troponin I (TnI), and $I_{Ks}$. The basic signaling and excitation-contraction coupling mechanisms included in the cellular model have been described in detail previously (160, 188, 190).

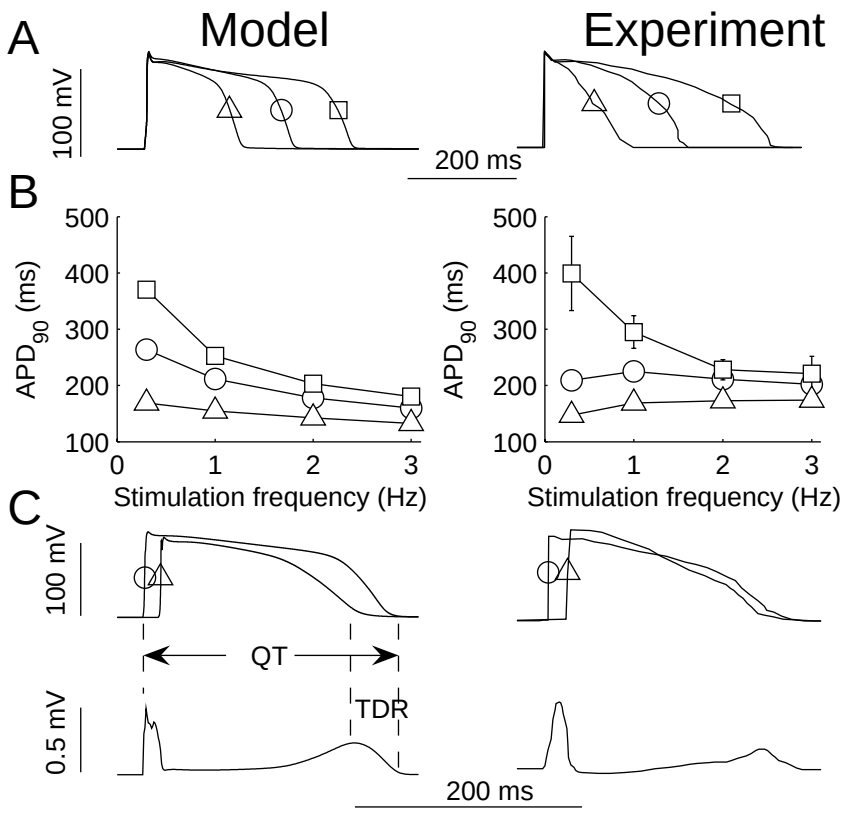


**Figure 2.2:** Validation of WT regional action potential characteristics for both single cell and intact ventricular wedge models. (A) Action potentials from WT endocardial (circles), midmyocardial (squares), and epicardial (triangles) single rabbit myocytes from model (left) and experiment (124) (right) paced at 0.3 Hz. (B) Pacing-rate dependence of $APD_{90}$ for endocardial (circles), midmyocardial (squares), and epicardial (triangles) myocytes in the model (left) and experiment (124) (right). (C) Upper tracings: endocardial (circles) and epicardial (triangles) action potentials from an intact ventricular wedge in the model (left) and experiment (260) (right), paced at 1 Hz. Lower tracings: corresponding ECG for the ventricular wedge in the model (left) and experiment (260) (right). Transmural dispersion of repolarization (TDR, measured from action potentials) and QT interval (measured from the ECG) are shown graphically.

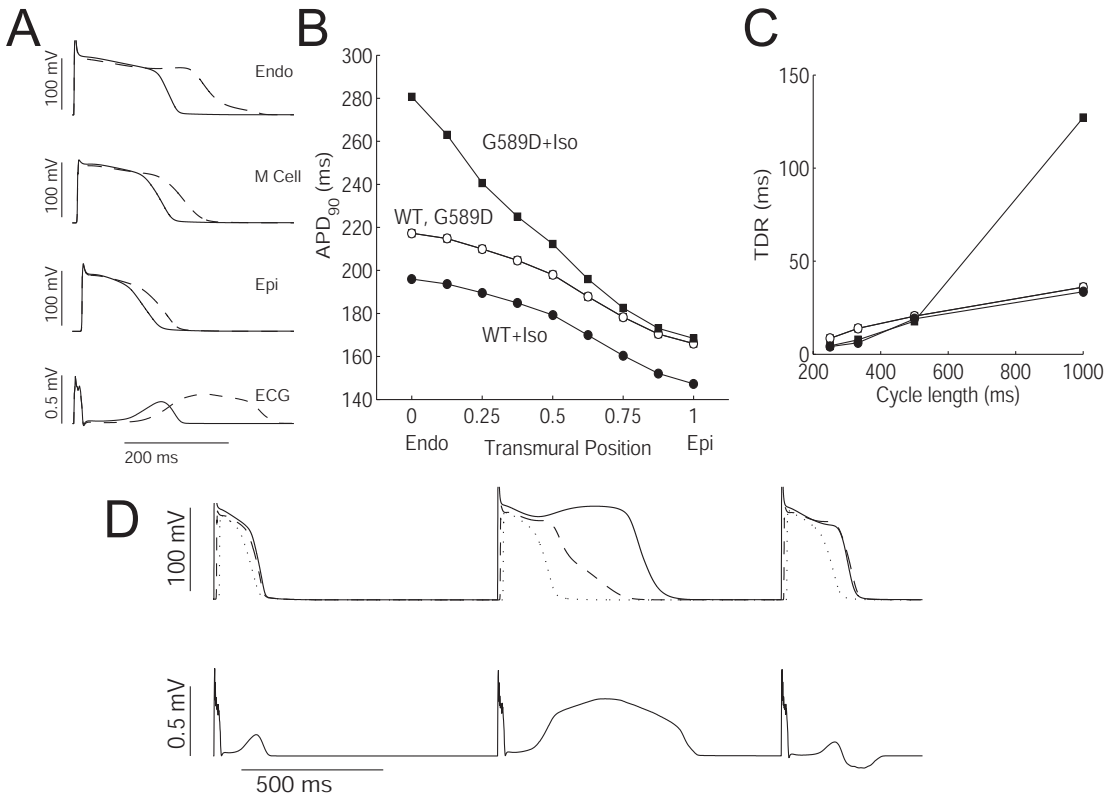


**Figure 2.3:** Role of G589D mutation and β-adrenergic signaling on action potential propagation in a rabbit ventricular wedge model. (A) After 60 seconds of isoproterenol stimulation (1 μmol/L), action potentials prolong in G589D mutants (dashed line) compared with WT (solid line), forming a broad T-wave and prolonged QT interval on the simulated ECG. (B) Transmural heterogeneity of $APD_{90}$ for untreated (empty markers) and isoproterenol-treated (1 μmol/L; filled markers) WT (circles) and G589D mutant (squares) wedges. (C) Transmural dispersion of repolarization is particularly elevated in sympathetic-stimulated G589D mutant models (filled squares) at long cycle lengths. (D) A larger heart decreases electrotonic coupling, allowing a range of possible T-wave abnormalities in isoproterenol-treated G589D mutants. Upper tracing depicts representative action potentials in endocardium (solid line), midmyocardium (dashed line), and epicardium (dotted line); lower tracing depicts the corresponding ECG. BCL = 1000 ms for (A),(B),(D).

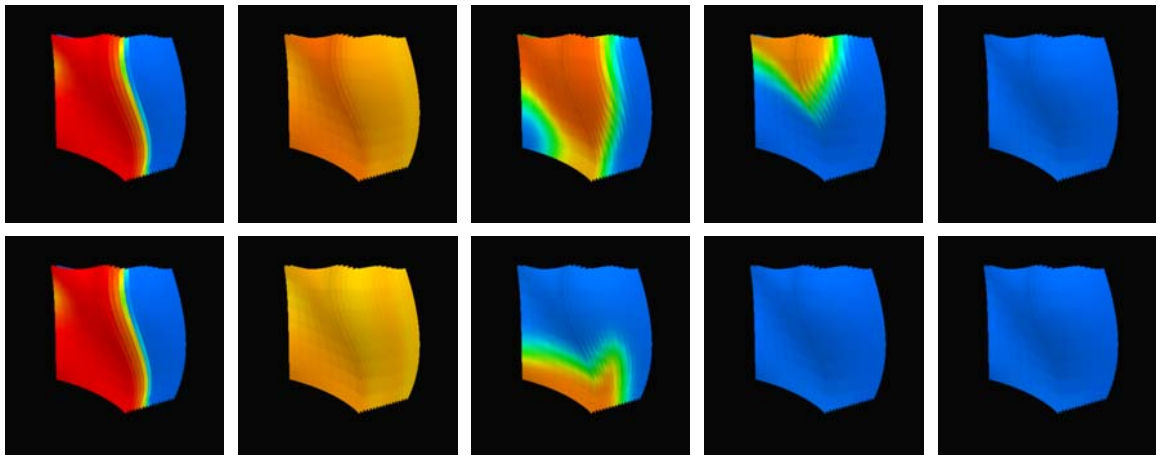

**Figure 2.4:** In a 1.5 × larger heart, the G589D mutation causes greater electrocardiographic abnormalities with isoproterenol, including regional endocardial EADs (upper panel, first beat) and subsequent nonuniform refractoriness (lower panel, second beat).

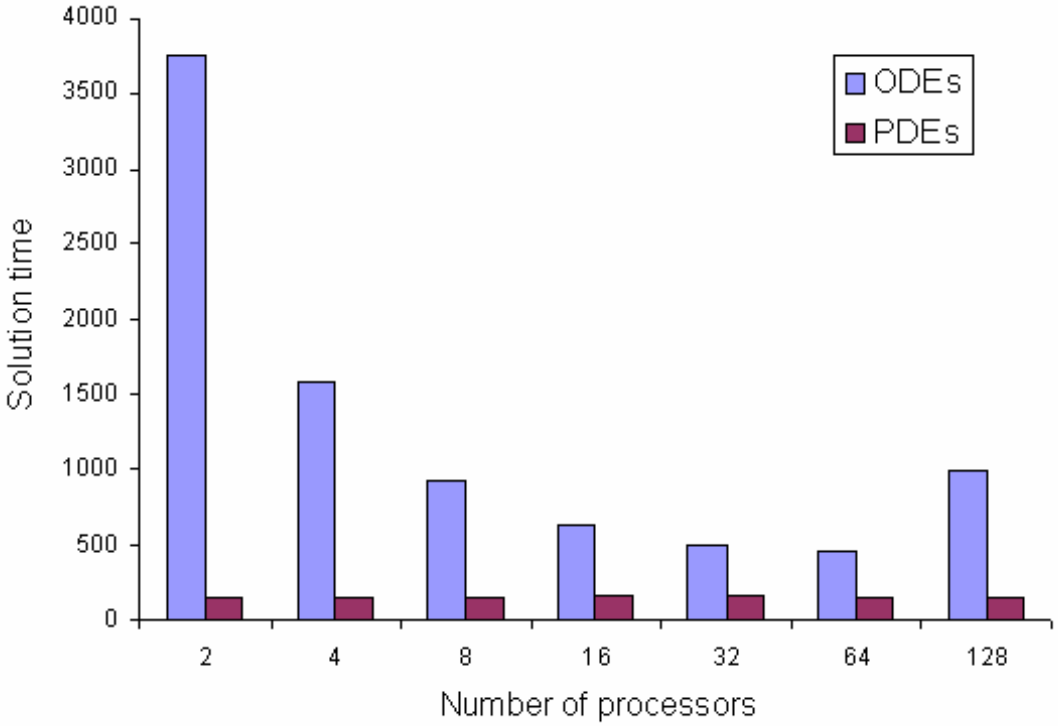


**Figure 2.5:** Solution times in seconds for the parallelized ODE and serial PDE portions of the algorithm. These times represent the solution of the monodomain equation using the Puglisi-Bers ionic model in the 1024 element rabbit ventricular wedge to 250 ms (1 heartbeat).

Part of the text of Chapter 2 is a reprint of the material as it appears in, “Proarrhythmic Consequences of a KCNQ1 AKAP-Binding Domain Mutation: Computational Models of Whole Cells and Heterogeneous Tissue” by Jeffrey Saucerman, Sarah Healy, Mary Ellen Belik, Jose Puglisi and Andrew McCulloch in Circulation Research, Vol 95(12):1216-24, 2004. 

# CHAPTER 3

# Arrhythmogenic consequences of asynchrony and heterogeneity in cardiac myocytes during $\beta_1$-adrenergic stimulation

## 3.1 Introduction

Activation of the sympathetic nervous system (SNS) and the subsequent release of norepinephrine (NE) are implicated in increased arrhythmogenic risk (71, 218). In cardiac myocytes, NE binds to the $\beta_1$-adrenergic receptor, initiating a cascade of signaling events resulting in the phosphorylation of a number of proteins, including the L-type $Ca^{2+}$ channel (LCC), phospholamban (PLB) and the slow activating delayed rectifier $K^+$ channel (IKS), which all play a role in the generation of the action potential and/or $Ca^{2+}$ cycling (26). While β-blockers are highly successful anti-arrhythmic agents, the electrophysiological responses to $\beta_1$-adrenergic agonists and the mechanisms of arrhythmia formation, particularly with respect to temporal and spatial heterogeneities, remain poorly understood.

Autonomic-mediated amplification of spatial heterogeneities of ion channel and $Ca^{2+}$ handling proteins appears to play a leading role in the development of proarrhythmic states, particularly in patients with long QT-1 syndrome (LQT1) (193). Adrenergic stimulation can induce $Ca^{2+}$-mediated afterdepolarizations, both early and delayed, in isolated ventricular myocytes and ventricular myocardial tissue (85, 118, 157, 241), although controversy exists as to the location of vulnerable regions. Furthermore, both experimental (202, 241) and clinical (116) data suggest that application of $\beta_1$-adrenergic agonist elicits dynamic alterations in action potential duration (APD), and indicate that the early response (<60s) is associated with greater

transmural dispersion of repolarization (TDR) than at steady state. The current understanding of $\beta_1$-adrenergic signaling fails to account for these transient observations.

In the previous chapter, we explored how the KCNQ1 mutation G589D resulted in an LQT1 phenotype in a multiscale finite element model. However, we investigated the response only once all phosphorylation states had reached steady-state. Here we investigate the hypothesis that clinical and experimentally observed time-varying responses to $\beta_1$-adrenergic stimulation occur as a result of differences in the time course of phosphorylation of PKA targets. This study also aims to investigate how the dynamic response to $\beta_1$-adrenergic agonists may contribute to arrhythmia formation by spatiotemporal variations in incidences of $Ca^{2+}$-mediated afterdepolarizations, and how these heterogeneities interact with a model of LQT1. We use a previously developed and validated 3D model of a rabbit ventricular wedge with spatially varying electrical properties, which integrates computational models of $\beta_1$-adrenergic signaling, myocyte excitation-contraction coupling (ECC) and action potential propagation. For this study, we investigated the cell and tissue level effects of the temporal variation of PKA phosphorylation and the spatial heterogeneity of calcium uptake into the sarcoplasmic reticulum (SR). Our model predicts asynchronous phosphoregulation of the LCC, PLB and IKS that results in a transient period of increased dispersion of repolarization, and thus vulnerability to reentrant arrhythmias.

## 3.2 Methods

### 3.2.1 Whole cell model of myocyte $\beta_1$-adrenergic signaling and ECC

A mechanistic mathematical model of $\beta_1$-adrenergic signaling has previously been developed (187), adapted for the rabbit ventricular myocyte, and validated at a variety

of functional levels with independent published experimental data obtained, whenever possible, from isolated rabbit ventricular myocytes. The single cell model was modified to adjust the internal triggering of spontaneous $Ca^{2+}$ release from the junctional SR to match experimental observations of dose-dependent isoproterenol-induced DADs (157), such that DADs rarely occur with a concentration 10 nmol/L but occur in all cell types at many frequencies with 100 nmol/L.

### 3.2.2 Transmurally heterogeneous rabbit ventricular wedge model

To simulate the electrophysiological effects of $\beta_1$-adrenergic stimulation at the heterogeneous multi-cellular tissue scale, we used a previously developed 3D finite-element model of a rabbit left ventricular wedge (Figure 3.1), which was sufficiently refined to obtain solutions for conduction velocity and APD that were both converged to within 1% (189). Briefly, transmural heterogeneity in the wedge was incorporated using endocardial, midmyocardial and epicardial layers with relative thicknesses of 3:3:2. Relative current densities in each region were estimated from rabbit (endocardial/epicardial data for the ionic currents $I_{Ks}$ (256), $I_{Kr}$ (256), and $I_{to}$ (123); endocardial/midmyocardial/epicardial $I_{Na}$ estimated from upstroke velocity (124)) or when necessary canine ($I_{Kp}$ (8), midmyocardial $I_{Ks}$, $I_{Kr}$ and $I_{to}$ (8)). To account for a possible transmural gradient of SR $Ca^{2+}$-ATPase expression reported in canine ventricular myocytes (94), maximum SR uptake rate was increased from 4.0 mmol/L/s to 6.0 mmol/L/s in epicardial cells only. This regional variation was derived from differences in the time constants of $Ca^{2+}$ transient decline observed between endocardial and epicardial myocytes following application of isoproteronol (ISO), taking into account species differences in APD. Simulations were performed using a collocation-Galerkin finite element method (172) and executed in parallel on 32 dual CPU nodes of a Linux cluster. All measurements of electrophysiological function

were consistent with the experimental results performed in arterially perfused rabbit wedge preparations of similar size at 1 Hz. The 3D wedge model upwardly integrates the cellular ionic model described above including time-varying phosphorylation levels of PKA targets computed from the signaling model (189).

### 3.2.3 Data analysis

The APD was measured at 90% repolarization. TDR was defined as the difference in repolarization time between the first and last cells to return to a resting state along a line from epicardium to endocardium in the middle of the wedge. All electrophysiological measurements from the wedge model were performed after a minimum of 3 beats to allow the model to reach steady-state. A pseudo-ECG was calculated using the method of Gima and Rudy (61). Early afterdepolarizations (EADs) were defined as the re-occurrence of a positive gradient of the transmembrane potential ($V_m$), whereas delayed afterdepolarizations (DADs) were identified by spontaneous release of SR $Ca^{2+}$ during the diastolic interval. In single cells for a given time period, the rate of DAD occurrence was averaged over a period of 10 seconds at constant phosphorylation states. In the wedge model, DAD frequencies were measured over 3 beats and represent the volume averaged regional incidences of DADs. The model of LQT1 was developed previously (189).

## 3.3 Results

### 3.3.1 Transient APD prolongation following application of isoproteronol

At most pacing rates and for all myocyte subtypes (endocardial, midmyocardial, epicardial), predicted APD transiently increased 5-10 seconds after application of isoproterenol (10 nmol/L), although it decreased below baseline once a steady-state had been reached (Table 3.1). The magnitude of the transient APD prolonging

response appeared to be dependent on rate and myocyte subtype, with the greatest effects observed at slow pacing rates in the midmyocardial cell model. No transient APD prolongation was observed in any myocyte subtype at 4 Hz.

### 3.3.2 Asynchronous PKA target phosphoregulation

The whole cell model of $\beta_1$-adrenergic signaling and ECC predicted faster phosphorylation of LCC and IKS than that of PLB (Figure 3.2A), contributing to a transient increase in APD (Figure 3.2B) in a model of a normal ventricular myocyte paced at 2Hz with ISO = 10 nmol/L. Preventing LCC phosphorylation in the model resulted in a monotonic decrease in APD and diastolic $Ca^{2+}$, with only a small increase in systolic $Ca^{2+}$, whereas preventing PLB phosphorylation attenuated the steady-state decrease in APD and eliminated alterations in diastolic $Ca^{2+}$. IKS phosphorylation appears to play a strong role in constraining both APD and systolic $Ca^{2+}$. Similar transient results were obtained in the 3D wedge model (Figure 3.2C) measured at 10 and 60 seconds after ISO. Preventing LCC phosphorylation in the model monotonically decreased TDR and QT interval, whereas preventing PLB phosphorylation eliminated much of the steady-state decrease in TDR and QT interval, further implicating the opposing action of these targets as contributing to the dynamic repolarization response. Results from preventing IKS phosphorylation resulted in complex patterns of afterdepolarizations and are not shown here.

### 3.3.3 Receptor desensitization

Experimental data from a canine ventricular wedge demonstrates QT interval prolongation and elevated TDR 2 minutes after isoproteronol (100 nmol/L), in the presence of d-Sotalol (100 μmol/L), a blocker of the rapidly activating delayed rectifier $K^+$ current (202). Model predictions of electrophysiological function from the

rabbit ventricular wedge model were in qualitative agreement with these results. These responses occur much later than those measured due to asynchronous phosphoregulation and are consistent with the time course of $\beta_1$-adrenergic receptor desensitization (Figure 3.3).

### 3.3.4 Spontaneous SR $Ca^{2+}$ release

The beat-to-beat induction of EADs and DADs by ISO (20 nmol/L) in a midmyocardial cell model paced at 1 Hz is shown in Figure 3.4 along with predicted tracings of cytosolic and junctional SR $Ca^{2+}$ concentrations and $I_{CaL}$, the LCC current, to illustrate the various mechanisms of $Ca^{2+}$-induced $V_m$ abnormalities. EADs were initially observed 5-10 seconds after agonist stimulation, followed by a period of concurrent occurrence of DADs and EADs. This $V_m$ tracing closely matches measured data from an isolated ventricular myocyte at similar pacing rate and ISO dose (241), in which EADs and DADs also commenced within the first 10 seconds and occurred concomitantly. EADs occurred by either reopening of the LCC, spontaneous release of $Ca^{2+}$ from the SR, or both, whereas DADs resulted exclusively from spontaneous SR release.

### 3.3.5 Asynchrony of PKA target phosphoregulation elicits complex patterns of spontaneous $Ca^{2+}$ release and contributes to ECG abnormalities

The cellular model predicts frequent incidences of DADs in all myocyte subtypes (Figure 3.5A), although midmyocardial myocytes appear more vulnerable earlier on (at 20 seconds), whereas epicardial myocytes are more susceptible to DADs closer to steady-state, particularly at faster pacing rates. This prediction is consistent with asynchrony of PKA target phosphorylation: the initial rapid increase in LCC

phosphorylation increases $Ca^{2+}$ influx, contributing to increased APD while also elevating the risk of DADs during the initial phase, particularly for those myocyte subtypes and conditions with intrinsically long APDs (slow rates, endocardial and midmyocardial). Conversely, PLB phosphorylation is likely to be the dominant mechanism of increased DAD vulnerability in epicardial myocytes, and thus the incidence of epicardial DADs lagged behind those of the other regions. EADs were observed at slow pacing rates in the single midmyocardial cell model only, and no EADs were observed in the 3D model (data not shown).

Predictions from the rabbit ventricular wedge model were also consistent with this hypothesis (Figure 3.5B), although electrotonic coupling played a significant role, modifying regional APD and hence altering expected regions of vulnerability. In the wedge model, the endocardium is the site of the longest APD, and thus in the early response at slow rates, it is the location most vulnerable to DADs. Once again at steady-state, the epicardium was the most vulnerable to DADs at all pacing rates.

Following application of ISO, T-waves are generally larger and TDR is increased, owing to nonuniform APD prolongation (Figure 3.6). At 20 seconds, afterdepolarization-mediated U-waves begin to appear that merge with the T-wave but do not affect repolarization on subsequent beats. There is also evidence of slight rate dependence of U-Wave formation. In order to investigate this more closely, the AP tracings from the WT 2 Hz model at 60 seconds are displayed above the corresponding ECG (Figure 3.7A) which indicate that the T and U waves merge due to epicardial DADs preceding endocardial repolarization. The decrease in DAD coupling interval increases the frequency of DADs such that they can influence the subsequent patterns of repolarization, leading to a frequency dependent susceptibility to T-wave alternans. Late endocardial DADs in LQT1 shorten the APD of the

subsequent beat which reverses the repolarization sequence and leads to prominent T-Wave alternans (Figure 3.7B).

## 3.4 Discussion

### 3.4.1 Intrinsic spatial heterogeneities contribute to regions of increased arrhythmic risk

Regional heterogeneities of ion channel expression contribute to the amplitude and direction of the electrocardiographic T-Wave (9), whereas transmurally varying SR $Ca^{2+}$-ATPase expression at least partly accounts for nonuniform $Ca^{2+}$ transients (45). Adrenergic stimulation appears to amplify these heterogeneities and play a leading role in the development of an electrically unstable substrate. This is especially true for patients with inherited conditions such as long QT-1 syndrome (LQT1) (193) and catecholaminergic polymorphic ventricular tachycardia (95), who are particularly vulnerable to sudden cardiac death during SNS activation. These conditions are characterized by serious ventricular arrhythmias associated with elevated sympathetic tone that occur in the absence of any significant morphological abnormalities. Model predictions in this investigation suggest that intrinsic spatial heterogeneities play a role in increasing regional arrhythmic risk, as evidenced by T-Wave alterations and regionally varying incidences of afterdepolarizations.

### 3.4.2 Temporal asynchrony of PKA target phosphorylation may underlie dynamic repolarization response

$\beta_1$-adrenergic agonists elicit a much slower response than parasympathetic influences since they require the action of second messengers. In the past, investigators have typically considered only steady-state responses to ISO (31, 70, 71, 89, 91, 112, 126), which correspond to a time period when phosphorylation states are

no longer changing. While the findings of Shimizu and Antzelevitch (202) clearly demonstrate a dynamic repolarization response following application of $\beta_1$-adrenergic agonist, this appears to result from receptor desensitization. However, others have reported initial APD prolongation in isolated ventricular myocytes (241). Furthermore, a transient increase in QT interval was observed in 12 out of 25 normal subjects following isoproterenol infusion (116). In the same study, no transient increase in QT interval was observed for exercise, indicating that this phenomenon was not linked to a chronotropic response. Our model predicts that asynchronous PKA phosphoregulation may underlie this transient heterogeneous APD prolongation and increased TDR. The transient response may increase dispersion of repolarization sufficiently to predispose the tissue to reentry.

A dynamic response to $\beta_1$-adrenergic stimulation does not appear to be limited to ventricular myocardium or electrophysiological function. McConville et al (121) recently demonstrated a close correlation between the magnitude and time course of inotropic and metabolic responses to norepinephrine in a perfused rabbit heart, which both precede the chronotropic response. They also noted a transient maximal inotropic response, as measured by left ventricular diastolic pressure, that monotonically decreased to a steady-state. Since PKA also phosphorylates the contractile protein troponin I, it is conceivable that temporal asynchrony of PKA phosphoregulation may also underlie this transient response.

### 3.4.3 Temporal and spatial heterogeneities may contribute to arrhythmia formation and destabilization in intact ventricular tissue

Patients with decreased parasympathetic tone and increased sympathetic activity have a higher risk for developing lethal ventricular arrhythmias. Although $Ca^{2+}$-mediated afterdepolarizations have long been associated with SNS activation,

substantial controversy exists regarding the location of vulnerable regions within the transmurally heterogeneous ventricle. Using optical mapping of a canine ventricular wedge, Laurita et al (94) demonstrated catecholamine-induced triggered activity mediated by DADs localized predominantly near the endocardium, although Zhang et al (264) using monophasic action potential recordings observed only midmyocardial EADs. Furthermore, Nam et al (133) demonstrated that the origin of ectopic activity after application of ISO could spontaneously shift from the endocardium to the epicardium, reversing the sequence of activation, greatly increasing TDR, and creating an electrical substrate capable of induction of polymorphic ventricular arrhythmias.

Here we predict labile T and U wave morphologies that occur as a result of temporal and spatial heterogeneities. The model results of increased T-Wave amplitude and width are consistent with experimental results following SNS activation and this phenotype has been shown to precede some spontaneous ventricular tachyarrhythmias (203). We also observe pathophysiological T-wave notches, similar to those observed in canine ventricular wedges, which can occur by merging of the T and U waves (afterdepolarizations occurring in some regions while other regions are repolarizing). Controversy still surrounds the cellular mechanism underlying the formation of the U-Wave and if indeed U-waves exist (259). A popular theory is that the U-wave represents delayed afterdepolarizations arising from stretch of the ventricular myocardium. In general, bradycardia-dependent augmentation of U-waves is observed in healthy controls (216), consistent with the mechanoelectrical theory in that slower rates allow greater filling of the ventricles. However, the frequency dependence of U-wave amplitude reverses with application of isoproteronol (115). Our results consistently implicate afterdepolarizations as strongly contributing to U-waves during SNS activation, and we speculate that the *in vivo* response is likely to result from a combination of both mechanical and adrenergic effects.

Variations in electrotonic coupling, activation sequence and repolarization reserve are likely to modify these predictions and may contribute to the discrepancies in the cited experimental results. Electrotonic coupling has previously been shown to minimize intrinsic regional differences in APD to a degree dictated by the strength of the coupling (182) and the sequence of activation can further modify dispersion of repolarization via heterogeneity of electrotonic loading (prolonging the APD in regions of wavefront spread and decreasing the APD in regions of wavefront collision) (184). We have demonstrated here that electrotonic effects can alter predicted regional incidences of DADs by increasing the risk of endocardial DADs, and decreasing those in the midmyocardium. Although not explicitly investigated, it is plausible that a decrease in electrotonic coupling might increase midmyocardial APD until EADs were localized in this region, as in the experiments of Zhang et al (264), but that a decrease in repolarization reserve may increase APD uniformly to an extent where the endocardium remains the most vulnerable region, consistent with the experiments of Laurita et al (94), which were indeed performed in the presence of the $K^+$ channel blocker, clofilium. Reduced repolarization reserve may also increase the probability of a DAD-induced action potential.

### 3.4.4 Experimental validation of asynchronous phosphoregulation

We have found no direct experimental evidence in the literature demonstrating temporal asynchrony of PKA-mediated phosphorylation. However, preliminary data from our laboratory with FRET biosensors of PKA activity show >10 s delay in cytosolic substrate phosphorylation compared with membrane-targeted substrates in neonatal cardiac myocytes (191). Although this constitutes a somewhat limited experimental basis for the underlying hypothesis of this work, many experimental and clinical investigations indicate temporal variation in response to $\beta_1$-adrenergic

agonists. Here we explore the hypothesis that an asynchronous signaling response may at least in part account for these currently inexplicable results.

### 3.4.5 Limitations

In this study, we have neglected to include the Purkinje system, which is thought to respond to SNS activation by increasing automaticity, shortening APD and enhancing slow action potential formation in depolarized Purkinje fibers (208). It is possible that in prior investigations, Purkinje cell afterdepolarizations may have been mistakenly deemed to be of an endocardial origin.

The increased epicardial expression of the SR $Ca^{2+}$-ATPase has only been reported in canine. It is possible that this is species-specific and the extrapolation to rabbit is inaccurate. In addition, the whole cell model ignores $\beta_1$-adrenergic effects on the $Na^+$ channel, which have been shown to alter conduction velocity in a $V_m$-dependent manner(266).

### 3.4.6 Conclusions

We have investigated the hypothesis that clinical and experimentally observed time-varying responses to $\beta_1$-adrenergic stimulation occur as a result of differences in the time course of phosphorylation of PKA targets. Although direct experimental validation of the temporal variation in phosphoregulation of downstream targets differences is scarce, our model is able to recapitulate 1) transient increases in APD in response to ISO; 2) the temporal pattern of EAD and DAD formation in isolated rabbit ventricular myocytes; and 3) the clinically observed reverse in frequency-dependence of U-waves with $\beta_1$-adrenergic activation.

**Table 3.1:** Baseline (before ISO), maximal and steady-state APDs

| | Baseline $APD_{90}$ (ms) | | | Maximal $APD_{90}$ (ms) | | | Steady-state $APD_{90}$ (ms) | | |
|---|---|---|---|---|---|---|---|---|---|
| Freq (Hz) | Endo | Mid | Epi | Endo | Mid | Epi | Endo | Mid | Epi |
| 0.5 | 276 | 389 | 206 | 322 | 510 † | 214 | 245 | 402 † * | 194 * |
| 1 | 226 | 276 | 185 | 266 | 503 † | 197 | 193 | 244 * | 163 * |
| 2 | 188 | 215 | 160 | 202 | 241 | 167 | 165 | 190 | 135 * |
| 3 | 170 | 192 | 145 | 172 | 196 | 146 | 152 | 170 | 121 * |
| 4 | 157 | 176 | 135 | 157 | 176 | 135 | 141 | 156 | 114 * |

* DADs present

† EADs present

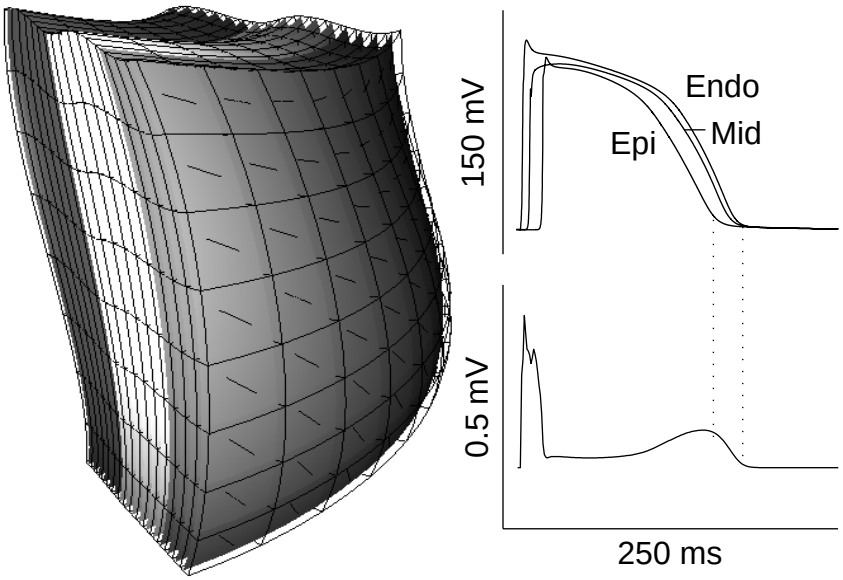


**Figure 3.1:** Rabbit ventricular wedge finite element model with distinct transmural layers (endocardium, dark grey; midmyocardium, white; epicardium, light grey) and variation in fiber orientation. Action potential traces from sites along the midline of the wedge are shown with the corresponding pseudo ECG to demonstrate the influence of electrotonic coupling and intrinsic cellular heterogeneities on the activation and repolarization sequence in intact tissue. Epicardial repolarization corresponds to the peak of the T-wave and endocardial repolarization to the end of the T-Wave. Pacing rate = 3 Hz.

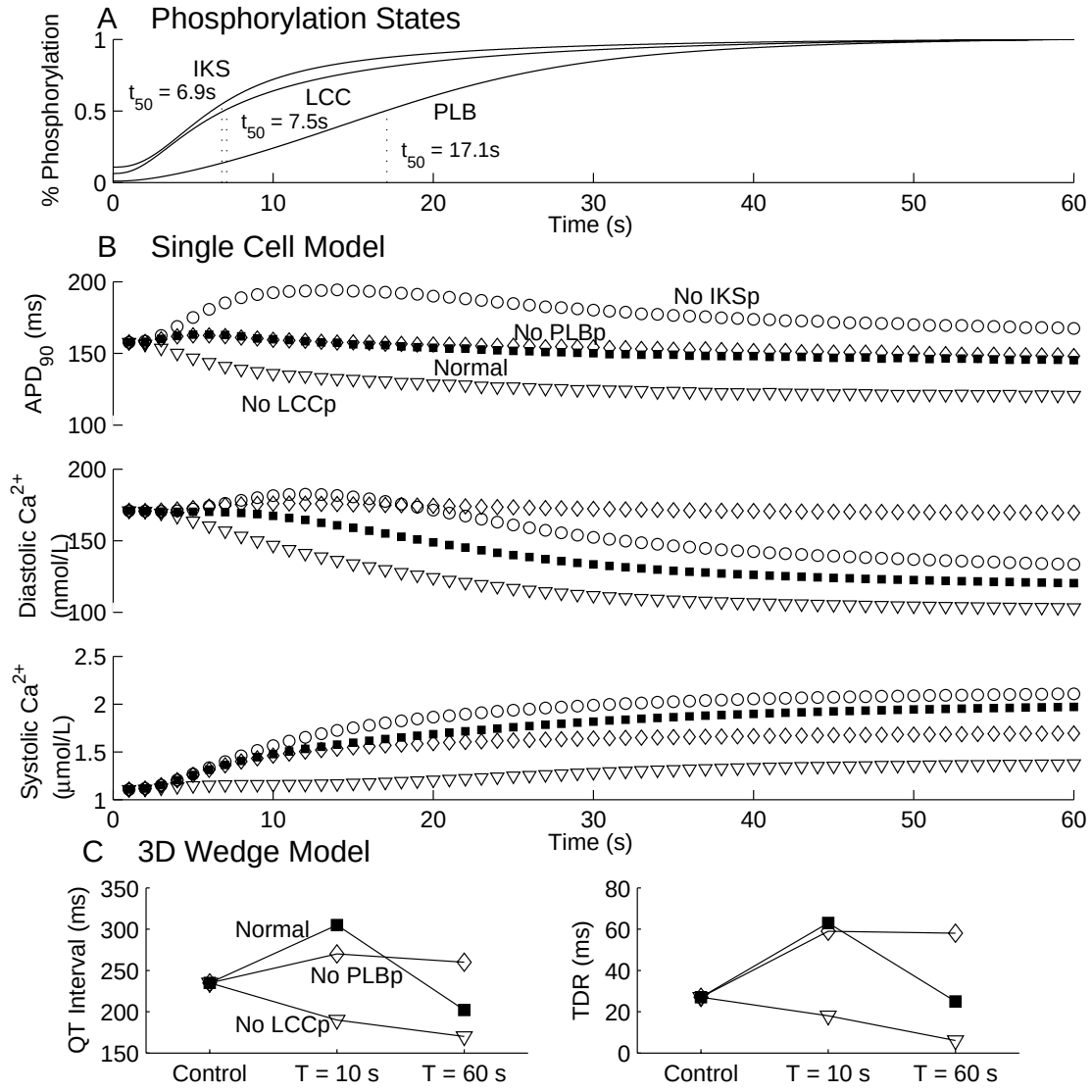


**Figure 3.2:** (A) Asynchronous phosphorylation of PLB, IKS and LCC as evidenced by varying $t_{50}$ values. (B) Corresponding beat-to-beat alterations in APD, diastolic $Ca^{2+}$ and systolic $Ca^{2+}$ over the first 60 seconds following simulated application of ISO (10 nmol/L) for a generic rabbit ventricular myocyte at 2 Hz. Normal APD, diastolic $Ca^{2+}$ and systolic $Ca^{2+}$ (■) are a result of opposing effects of PKA target phosphorylation, as evidenced by the substantial differences when phosphoregulation is systematically removed from each of IKS (○), PLB (◊) and LCC (▽). Data are shown from every second beat only for clarity. (C) Electrophysiological measurements from the 3D wedge model paced at 1Hz with 100 nmol/L ISO (■). Preventing LCC phosphorylation eliminates the transient increase in QT interval and TDR (■) whereas preventing PLB phosphorylation (□) attenuates the steady-state response.

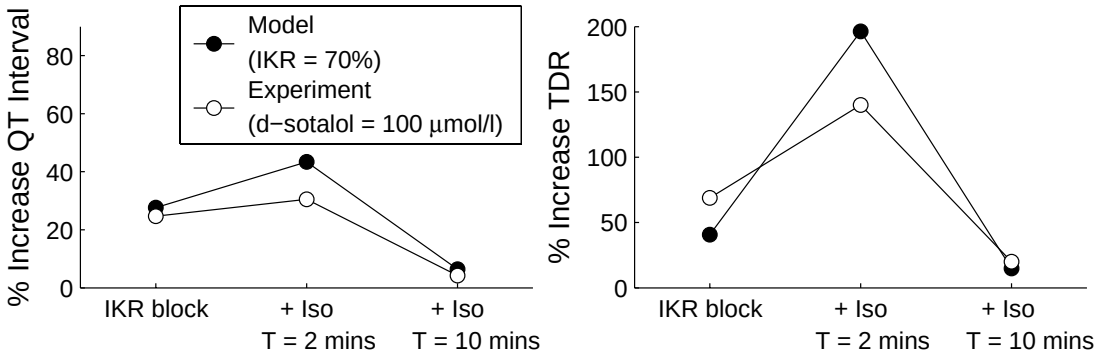


**Figure 3.3:** Experimental data from a canine ventricular wedge demonstrating QT interval prolongation and elevated TDR 2 minutes after isoproteronol in the presence of an IKR blocker d-Sotalol (202). Model predictions of QT interval and TDR with 30% IKR block demonstrate similar trends which are due to $\beta_1$-adrenergic receptor desensitization.

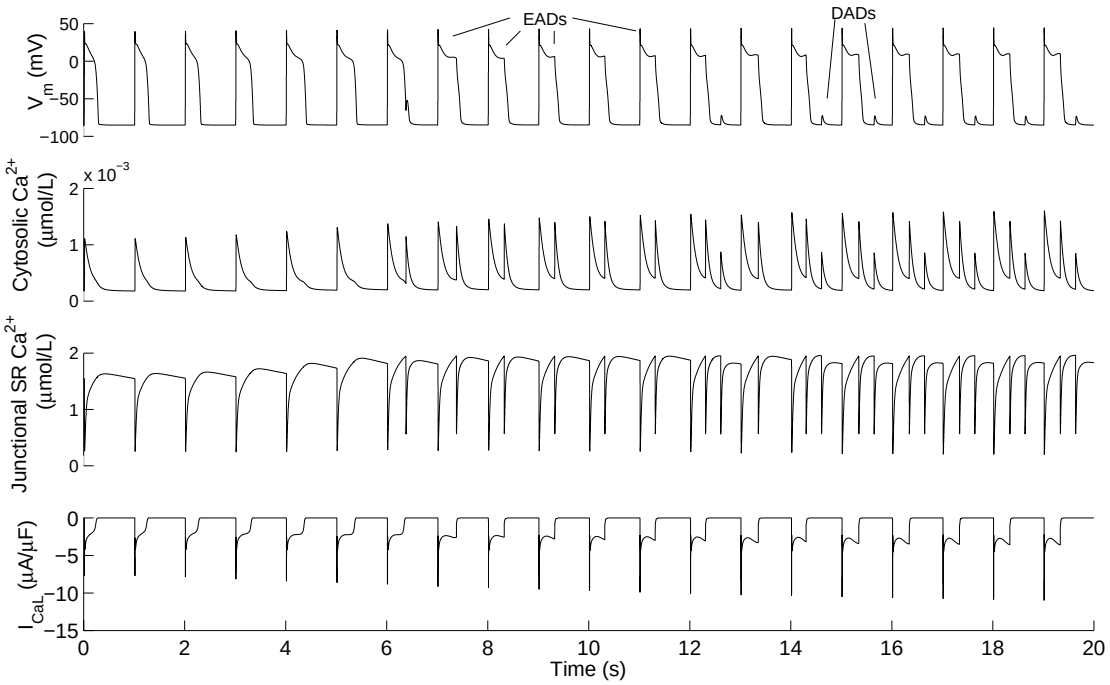


**Figure 3.4:** Induction of EADs and DADs by ISO (added at time = 0 s) in a midmyocardial cell. AP tracings are similar to recordings by Volders et al (241). ISO: 20 nmol/L; Pacing frequency: 1 Hz.

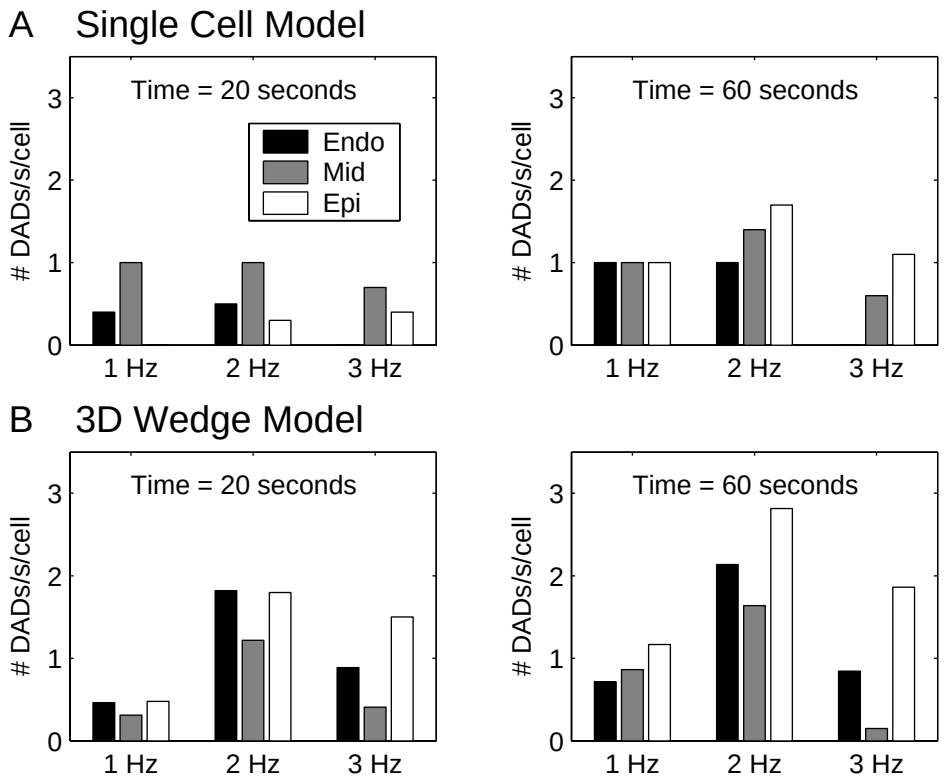


**Figure 3.5:** Frequency of spontaneous SR $Ca^{2+}$ release resulting in DADs in (A) single ventricular myocytes and (B) the 3D wedge model grouped by pacing frequency (1, 2 and 3Hz), demonstrating the effect of electrotonic coupling on regional incidences of DADs. Results are shown at a transient state (20 seconds) and steady state (60 seconds). ISO: 1 μmol/L.

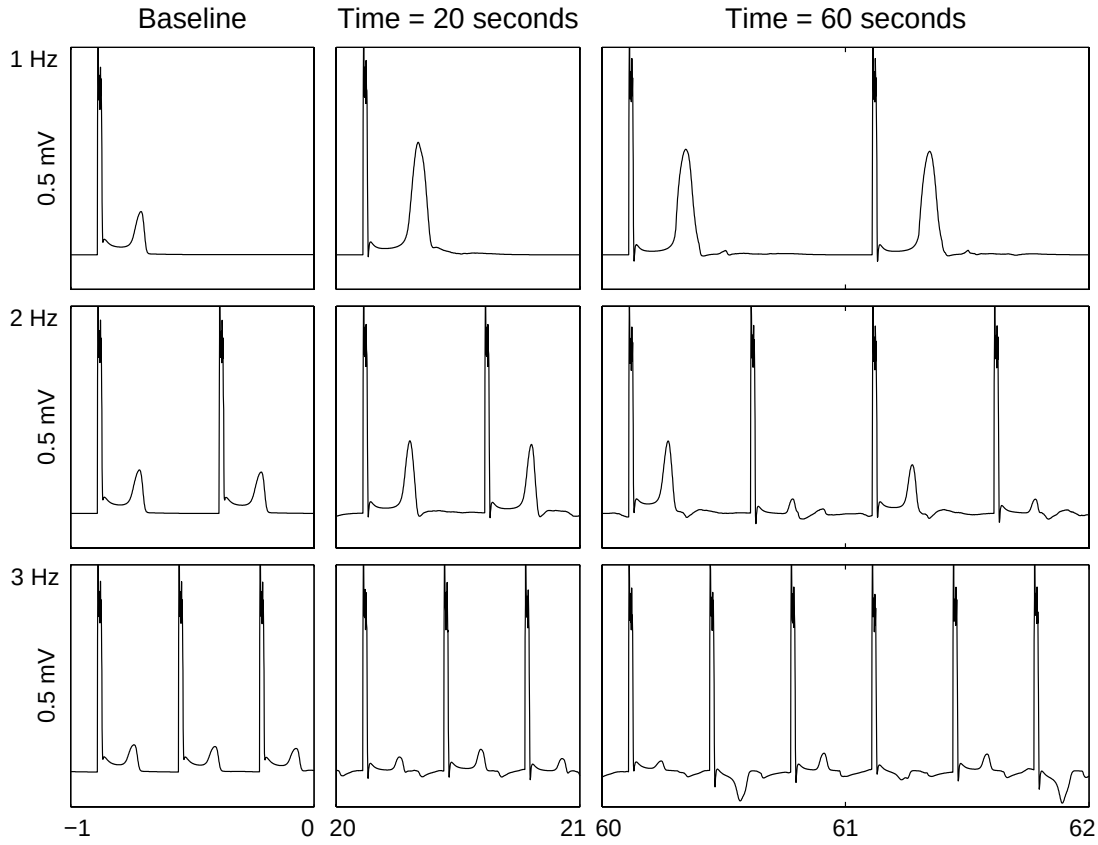


**Figure 3.6:** ECG tracings from the rabbit ventricular wedge model at baseline, 20 seconds after application of ISO and 60 seconds after application of ISO at pacing rates of 1, 2 and 3 Hz. Note that the model predicts a frequency dependent increase in T-Wave amplitude and area (greatest at slow pacing rates). U-waves begin to appear after isoproteronol application, although the T and U waves become difficult to distinguish at higher frequencies. At steady state with pacing at 3Hz, T-Wave alternans is observed. ISO: 1 μmol/L.

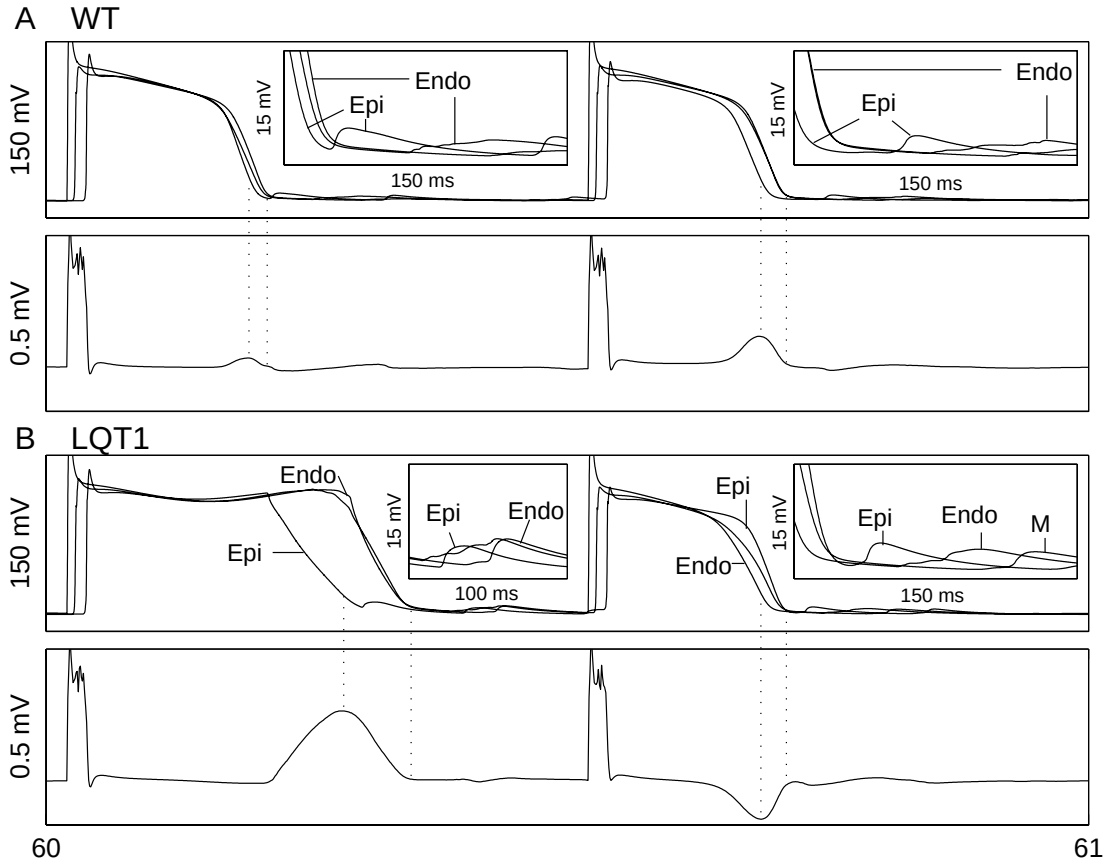


**Figure 3.7:** AP traces of (A) the WT model and (B) an LQT1 model at 60 seconds demonstrating regionally varying incidences of DADs which influence the morphology of the electrocardiographic T-Waves and U-Waves. Insets show magnified view of repolarization sequence and DADs.

The text of Chapter 3, entitled “Arrhythmogenic consequences of asynchrony and heterogeneity in cardiac myocytes during $\beta_1$-adrenergic stimulation” by Sarah Flaim, Jeffrey Saucerman, and Andrew McCulloch is a reprint of the material as it was submitted to Circulation Research.

# CHAPTER 4

# Contributions of sustained $I_{Na}$ and $I_{Kv43}$ to transmural heterogeneity of early repolarization and arrhythmogenesis in canine left ventricular myocytes

## 4.1 Introduction

Significant differences in the expression patterns of a number of ion channels is an important functional distinction among cells isolated from the left ventricular endocardium, epicardium and midmyocardium of many species, including human (54, 105), dog (16, 204), guinea pig (16), rabbit (124) and mouse (30). The major consequence of this systematic variation in ionic currents is a corresponding heterogeneity of action potential duration (APD), waveform and rate-dependence (105). It is hypothesized that these so-called intrinsic electrophysiological differences are responsible for a normal sequence of activation and repolarization in healthy hearts. Moreover, either exaggeration or significant reductions of repolarization heterogeneities, due to drug actions, inherited mutations or acquired disease, may be proarrhythmic. Experimental studies in ventricular myocytes have begun to define the molecular and ionic mechanisms underlying the transmural heterogeneities of ion channel and calcium ($Ca^{2+}$)-handling proteins. A relatively extensive data set is now available for the canine ventricular myocardium. The ionic currents which are known to exhibit transmural heterogeneities include: the transient outward potassium ($K^+$) current, $I_{Kv43}$(110); the slowly activating delayed rectifier $K^+$ current, $I_{Ks}$(109); the late sodium ($Na^+$) current, $I_{NaL}$(273); the $Na^+$-$Ca^{2+}$ exchanger, $I_{NaCa}$ (255, 274); and the SR $Ca^{2+}$-ATPase uptake rate, $I_{SERCA}$. (93). Important unresolved questions concerning the functional importance of these transmural heterogeneities remain.

This study was motivated by the possibility that we could integrate data concerning (i) known heterogeneities, to determine if they are sufficient to explain the distinct action potential waveforms; and (ii) information regarding known interactions between the subunits comprising an ion channel, to reproduce channel function within intact myocytes and explore the functional roles of these interactions. Computational modeling provides a useful framework with which to integrate extensive experimental data and develop specific working hypotheses to guide quantitative investigations into these unresolved questions.

The ionic mechanisms responsible for the intrinsically long APDs and pronounced rate-dependence of midmyocardial myocytes in the left ventricle have been the focus of many experimental investigations (9). Most previous hypotheses have been centered on the relatively large $K^+$ outward currents that are responsible for late repolarization (Phase 3). However, evidence is emerging that some currents previously measured and defined as being transient (such as both $I_{Na}$ and $I_{Kv43}$) modulate APD as a consequence of their smaller slowly inactivating or sustained components. The relatively high resistance of the ventricular action potential plateau provides a substrate in which these small net currents can modulate the AP waveform (209). In this study, we have investigated the hypothesis that these two currents can contribute substantially to early repolarization. As such, transmural differences in these currents may lead to increased APD and arrhythmogenic risk of midmyocardial myocytes.

Intracellular $Ca^{2+}$ cycling is an important regulator of normal and abnormal excitation-contraction coupling (ECC) (26). In the myoplasm, $Ca^{2+}$ binds to regulatory molecules, such as calmodulin, and thereby can modify ion channel function on a beat-to-beat basis or over longer time periods (149). Furthermore, $Ca^{2+}$-mediated early afterdepolarizations (EADs) can facilitate the development of potentially life-

threatening reentrant arrhythmias by increasing transmural dispersion of repolarization. In an effort to create a mechanistic yet computationally efficient model of $Ca^{2+}$ cycling in the cardiac ventricular myocyte, Hinch et al (75) used a method based on time scale decomposition to simplify continuous-time Markov chain descriptions of L-Type $Ca^{2+}$ channel (LCC) and ryanodine receptor (RyR) gating. This resulted in a low order system of ordinary differential equations (ODEs) representing the ensemble behavior of the so-called $Ca^{2+}$ release units (comprising 1 LCC and 5 RyRs) while also retaining many key biophysical properties (75). Greenstein et al (65) generalized this approach to allow LCC and RyR models of arbitrary complexity, and combined this model with their equations for ionic currents in canine midmyocardial myocytes. The resulting whole cell model was shown to faithfully reproduce features of LCC voltage and $Ca^{2+}$ sensitivity, ECC, and action potential and $Ca^{2+}$ cycling properties of a canine midmyocardial myocyte (65).

The time- and voltage-dependent properties of the Kv4.3 channel current are now known to be much more complex than previous models accounted for. This is, at least in part, due to accessory β subunits, such as the $K^+$ Channel Interacting Proteins (KChIPs). Specifically, KChIP isoforms both promote cell surface expression and modify gating kinetics (148). Furthermore, it has been suggested that the steep transmural gradient of KChIP expression may contribute to the heterogeneous measurements of $I_{Kv43}$ across the canine left ventricular wall (174, 269). Patel et al (148) propose that once Kv4.3 channels transition to the open-state, inactivation can occur via two distinct mechanistic pathways: a $Ca^{2+}$-independent closed-state or a $Ca^{2+}$-dependent open-state mechanism. However, at present it is unknown whether these results, obtained in heterologous systems, are relevant to the cardiac myocyte action potential waveform or excitation-contraction coupling.

In this study, we completed meaningful modifications to the Greenstein model (65) of canine midmyocardial myocyte excitation-contraction coupling for epicardial and endocardial cells. We accomplished this by utilizing recent experimental data describing the molecular basis of transmural cellular heterogeneity and existing Markov models of $I_{NaL}$ and $I_{Kv43}$. We first demonstrate the ability of the models to simulate quantitative features of regionally varying ion channel function or expression levels. Next, we explore the consequences of a possible $Ca^{2+}$-dependent inactivation of $I_{Kv43}$ on the canine LV action potential waveforms. Finally, we investigate the contributions of sustained components of $I_{NaL}$ and $I_{Kv43}$ to early repolarization and transmural heterogeneities of APD in canine LV myocytes. We also explore how an increase in $I_{NaL,}$ e.g. due to the I1768V *SCN5A* mutation, may contribute to regional increases in APD and arrhythmic risk, examine potential additional heterogeneities and suggest targets for further experimental investigation. These models are biophysically detailed, yet computationally tractable, allowing for upward integration into tissue- and organ-scale models.

## 4.2 Methods

The Greenstein model of ECC in a canine midmyocardial myocyte (65) was used as a basis for the three canine ventricular myocyte models in this study. Briefly, the original model consists of 76 ODEs, of which 40 represent intracellular $Ca^{2+}$ cycling states. The other 36 ODEs represent gating kinetics and ion transfer relationships of the known ion channels and corresponding $Na^+$, $Ca^{2+}$, $K^+$ and $Cl^-$ currents. We added an extra state variable representing open-state inactivation of $I_{Kv43}$ (148) and replaced the existing Hodgkin-Huxley equations (3 state variables) with a 13-state Markov model of $I_{Na}$ (39). Thus, our modified models are comprised of 87 ODEs. The ionic currents we have included as contributors to transmurally heterogeneous action

potentials are outlined below. A summary of the original and modified parameters is provided in Table 4.1. Experimental data used for model validation was converted to a digital format and digitized using MATLAB.

### 4.2.1 The transient outward $K^+$ current, $I_{Kv43}$

This $K^+$ conductance is an important regulator of the early repolarization phase of the action potential. Furthermore, changes in $I_{Kv43}$ can modify ECC in ventricular myocytes. In order to investigate the consequences of a $Ca^{2+}$-dependent open state inactivation of $I_{Kv43}$, as proposed by Patel et al (148), we incorporated an additional state into the existing homotetrameric Markov model of Greenstein et al (67) (see Figure C.1). Specifically, the scaling factor for Kv4.3 (controlling current amplitude), the recovery from inactivation transition rate $\alpha_i$ and the closed-state inactivation transition rate $\beta_i$ were modified so that they agreed with recent experimental data (Table 1). The $Ca^{2+}$-dependent inactivation from the open state was simulated by the inclusion of an additional state variable $I_o$, and two transition rates, $\alpha_{o,i}$ and $\beta_{o,i}$. Since KChiP2 modifies only the Kv4.3 current (not Kv1.4 current), we altered only the biophysical parameters corresponding to Kv4.3. In the absence of any data to the contrary, we assumed that Kv1.4 is homogeneously expressed across the wall of the adult canine left ventricle.

Voltage clamp data from Rosati et al (174) suggests that the current density of $I_{to1}$ from the epicardium of the canine LV is 36% larger and that $I_{to1}$ from the endocardium is 80% smaller than in the midmyocardium. We used these data to estimate Kv4.3 scaling factors for epicardial and endocardial myocytes relative to the original value in the midmyocardial model (65). All three values were adjusted to closely match the voltage clamp data of Liu et al (130) (although they found no statistical significant difference between epicardial and midmyocardial $I_{Kv43}$). The KChIP2-dependent

transition rates ($\alpha_i$ , $\beta_i$ ) were altered to match data from Patel et al (148). Their data and this adjustment are based on an abundance of KChIP2 subunits on the epicardium, and virtually no KChIP2 subunits on the endocardium. The corresponding midmyocardial transition rates were estimated by interpolating between epicardial and endocardial values using the measured gradient of KChIP2 mRNA expression of Rosati et al (174). Since the kinetic measurements of $I_{Kv43}$ were performed at 22°C, all transition rates were scaled up to account for temperature dependence of this current.

The fourth EF-hand moiety of the KChIP β subunit displays the highest $Ca^{2+}$ affinity and underlies most of the $Ca^{2+}$ sensitivity. We have assumed that the $Ca^{2+}$-dependent transition rate $\alpha_{o,i}$ is linearly dependent on cytosolic $Ca^{2+}$ concentration. The formulation of the transition rate controlling recovery from open-state inactivation ($\beta_{o,i}$ ) was based on the voltage-dependent deactivation transition rate, $\beta_a$, but scaled to result in an appropriate rate of current inactivation. The relative contribution of the $K^+$ channel α subunit transcripts Kv4.3 to Kv1.4 was adjusted slightly from 77%/23% to 85%/15% to match the data of Dixon et al (52). After all transition rate modifications were made, Kv4.3 scaling factors were readjusted to yield appropriate peak currents.

### 4.2.2 The slowly inactivating or late Na+ current, $I_{NaL}$

To account for this important biophysical property of $I_{Na}$, we replaced the existing Hodgkin-Huxley formulation with the Markov model of Clancy et al (39). This version includes both a background mode, contributing predominantly to the large transient component of $I_{Na}$, and a burst mode, which is activated during the plateau phase of the AP and results in a sustained inward current of roughly 0.07% of the peak current density. The background mode also contributes to a second, albeit much smaller (0.2%), current density peak during Phase 3 repolarization or a ramped

voltage clamp protocol (39). The magnitude of the channel conductance was reduced to 4.6 mS/uF to yield a similar peak current density (~300 pA/pF) in both the Hodgkin-Huxley and Markov formulations.

Experimental evidence suggests that not all SCN5A channels exhibit this bursting behavior. Furthermore, the data of Zygmunt et al (273) indicate that $I_{NaL}$ is approximately twice as great in the midmyocardium as in the other regions. To reflect this heterogeneity, we reduced the bursting state conductance to ¼ of the background conductance in endocardial and epicardial myocytes and ½ of the background conductance in midmyocardial myocytes (Table 4.1). To model the I1768V mutation, we increased the recovery kinetics as described by Clancy et al (39), although to a lesser extent (50% increase instead of 100%). This resulted in an equivalent increase in $I_{NaL}$ in response in a ramped voltage protocol.

### 4.2.3 The slowly activating delayed rectifier current, $I_{Ks}$

Our $I_{Ks}$ current formulation is the same as that of Winslow et al (250). However, we modified the maximal conductance in the three types of canine ventricular myocyte in order to yield tail current densities that match the experimental values of Liu and Antzelevitch (109). Specifically, the statistically significant difference in midmyocardial tail currents was accounted for in our model.

### 4.2.4 Transmural variation in $Ca^{2+}$-handling proteins

To model heterogeneity of the SERCA uptake rate, we included a scaling term for both the forward and reverse rate of the existing SERCA pump model, as has been done by Iyer et al (79). SR uptake in epicardial myocytes was increased by a factor of 2.0, as suggested by the data of Laurita et al (93).

### 4.2.5 Computational methods and analysis

All simulations were implemented and executed in MATLAB using the built-in ode23t integrator with a maximum step size of 0.1 ms. Action potential duration was computed at 30% and 90% repolarization ($APD_{30}$ and $APD_{90}$). We fitted exponential functions to the inactivation and recovery curves of $I_{Kv43}$ in a manner similar to Patel et al (148). Briefly, for $\tau_{closed,inact}$ and $\tau_f$, the time constants were obtained by fitting exponentials of the form:

$$I = A_1 \exp(-t/\tau)$$

For $\tau_{rec,}$ the time constants were obtained by fitting exponentials of the form:

$$I = I_{peak}(1-\exp[-t/\tau_{rec}])$$

## 4.3 Results

### 4.3.1 The transient outward $K^+$ current, $I_{Kv43}$

Families of simulated current tracings corresponding to $I_{Kv43}$ in epicardial, midmyocardial and endocardial myocytes are shown in Figure 4.1A. The voltage clamp protocol is illustrated in the inset. The peak current densities are plotted in Figure 4.1B along with experimental results of Liu et al (110) for comparison. These predicted $I_{Kv43}$ amplitudes for each canine ventricular myocyte subtype are also consistent with published current densities in a number of previous papers (130, 174, 269). Note that Liu et al (110) did not detect significant differences between epicardial and midmyocardial myocytes. We chose to use the more complete data of Rosati et al

(174) as a basis for the $I_{Kv43}$ scaling parameters. Hence, our model predicts a slightly larger difference in peak $I_{Kv43}$ between epicardial and midmyocardial cells, although this is still within the range of experimental variation.

The simulations in Figure 4.2 demonstrate the ability of our model to account for differences in the gating kinetics of Kv4.3 which have been reported in the presence and absence of KChIP2 accessory subunits. Since the experimental results for different KChIP2 isoforms (KChIP2b and KChIP2d) were in general very similar, these data have been averaged. In our simulations, closed stated inactivation kinetics, (Figure 4.2A), were measured using a P2 pulse to +50 mV preceded by a P1 pulse of progressively increasing duration applied at a number of selected membrane potentials (see inset for protocol). The time course of this family of peak currents was well approximated by a single exponential with associated time constant, $\tau_{closed,inact}$. Note that the model predictions closely match the experimentally measured voltage dependence of closed state inactivation. The effect of KChIP2 on steady state inactivation is also reproduced very well. The experimentally measured mean value of $\tau_{closed,inact}$ at -60 mV for Kv4.3 with KChIP2 diverges from the exponential function that depicts the voltage dependence of closed-state inactivation kinetics at more depolarized potentials. Although the model fails to account for this deviation, it is unlikely to play a significant role in simulations of action potential waveform which are the main focus of this investigation.

The voltage-dependence of Kv4.3 recovery kinetics was evaluated over the range -100 mV to -60 mV (Figure 4.2B). A conventional double-pulse protocol (inset) was used in which interpulse intervals were varied at four selected holding potentials. Faster recovery kinetics for epicardial as compared to endocardial cells were obtains at all holding potentials. Both plots are in agreement with experimental results. Midmyocardial myocyte transition rates for $\alpha_i$, $\beta_i$, $\alpha_{o,i}$ and $\beta_{o,i}$ (not shown) were

interpolated based on reported KChIP2 expression levels. Once again, all model predictions are within the bounds of reported experimental variation.

Macroscopic inactivation kinetics were examined over the voltage range from minimal to nearly maximal current activation (–30 to +50 mV). In order to test the ability of our models to yield inactivation rates, we fitted the time course of activated current decay to a single exponential function with associated time constant $\tau_f$ and compared this with the experimentally measured values of Patel et al (148) (Figure 4.2C).

We then explored the consequences of a proposed $Ca^{2+}$-dependent inactivation of $I_{Kv43}$ on the canine LV action potential waveforms. Our simulations predict that $Ca^{2+}$-independent inactivation of $I_{Kv43}$ *alone* results in early repolarization (both in terms of the spike and dome morphology and $APD_{30}$) exhibiting a pronounced unphysiological delay in epicardial and midmyocardial myocyte models (Figure 4.3). This is not consistent with experimental data. In contrast, simulations in which inactivation proceeded via *both* $Ca^{2+}$-dependent and -independent mechanisms resulted in more realistic AP waveforms. These results suggest that KChIPs may modify $I_{Kv43}$ in both a $Ca^{2+}$-dependent and -independent fashion.

### 4.3.2 The slowly inactivating late $Na^+$ current, $I_{NaL}$

Figure 4.4A consists of computed records of $I_{NaL}$ activated in response to a series of depolarizing steps (duration 700 ms) from -140 mV (to relieve inactivation) to voltages ranging from -60 mV to 0 mV. The resulting current-voltage relationship (Figure 4.4B) closely matches the experimental measurements of Valdivia et al (233) over much of the examined range of membrane potentials.

### 4.3.3 The slowly activating delayed rectifier current, $I_{Ks}$

Our models predict a heterogeneous distribution of $I_{Ks}$ tail currents (Figure 4.5A) resulting from repolarization to -20 mV following a 5-s depolarizing stimulus (inset; magnified view of the tail currents). The predicted current-voltage relationship (Figure 4.5B) appears to reproduce the corresponding experimental findings by Liu et al (109) (inset) accurately.

### 4.3.4 The $Ca^{2+}$-activated chloride current, $I_{Cl(Ca)}$

Our models of epicardial and midmyocardial myocytes include a small contribution of $I_{Cl(Ca)}$ to total transient outward current (Figure 4.6). Note that the net effect of this was appropriate action potential morphology and duration for these two myocyte subtypes. However, the lack of any significant outward current generated an abnormal Phase 2 'hump' which delayed repolarization and prolonged $APD_{90}$ in endocardial cells. Selectively increasing $I_{Cl(Ca)}$ in endocardial cells prevented this and resulted in an $APD_{90}$ typical of these myocytes at this pacing rate (see Discussion).

### 4.3.5 $Ca^{2+}$ homeostasis and AP morphology in normal canine ventricular myocytes

A major requirement of mathematical models of cardiac myocyte electrophysiology and ECC is the ability to accurately simulate qualitative and quantitative changes in the AP and $Ca^{2+}$ transient, as a function of pacing frequency and LV location. In Figure 4.7, we demonstrate the ability of our model to predict $Ca^{2+}$ cycling kinetics which are consistent with the experimental results of Cordeiro et al (46). Specifically, elevated SR $Ca^{2+}$ content and faster $Ca^{2+}$ transient decay rates are observed in myocytes from the LV epicardium.

Figure 4.8 shows the resulting APs at cycle lengths of 500, 1000 and 2000 ms in the three canine ventricular myocytes subtypes. Table 4.2 compares the predicted $APD_{90}$ with the minimum and maximum measured values of Liu and Antzelevitch (109). In all cases the model predictions are within one standard deviation of the experimentally reported means.

We also explored the extent to which early repolarization currents play a role in determining the differences in APD between epicardial, midmyocardial and endocardial myocytes at varying pacing rates. $APD_{30}$ was measured and compared with $APD_{90}$. In all cases, the most significant difference was observed at $APD_{30}$. The difference times ($APD_{90}$-$APD_{30}$) showed very little dependence on pacing rate and myocyte subtype.

Our models can be used to investigate the relative contribution of each known heterogeneity to prolongation of the midmyocardial action potential (Table 4.3). We systematically switched midmyocardial parameters relating to each heterogeneous current to epicardial parameters. Specifically, the perturbations were: $G_{NaL}$ = 1.15 mS/uF, $G_{Ks}$ = 0.02 mS/uF, $k_{SR}$ = 2.0, and all epicardial $I_{Kv43}$ parameters. Using the model, we found that modifying $I_{NaL}$ and $I_{Kv43}$ parameters resulted in the most significant rate-dependent impact on $APD_{30}$. Substituting midmyocardial for epicardial $I_{Kv43}$ parameters (i) decreased $I_{Kv43}$ conductance, and (ii) altered the KChIP-dependent effects on $I_{Kv43}$ inactivation. The KChIP modulation of $I_{Kv43}$ played the major role in shortening $APD_{30}$ (a mere decrease in $I_{Kv43}$ conductance without KChIP modulation made little difference to APD measurements). $I_{Ks}$ did not appear to contribute significantly to midmyocardial rate-dependent APD prolongation under physiological conditions. No perturbations resulted in large changes to the difference between $APD_{90}$ and $APD_{30}$, suggesting that early repolarization currents dominate transmural heterogeneities in action potential morphology.

### 4.3.6 Proarrhythmia due to the I1768V *SCN5A* mutation

An enhancement of $I_{NaL}$, as in the case of the I1768V mutation (166), did not appear to alter early repolarization in any of the three myocyte subtypes. However we observed EADs in both midmyocardial and endocardial myocytes which occurred at all examined stimulation cycle lengths (Figure 4.9). This pattern of results may suggest that the sustained component of $I_{Kv43}$ can not only produce rapid early repolarization in epicardial myocytes, but may also protect against the late increase in $I_{Na}$ and subsequent EAD formation.

## 4.4 Discussion

Current and voltage clamp studies of isolated canine ventricular myocytes have provided a wealth of quantitative data concerning the electrophysiological properties of the $Na^+$, $Ca^{2+}$, and $K^+$ and $Cl^-$ currents that underlie the action potential and contribute to action potential heterogeneity. Information regarding the way in which individual subunits of ion channels can contribute to the electrical functioning of the ion channels has also been obtained. Evidence is emerging that in many instances, ion channels are components of macromolecular complexes, containing both pore forming ($\alpha$) and accessory ($\beta$ or $\delta$) subunits, and their function may be modified by a variety of regulatory proteins (136).

### 4.4.1 The transient outward $K^+$ current, $I_{Kv43}$

It has been suggested by many investigators that KChIPs can regulate the transmural heterogeneity of $I_{Kv43}$ in canine ventricular myocytes (145)**.** In addition to altering expression levels and accelerating recovery from inactivation, KChIP2 isoforms can modify Kv4.3 gating kinetics by 1) a $Ca^{2+}$-independent slowing of closed-state inactivation and 2) a $[Ca^{2+}]_i$-dependent open state inactivation. This

current was previously thought to be insensitive to $[Ca^{2+}]_i$, and previous models do not account for this.

The experimental data and proposed model of Patel et al (148) predict that channels that inactivate by the open-state mechanism must reopen upon hyperpolarisation before reentering the closed-state (see Figure C.1). Such reopening events can generate an outward current. This current has been measured experimentally (49, 148, 178) and is maximal under conditions of elevated $[Ca^{2+}]_i$. In the model we have developed, $I_{Kv43}$ is most prominent in Phase 1, but can also contribute to early repolarization since it fails to inactivate completely and can neutralize the sustained component of $I_{Na}$. This slow inactivation occurs as a consequence of KChIP2- and $[Ca^{2+}]_i$-dependent modifications to $I_{Kv43}$ gating kinetics. This effect may become important in conditions such as congestive heart failure, when $I_{Kv43}$ is significantly downregulated and $APD_{90}$ is prolonged.

The hydrophobic interactions of KChIPs and Kv4 channels bear a striking resemblance to the modes of interaction between calmodulin and its target proteins (268). KChIPs and calmodulin moieties share the structural feature of a 4 EF-hand scaffold that undergoes $Ca^{2+}$-mediated conformational changes. Furthermore, elution profiles from size-exclusion chromatography have indicated that chelating $Ca^{2+}$ destabilizes the KChIP2-Kv4 interactions (268), consistent with similar results on calmodulin ion channel interaction. These and other studies suggest a common mechanism of $Ca^{2+}$ regulation among ion channel proteins.

### 4.4.2 The slowly inactivating or late $Na^+$ current, $I_{NaL}$

In heart, the SCN5A-encoded Nav1.5 is the predominant carrier of $I_{Na}$. Accessory subunits also modulate $I_{Na}$ current density and voltage-dependent gating (136). Recent evidence suggests that $Na^+$ channels contribute not only to the action potential

upstroke, but also to the plateau phase and repolarization. Sustained activity can result from channels which fail to inactivate, or channels which recover from inactivation during repolarization. A recent report by Maltsev et al delineates the behavior into three separate mechanisms: channel bursting, window current and recovery from inactivation (117). Here we demonstrate that the sustained component of $I_{Na}$ can be an important regulator of early repolarization and underlies to a large extent the increase in the measured APDs and rate-dependency of midmyocardial myocytes.

The I1768V mutation-induced increase in $I_{NaL}$ is a potent instigator of $Ca^{2+}$-mediated EADs originating during Phase 3 repolarization in our model. Specifically, this mutant has been demonstrated to result in long QT-syndrome type-3 (LQT3). Previous modeling studies of this mutation have suggested that the alteration in gating kinetics accounts for AP prolongation and susceptibility to $Ca^{2+}$-mediated EADs (39). Our simulations demonstrate that these phenotypes are most pronounced in midmyocardial and endocardial myocytes. These effects are also more marked in our canine models than previous modeling studies (in guinea-pig) have suggested.

### 4.4.3 The slowly activating delayed rectifier current, $I_{Ks}$

Some previous models of the ionic currents which underlie the mammalian ventricular action potentials have tended to overestimate the magnitude of $I_{Ks.}$ This may have been a practical adjustment made in order to exceed inward currents and hence generate the appropriate $APD_{90}$. It may also have contributed to the role of $I_{Ks}$ in action potential heterogeneity being overstated. Increasing the conductance of $I_{Ks}$ in the midmyocardium to be equal to that in the other two regions decreased $APD_{90}$ only slightly. Our results suggest that, under normal physiologic conditions, other currents such as $I_{NaL}$ and $I_{Kv43}$ may have a greater influence on transmural heterogeneities of APD.

### 4.4.4 The $Ca^{2+}$-activated chloride current, $I_{Cl(Ca)}$

The extent to which anionic currents contribute to transmural electrical heterogeneity has been investigated less thoroughly than their cationic counterparts (78). No difference in $I_{Cl(Ca)}$ current density was measured in canine epicardial and midmyocardial myocytes (272), but endocardial myocytes were not included in this study. We could find no subsequent or prior report in the literature of an investigation into transmural heterogeneity of $I_{Cl(Ca)}$ in canines that included endocardial cells. Hence our decision to assign a heterogeneous transmural conductance of this current is not based on quantitative experimental results. Its inclusion in the model can be justified by the both the absence of conflicting data, and clear evidence that without it, endocardial cells display unphysiologic features of AP morphology.

### 4.4.5 Heterogeneities in $Ca^{2+}$ fluxes and homeostasis

In canine LV myocytes, time to peak and the duration of the $Ca^{2+}$ transient have been reported to be longer in endocardial cells (46). In addition, SR $Ca^{2+}$ content, as measured by rapid application of caffeine, is largest in epicardial cells (46). A variety of experimental findings suggest that a combination of electrical heterogeneity and intrinsic differences in ECC may underlie these differences in the SR $Ca^{2+}$ concentration and kinetics of the $Ca^{2+}$ transients. Greater SERCA expression on the epicardium may contribute to a higher SR $Ca^{2+}$ content and faster decay (93), while the spike and dome morphology of the epicardial AP waveform permits a greater L-type $Ca^{2+}$ current (LCC) current (65). It is presumed that these differences result in a more coordinated contraction of the ventricular myocardium i.e. the faster kinetics of epicardial myocyte $Ca^{2+}$ transients compensate for the delay in activation.

It is known that intracellular $Ca^{2+}$ handling can have significant effects on cellular electrical behavior. Hence it is very important to include mechanistic detail of

intracellular $Ca^{2+}$ dynamics in studies of the action potential waveform. Many previous ionic models of ventricular myocyte excitation-contraction coupling have dealt with intracellular $Ca^{2+}$ cycling in only a qualitative manner. These approaches therefore lack a mechanistic representation of local CICR control. For instance, common pool models, as their name suggests, direct $Ca^{2+}$ influx and SR release into a single cytosolic domain, which simultaneously controls RyR current (80, 141, 143, 250). A consequence of this is that once the RyR current is triggered, the resulting increase in "subspace" $Ca^{2+}$ ensures an all-or-none SR release. As such, these models fail to reproduce one of the most important features of $Ca^{2+}$ handling in cardiac myocytes, that of the graded $Ca^{2+}$ release, in which SR $Ca^{2+}$ release is proportional to LCC influx (211). A further limitation of many previous models is their very strong reliance on voltage-dependent inactivation of $I_{CaL}$ for stability (211). This conflicts with experimental evidence which consistently points to $Ca^{2+}$ dependent inactivation as the dominant mechanism (107). Other model formulations that base SR $Ca^{2+}$ release on LCC influx do so in a phenomenological manner and have less predictive capability (56, 114, 155). In contrast, local control models (66, 164, 201, 207) have successfully reproduced experimental observations. However in general, these are too computationally intensive for upward integration into tissue or whole organ models. Our model effectively addresses these limitations.

### 4.4.6 Limitations

Our model, in its present form, has several limitations. The existence of apparent discrepancies between the measured $I_{NaCa}$ data of Zygmunt et al(274), that of Xiong et al (255) and the existing model formulation of $I_{NaCa}$ prevented the inclusion of transmural heterogeneity of this current in this study. The disparities may have arisen from differences in experimental protocols and/or the difficulties associated with

isolating this current using the required pharmacological approaches. In order to reconcile the differences in predicted $I_{NaCa}$ heterogeneities, further experimental investigation is required. Thereafter, a thorough analysis of this antiporter mechanism can be carried out.

Our model recapitulates many of the observed differences between Kv4.3 currents expressed alone and with KChiPs in heterologous systems. However, it fails to predict $\tau_{closed,inact}$ at membrane potentials more negative than -50 mV. Furthermore, despite the evidence favoring two distinct mechanisms of inactivation, the current records were in most cases well characterized with a single exponential with kinetics corresponding to the fast component ($\tau_f$) of the results of Patel et al (148). There may be several reasons for these discrepancies. Firstly, it is difficult to predict intracellular $Ca^{2+}$ concentrations (which are thought to regulate the slow component of inactivation) within the heterologous system. Secondly, as in the case of $I_{Na}$, multiple open states may underlie the different components of inactivation rate. Finally, many other mechanisms of Kv4 channel regulation have been demonstrated (see below).

Kuo et al have demonstrated the importance of KChIPs in the regulation of Kv4 channels by analyzing currents in right ventricular myocytes isolated from $KChIP^{-/-}$ mice (90). Their studies reveal a complete loss of $I_{to1}$ in the RV of $KChIP^{-/-}$ mice. The majority of experimental reports confirm the importance of KChIPs in the regulation of $I_{Kv43}$. However, Deschenes et al failed to detect a transmural gradient of KChIP across the canine LV wall (50). It has been suggested that non-specific binding of the polyclonal antibody used in this study may have masked the KChIP expression profile (145).

Many other mechanisms of Kv4 channel regulation have been demonstrated, and we do not account for these in our model (for a review see Patel and Campbell (145)). Briefly, these other regulatory subunits include frequenin (132), MinK-related peptide

1 (MiRP1) (265), NFAT/calcineurin (177) and DPPXs (131). All of these may contribute to $I_{Kv43}$ regulation *in vivo*. Of these, frequenin is thought to be the most likely candidate (145), possibly due to the structural similarity to KChIPs (both are neuronal $Ca^{2+}$ sensors containing multiple EF hands). Indeed, frequenin has been reported to co-immunoprecipitate with Kv4.3 $\alpha$ subunits in mouse ventricle extracts (68). However, others were unable to detect this association (163). Furthermore, it has been demonstrated that the interactions of KChIPs with Kv4 channels are substantially stronger and/or more efficient than those of frequenin (163).

We have replicated and normalized model simulations as closely as possible to experimental data acquisition conditions and protocols. However, in some papers, a narrow temperature range was given instead of an exact value. The reaction rate measurement $Q_{10}$ is approximately 3 for gating kinetics and 1.3 for ion transfer, which may introduce small errors into our predictions. Nevertheless, these errors are well within the bounds of normal experimental variation. Furthermore, the results from extrapolating kinetic data to 37°C are in close agreement with independent data.

Some of the results used in the validation process were obtained in heterologous cell culture systems. Additional modulating proteins, such as caveolins (263), present in the native environment of the cardiac myocyte sarcolemma may affect channel function. We also failed to account for any interactions between ion channels and the actin cytoskeleton and/or the extracellular matrix, which have been suggested to play a role in whole cell functioning (136).

Recent results also draw attention to a transmural gradient of the $\alpha$ subunit of the $Na^+$-$K^+$ pump, $I_{NaK}$, in which ion channel expression decreases from epicardium to endocardium (59). However, it is thought that under physiological conditions, transmural gradients of intracellular $Na^+$ result in nearly homogeneous whole cell $I_{NaK}$. The paucity of quantitative data regarding these results prohibited the inclusion of this

electrochemical gradient in our investigation. There also appears to be a gradient of $I_{Cl(cAMP)}$, increasing from endocardium to epicardium (81, 221, 252). However under normal conditions, cAMP levels are low and constant, and thus this current is unlikely to significantly contribute to cellular electrical response.

The Greenstein model is based on dynamic changes in intracellular ion concentrations and as such displays some degree of nonphysiological "drift". However, it is stable (in terms of both APD and intracellular ion concentrations to within 1.5%) over a period of greater than 50 heartbeats. This degree of stability is comparable, or better, than previous models of this type (125, 250).

Dixon et al (52) report that Kv1.4 mRNA is present at 16% of the level of Kv4.3 mRNA in the canine LV. However, there appears to be no electrophysiological evidence for a Kv1.4-mediated slowly recovering cumulatively inactivating transient outward current phenotype in canine (145). With respect to the original Greenstein model, we have attempted to make only those changes that confer the molecular bases of transmural electrophysiological heterogeneities. Therefore, we have modified the original model of Greenstein et al to reflect the data of Dixon et al by *decreasing* the contribution of the Kv1.4 current, but chose not to remove it completely.

Recent experimental investigations suggest that calmodulin binding to KCNQ1, the pore-forming subunit of the $I_{Ks}$ channel, is required for protein assembly and conferral of $Ca^{2+}$ sensitivity to the $I_{Ks}$ current (199). The role of calmodulin in the folding and assemble of KCNQ1 is likely to be accounted for indirectly in existing formulations of $I_{Ks}$. However, we do not model a $Ca^{2+}$ sensitive component of $I_{Ks}$. Although we do not account for this potentially important mechanism of functional regulation of $I_{Ks}$, we demonstrate only a minimal contribution of $I_{Ks}$ to repolarization in canine ventricular myocytes under our simulation conditions. Further investigations

into action potential regulation during elevated adrenergic tone may require these interactions to be incorporated into the model.

### 4.4.7 Suggested experiments

One of the consequences of detailed model development and testing is that it reveals where the published experimental results in single myocytes fail to fully account for physiological phenomena. Our results suggest a number of potential opportunities for further investigation including additional examination of transient outward currents in canine endocardial myocytes and the detailed nature of the transmural heterogeneity of $I_{NaCa.}$

Our model may also be a useful tool to aid in the understanding of arrhythmia mechanisms in patients with Brugada syndrome. This condition is characterized by ST segment elevation, prominent J-waves and SCD (6). Brugada syndrome appears to be linked to SCN5A mutations that result in a reduction of $Na^+$ influx across the right ventricular epicardium (102). It is hypothesized that premature repolarization in this region contributes to electrical heterogeneity of repolarization and creates an electrical substrate conducive to reentrant arrhythmias (6).

### 4.4.8 Conclusions

We have completed meaningful modifications to the Greenstein model (65) of canine midmyocardial myocyte excitation-contraction coupling for epicardial and endocardial cells. Expression levels (current densities) and gating kinetics parameters for $I_{Kv43}$, $I_{Ks}$, $I_{NaL}$ and SERCA were constrained by experimental data from a number of different laboratories, using myocytes isolated from the three transmural locations within the canine left ventricle. Our results suggest that early repolarization currents such as $I_{Kv43}$ and $I_{NaL}$ play a major role in shaping the cardiac AP. The model predicted that KChIP2- and $Ca^{2+}$-dependent control of $I_{Kv43}$ permits a sustained outward current that neutralizes $I_{NaL}$ in a rate and subtype-dependent manner. Both these currents appear to play major roles in the increased AP duration and rate-dependence in midmyocardial myocytes. Furthermore, the increased ratio of $I_{Kv43}$ to $I_{NaL}$ appears to protect epicardial myocytes since the incidence of EADs resulting from the SCN5A I1768V mutation-induced increase in $I_{NaL}$ is much reduced.

**Table 4.1:** Modifications to parameters in the Greenstein model.

| | Original | Epi | M | Endo | Heterogeneity References | Others |
|---|---|---|---|---|---|---|
| GKs (mS/uF) | 0.035 | 0.02 | 0.01 | 0.02 | Liu and Antzelevitch (1995) | |
| kNaCa (Xiong) | 0.27 | 0.27 | 0.11 | 0.11 | Xiong et al (2005) | Zygmunt et al (2000), Wan et al (2005) |
| kSR | 1.00 | 1.00 | 0.40 | 0.40 | Cordeiro et al (2004), Laurita et al (2003) | |
| GNaL (mS/uF) | 0.00 | 0.001 | 0.002 | 0.001 | Zygmunt et al (2001), Valdivia et al (2005) | |
| Kv43Frac | 0.77 | 0.85 | 0.85 | 0.85 | Dixon et al (1996) | |
| Kv4p3Scale | 1.00 | 2.00 | 1.50 | 0.22 | Rosati et al (2001), Liu et al (1993) | Zicha et al (2004), Nabauer et al (1996) |
| $k\alpha_i$ | 1.00 | 2.25 | 1.22 | 0.18 | | |
| $k\beta_i$ | 1.00 | 1.125 | 1.69 | 2.25 | Patel et al (2004) | Patel et al (2002), Nabauer et al (1996) |
| $k\alpha_{o,i}$ | 0.00 | 2000 | 1000 | 0.00 | | |
| $k\beta_{o,i}$ | 0.00 | 0.20 | 0.10 | 0.00 | | |
| Ito2scale | 1.00 | 0.50 | 0.50 | 2.50 | Verkerk et al (2004) | |

**Table 4.2:** Experimental measurements of $APD_{90}$ in epicardial, midmyocardial and endocardial myocytes and comparison with model predictions.

| | | Experiment | | Model | | |
|---|---|---|---|---|---|---|
| | **BCL(ms)** | $APD_{90}$ (Mean) | $APD_{90}$ (SD) | $APD_{90}$ | $APD_{30}$ | $APD_{90}$ - $APD_{30}$ |
| **Epicardial** | 500 | 197 | 35 | 186 | 131 | 55 |
| | 1000 | 231 | 44 | 214 | 159 | 55 |
| | 2000 | 250 | 47 | 277 | 219 | 58 |
| **Midmyocardial** | 500 | 222 | 29 | 241 | 177 | 64 |
| | 1000 | 286 | 49 | 270 | 202 | 68 |
| | 2000 | 338 | 77 | 384 | 303 | 81 |
| **Endocardial** | 500 | 212 | 28 | 209 | 139 | 70 |
| | 1000 | 250 | 33 | 233 | 162 | 71 |
| | 2000 | 270 | 40 | 290 | 216 | 74 |

**Table 4.3:** Effect of substituting midmyocardial parameters for epicardial parameters on model predictions of APD: a sensitivity analysis.

| | BCL (ms) | $APD_{90}$ | $APD_{30}$ | $APD_{90}$ - $APD_{30}$ | % change from baseline |
|---|---|---|---|---|---|
| Normal | 500 | 241 | 177 | 64 | |
| | 1000 | 270 | 202 | 68 | |
| | 2000 | 384 | 303 | 81 | |
| Epi $G_{NaL}$ | 500 | 233 | 169 | 64 | 3.32% |
| | 1000 | 254 | 190 | 64 | 5.93% |
| | 2000 | 345 | 274 | 71 | 10.16% |
| Epi $G_{Ks}$ | 500 | 238 | 174 | 64 | 1.24% |
| | 1000 | 266 | 198 | 68 | 1.48% |
| | 2000 | 365 | 287 | 78 | 4.95% |
| Epi kSR | 500 | 230 | 165 | 65 | 4.56% |
| | 1000 | 251 | 157 | 94 | 7.04% |
| | 2000 | 371 | 296 | 75 | 3.39% |
| Epi $I_{Kv43}$ | 500 | 225 | 167 | 58 | 6.64% |
| | 1000 | 246 | 185 | 61 | 8.89% |
| | 2000 | 329 | 264 | 65 | 14.32% |

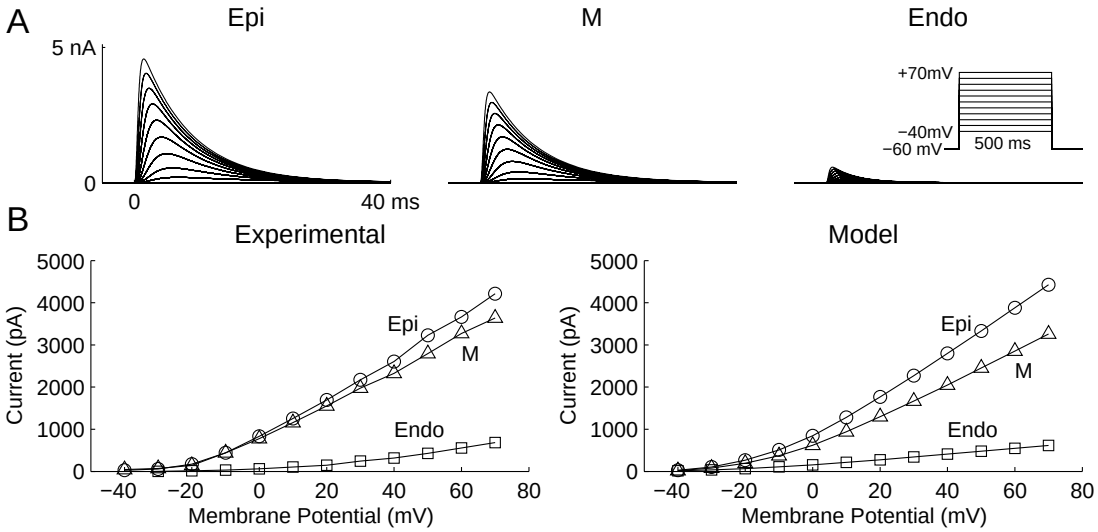


**Figure 4.1** Heterogeneity of $I_{to1}$ in epicardial, midmyocardial and endocardial canine LV myocytes. (A) Predicted $I_{to1}$ current tracings in all three ventricular myocytes subtypes at 37°C (including voltage clamp protocol). The tracings were recorded during depolarizing steps (300 ms duration) from a holding potential of -80 mV to test potentials ranging from -40 mV to +70 mV. The time scale of the record is abbreviated in order to better illustrate differences in these currents. (B) Peak current measurements from the voltage clamp protocol in (A) measured by Liu et al(110) at 37°C *(left)* and predicted by the model *(right)*.

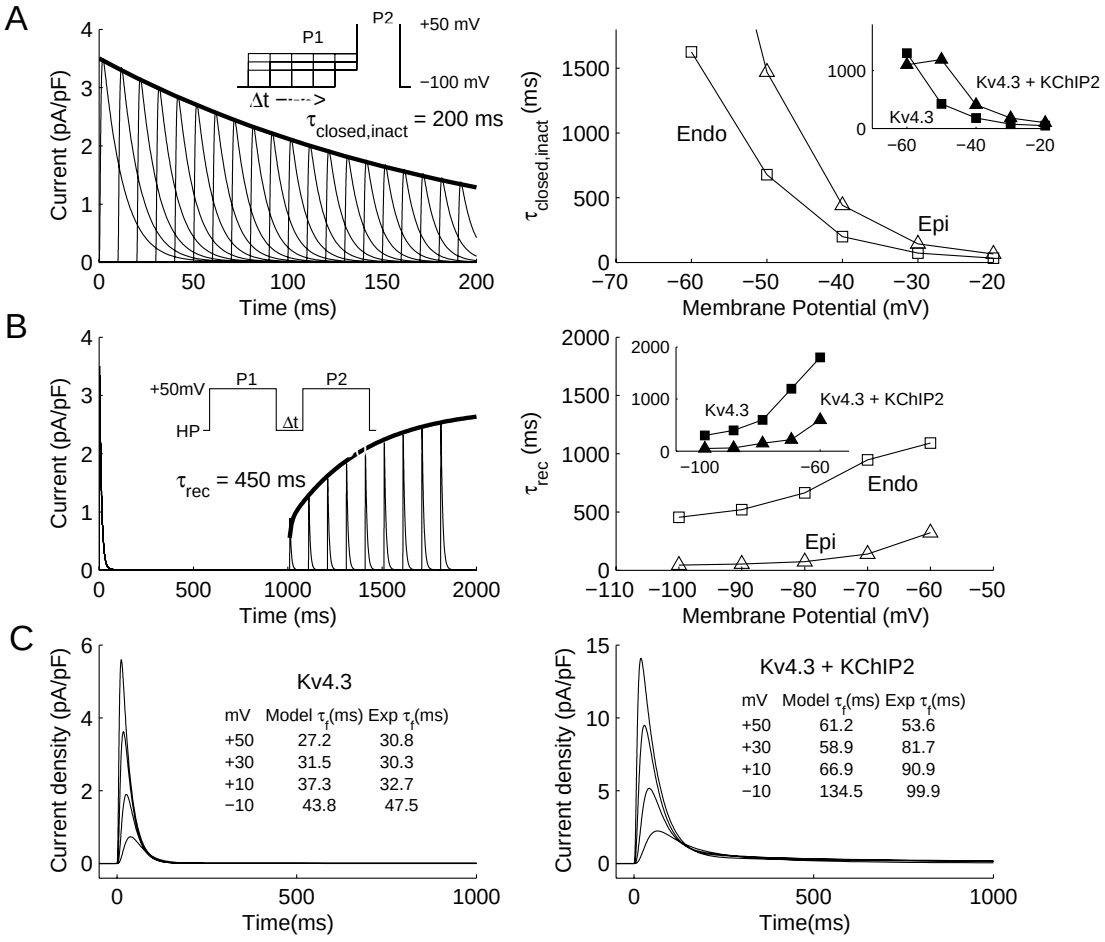


**Figure 4.2:** Heterogeneity in the KChIP2-dependent gating kinetics of $I_{to1}$ in epicardial and endocardial canine LV myocytes over a range of examined potentials. (A) Voltage-dependence of Kv4.3 closed state inactivation kinetics (-60 to -20 mV) with representative Kv4.3 closed state inactivation protocol current waveforms for P1 = -40 mV *(left)*. Peak P2 currents were fitted with a single exponential relationship with indicated $\tau_{closed,inact}$. Inset, voltage clamp protocol. *(Right)*, overlay of the predicted time constants of closed state inactivation. Inset, experimental data of Patel et al(148), with averaged results for different KChIP2 isoforms. (B) Voltage-dependence of Kv4.3 recovery kinetics (-100 mV to -60 mV) with representative Kv4.3 recovery waveforms at a holding potential (HP) = -100mV fitted with indicated $\tau_{rec}$ (left). Inset, recovery protocol. *(Right)*, overlay of predicted values of $\tau_{rec}$ for Kv4.3 and Kv4.3+KChIP2 isoforms. Inset, experimental data of Patel et al (148).

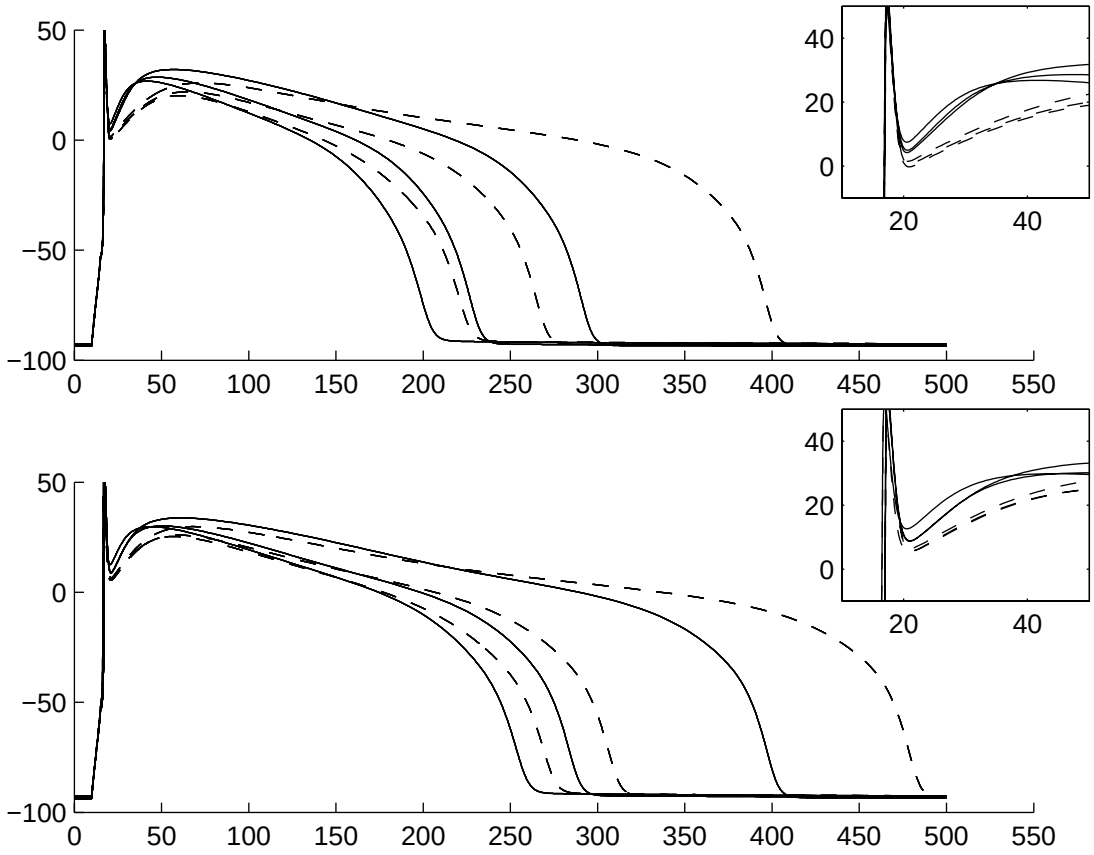


**Figure 4.3:** Consequences of $Ca^{2+}$-independent only (dashed) vs both $Ca^{2+}$-dependent and –independent (solid) mechanisms of $I_{Kv43}$ inactivation in epicardial (*upper*) and midmyocardial (*lower*) myocyte models.

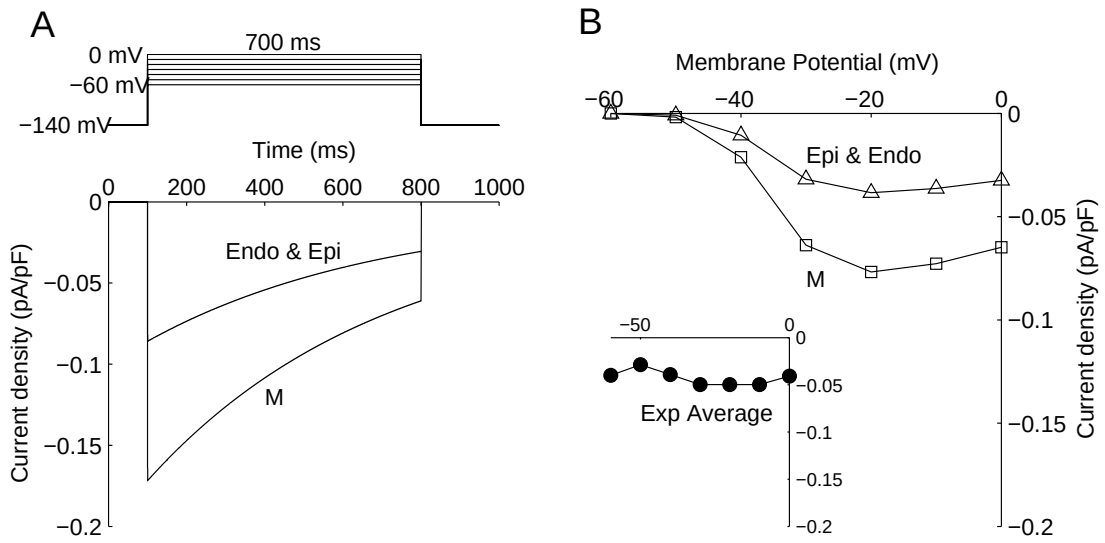


**Figure 4.4:** Heterogeneity of $I_{NaL}$. (A) Voltage clamp protocol and resulting currents at -20 mV at 25°C. (B) Model predictions of current-voltage relationship at 25°C with inset experimental results of Valdivia et al (room temperature) (233).

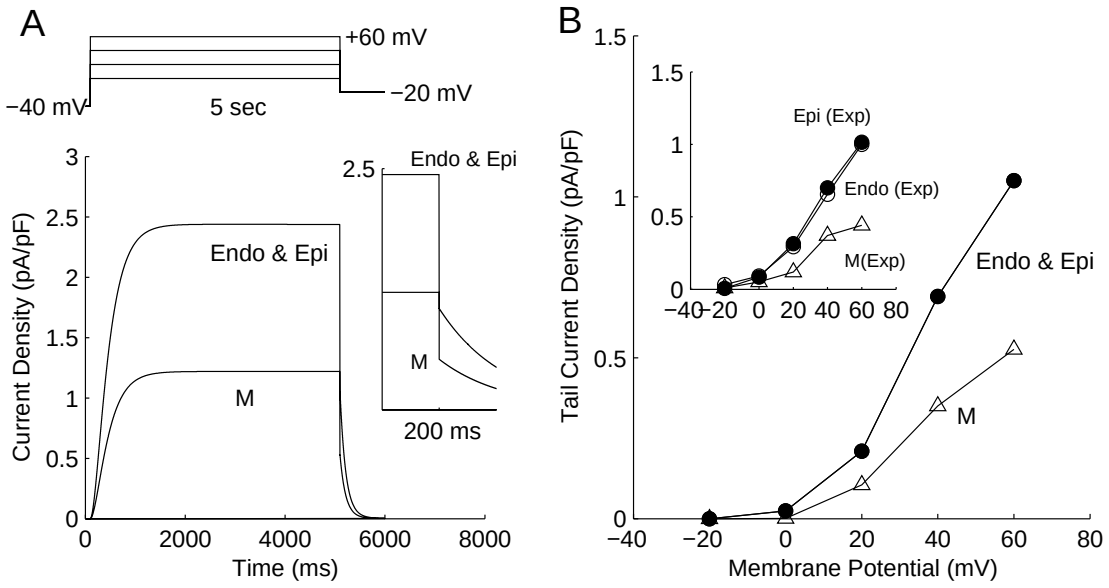


**Figure 4.5:** Heterogeneity of $I_{Ks}$ tail currents. (A) Model tracings of $I_{Ks}$ depolarization and tail currents and voltage clamp protocol at 37°C. (B) Voltage dependence of model (37°C) versus experimental tail currents (inset;Liu and Antzelevitch, 35-37°C (109)).

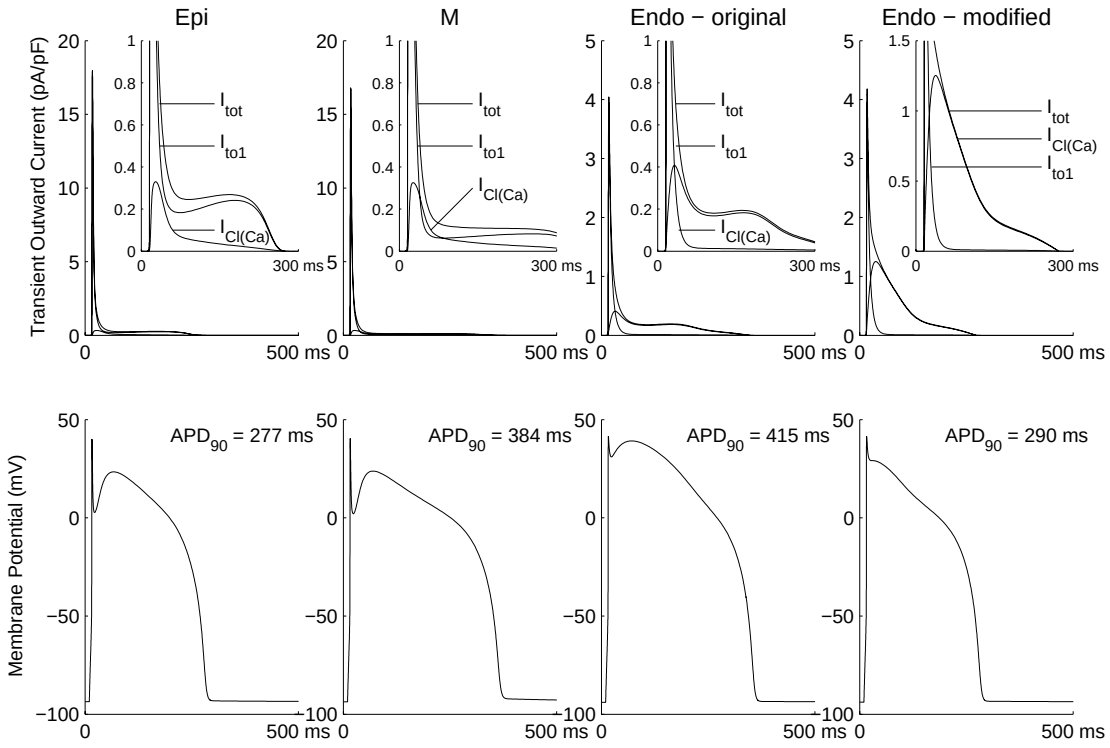


**Figure 4.6:** Contributions of $I_{to1}$ and $I_{Cl(Ca)}$ to total ($I_{tot}$) transient outward currents (upper) in the three myocyte subtypes at a cycle length of 2000ms with corresponding action potentials (lower). A modified endocardial cell model is included to demonstrate how upregulation of $I_{Cl(Ca)}$ increases endocardial transient outward current preventing unphysiologic features of action potential morphology and duration.

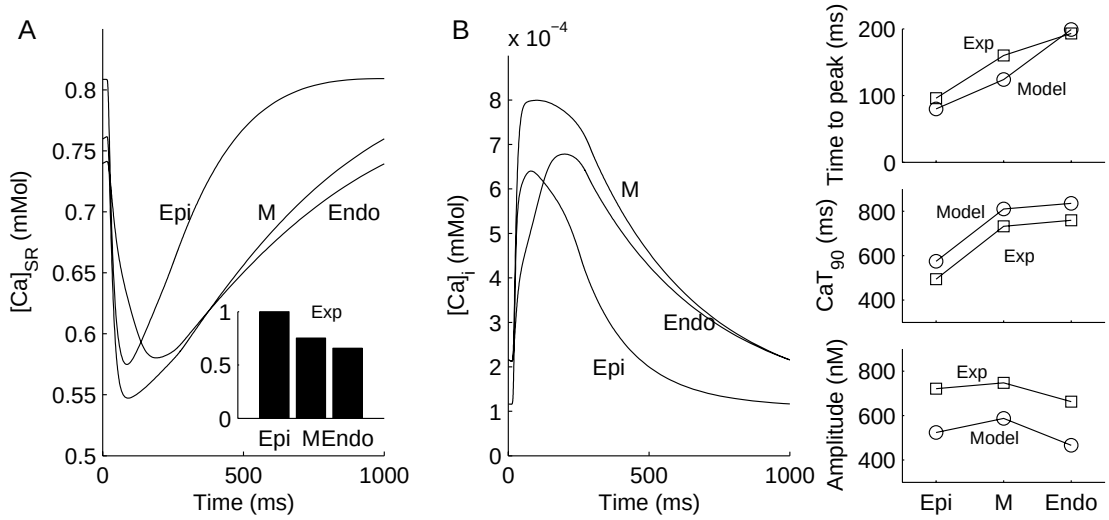


**Figure 4.7:** Heterogeneity of (A) SR $Ca^{2+}$ concentration (inset; Cordeiro et al (46)) and (B) $Ca^{2+}$ transients at 1 Hz with plotted comparisons between model predictions and measured experimental data of Cordeiro et al (46).

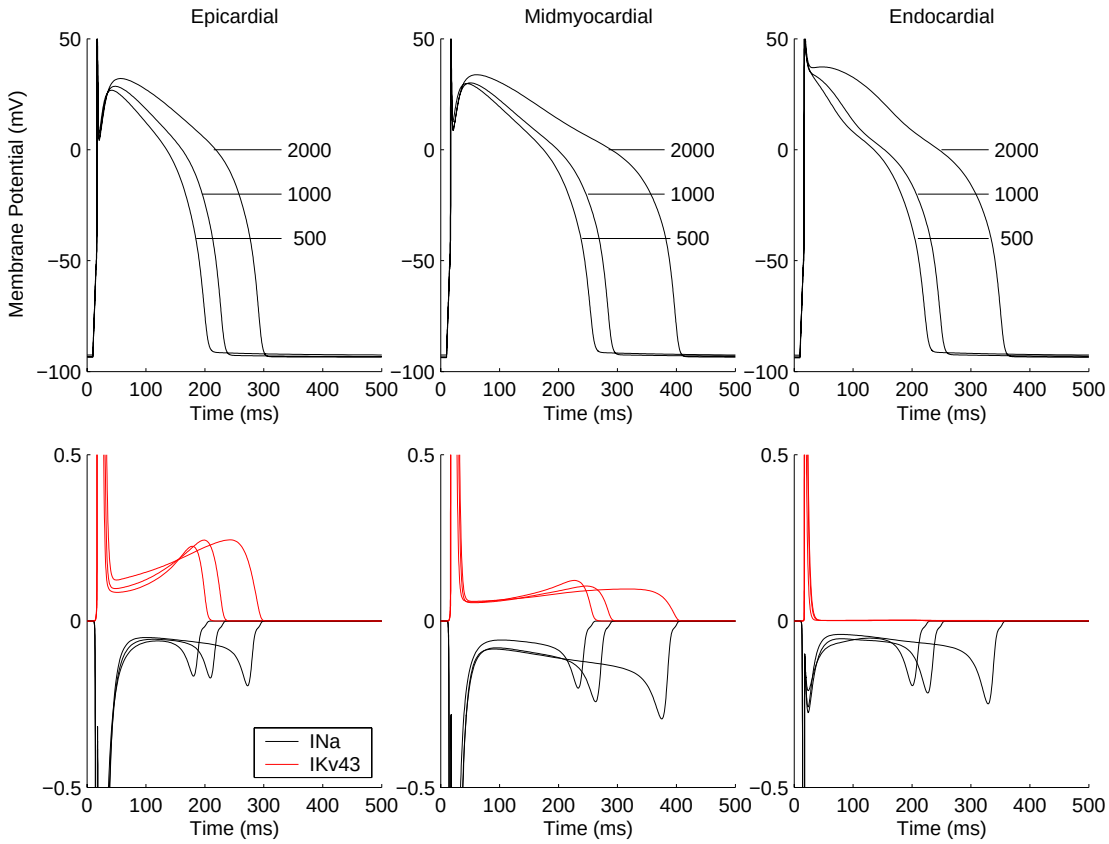


**Figure 4.8:** *(Upper)* Model-computed action potential morphology, duration and rate dependence of epicardial, midmyocardial and endocardial action potentials with parameters as outlined in the Appendix. *(Lower)* Model-computed $I_{Na}$ (black) and $I_{Kv43}$ (red). Cycle lengths are in ms.

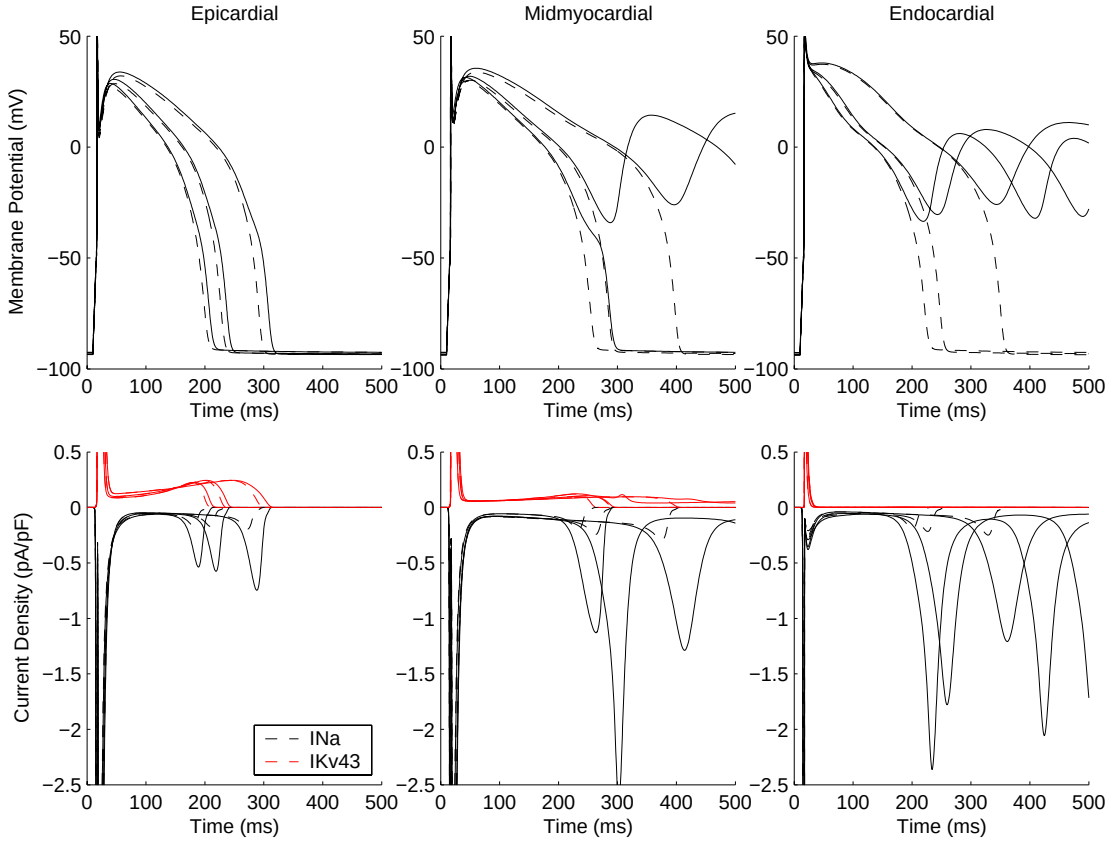


**Figure 4.9:** *(Upper)* Model-computed action potential morphology, duration and rate dependence of epicardial, midmyocardial and endocardial action potentials with altered $I_{Na}$ parameters representative of the I1768V SCN5A mutation. Original AP tracings are shown in dotted lines for direct comparison. *(Lower)* Model-computed $I_{Na}$ (black) and $I_{Kv43}$ (red) for mutation with original currents shown in dotted lines for comparison. Cycle lengths are in ms.

The text of Chapter 4, entitled “Contributions of sustained $I_{NaL}$ and $I_{Kv43}$ to heterogeneity of early repolarization and arrhythmogenesis in canine left ventricular myocytes” by Sarah Flaim, Wayne Giles and Andrew McCulloch is a reprint of the material as it was submitted to the American Journal of Physiology (Heart and Circulation).

# CHAPTER 5

# Computational modeling of arrhythmia formation in an LQT3 *SCN5A* mutation: From genetic mutation to clinical phenotype

## 5.1 Introduction

Mutations in the genes encoding for ion channel proteins can alter the delicate balance of ionic fluxes underlying the cardiac action potential. Patients with so-called "ion channelopathies" are susceptible to a particular polymorphic ventricular tachycardia known as torsades de pointes (TdP) and sudden cardiac death (168). The most common of these conditions is the long QT syndrome (LQTS). In addition to QT prolongation, T wave morphology is often abnormal, consistent with the concept of ventricular repolarization abnormalities playing a role in creating an unstable electrical substrate predisposed to arrhythmia formation (102). It is increasingly recognized that even under normal conditions, measurements of action potential duration and morphology within the left ventricle are highly heterogeneous (9). The contribution of these cellular heterogeneities to the transition from normal rhythm to TdP is unclear.

Recognition of regional variation in the expression and function of ion channels across the wall of the left ventricle promoted the notion of transmural dispersion of repolarization (TDR). The intrinsically long APDs, reduced repolarization reserve and strong rate dependence of isolated midmyocardial cells (M-cells) has implicated them in determining the polarity and width of the electrocardiographic T-wave in normal hearts (9, 13), and reentrant arrhythmia formation in pharmacologically altered hearts (representative of ion channelophathies e.g. LQTS) (61, 202, 239). However, there

exists considerable debate as to the extent that midmyocardial cells play a role in intact myocardium given the potential for intrinsic electrical differences to be masked by electrotonic effects. Experimental studies that have addressed this issue have varying results with evidence both for and against M-cell dominated electrical gradients (for review see Taggart et al (219)), leading to the question of whether M-cell-mediated increases in TDR occur *in vivo* or not. Previous modeling work has suggested that M-cells are not required for an upright T-Wave (40) and geometric factors such as wall thickness may alter the extent that intrinsic heterogeneities influence repolarization patterns (182). Furthermore, the intrinsic electrical properties of individual cells can be modified by their location with respect to the beginning and end of propagation and collision of wavefronts (251). However, midmyocardial APDs, as measured by recording electrodes or optical mapping of canine ventricular wedge preparations, consistently exceed those from other regions in a rate-dependent manner.

Another factor more recently implicated as a strong influence on both normal cardiac electrophysiology and arrhythmia formation is intracellular calcium ($Ca^{2+}$) cycling (27). Briefly, recent experimental data has demonstrated inactivation of the sarcolemmal L-Type $Ca^{2+}$ channel (LCC) to be primarily $Ca^{2+}$-dependent (107). Fluctuations in intracellular $Ca^{2+}$ levels can modulate the shape and duration of the cardiac action potential via altering transmembrane $Ca^{2+}$ fluxes. In the myoplasm, $Ca^{2+}$ binds to regulatory molecules, such as calmodulin, and thereby can modify ion channel function on a beat-to-beat basis or over longer time periods (149). In extreme instances, highly proarrhythmic $Ca^{2+}$-mediated afterdepolarizations, both early and delayed, may be observed. Here again, conditions *in vivo* are complicated by a heterogeneous distribution of $Ca^{2+}$-handling proteins, including the sarcolemmal sodium-calcium exchanger (NCX) (255) and the sarcoplasmic reticulum $Ca^{2+}$-ATPase (SERCA) pump(93).

The difficulties in obtaining high resolution three dimensional (3D) measurements of myocardial electrical activity and $Ca^{2+}$ cycling *in vivo* limit experimental investigation into the role of intrinsic heterogeneities on the pattern of normal and abnormal repolarization patterns. Furthermore, experimental measurements may be influenced by use of anesthetics and other methodological concerns (14, 219). Thus, we investigated these phenomena using a computational model of the canine left ventricular wedge preparation with a realistic model of whole cell ionic currents including mechanistic descriptions of intracellular $Ca^{2+}$-cycling. The modeling framework allows us to assess the contributions of the regional variations in ion channel and $Ca^{2+}$-handling proteins on normal electrical propagation as well as to investigate how defects in ion channel function may lead to arrhythmia formation. Specifically, we investigated the proarrhythmic consequences of the I1768V *SCN5A* mutation resulting in variant 3 of the long QT syndrome (LQT3). Our simulations predict EADs localized to the endocardium that trigger midmyocardial and epicardial action potentials leading to an "R on T" extrasystole on the ECG.

## 5.2 Methods

### 5.2.1 Whole cell models of canine ventricular myocyte ECC

The whole cell models of canine epicardial, midmyocardial and endocardial ventricular myocyte ECC were previously developed and validated against a wide range of experimental data. Briefly, we included transmural heterogeneities for the voltage-dependent transient outward current $I_{Kv43}$; the slowly activating delayed rectifier current, $I_{Ks}$; the late sodium ($Na^+$) current, $I_{NaL}$; and the SR $Ca^{2+}$-ATPase pump (SERCA).

The model of the I1768V *SCN5A* mutation was developed by Clancy et al (39). In our implementation, we increased the recovery kinetics as described by Clancy et al (39), although to a lesser extent (50% increase instead of 100%). This resulted in an equivalent increase in $I_{NaL}$ in response in a ramped voltage protocol.

### 5.2.2 3D integrative model of a canine LV tissue wedge

To model transmural heterogeneity at the tissue level, we extracted a two-element wedge from the posterior LV free wall (average dimensions 1.0 cm (transmural), 0.8 cm (circumferential) and 1.4 cm (longitudinal)) from the original 24 element anatomic model of the canine ventricular geometry and fiber architecture described by LeGrice et al (96). The dimensions of the model wedge are within those from the corresponding experimental preparations (111, 261). The wedge was repetitively refined in each direction to yield a 2048 element mesh with 21,384 degrees of freedom. This was sufficient to obtain solutions for conduction velocity and APD at 90% repolarization ($APD_{90}$) to within 1% (see Appendix D). Transmural heterogeneity was incorporated using the epicardial, midmyocardial and endocardial parameters defined earlier in layers of equal thickness (unless otherwise indicated). Initial conditions for the finite element simulations were generated from the single cell models. All initial conditions were at steady state for the relevant pacing rates and myocyte subtype. Transversely orthotropic conductivities were selected to obtain activation times consistent with experimental observations (Figure 5.2). No-flux boundary conditions were prescribed along the edges of the tissue. A pseudo-ECG was estimated by calculating the potential at an electrode 20 mm from the layer corresponding to the epicardial surface using the approach of Gima and Rudy (2002). The conductivity was reduced to 50% of that in other regions in the outermost 10% of the wedge to account for an experimentally measured increase in tissue resistivity here

(261). The diffusion coefficient was increased 10-fold in the innermost endocardial layer, representative of the Purkinje fiber network. Unless otherwise indicated, TDR is defined as the difference between the maximum and minimum repolarization times recorded at 90% repolarization.

## 5.3 Results

### 5.3.1 M-cells contribute to early dispersion of repolarization

In the first instance we measured activation and recovery times in the heterogeneous canine LV wedge model for basic cycle lengths of 500, 1000 and 2000 ms. In all cases, the longest APDs were measured on the endocardium and shortest in the epicardium (Figure 5.1). The last region to complete Phase 2 repolarization (as defined by $APD_{30}$) was the midmyocardium although the last region to return to resting membrane potential was the endocardium. APD (and to some extent) TDR increased in a rate-dependent manner (Table 1).

### 5.3.2 Electrotonic coupling masks M-cell $APD_{90}$ prolongation

Upon closer inspection of cellular electrical activity measured at many sites through the center of the wedge, the model predicted that $APD_{90}$ decreases monotonically from endocardium to epicardium (Figure 5.2). The results from these simulations are compared with experimental data from Yan et al (261). Model predictions of endocardial and epicardial APD closely match corresponding experimental measurements at the examined pacing rates. Among the regions in the ventricular wedge, the epicardium always displayed the briefest $APD_{90}$. Late repolarization consistently occurred in the opposite direction from activation when the pacing site was on the endocardium. However, our model fails to recapitulate a subendocardial peak in APD and an abrupt change in APD at the subepicardium.

Thus, our model predicts that differences in epicardial and endocardial repolarization times determines TDR.

### 5.3.3 Sensitivity of APD predictions to electrode positioning

Since wavefront curvature/collisions with boundaries may alter APD, we measured $APD_{90}$ both down the center and on two external faces (upper and lower) of the wedge (where experimental measurements are taken) (Figure 5.3). Endocardial $APD_{90}$ is greatest at the site of the stimulus and smallest where the activation wave hits the opposite endocardial edge (due to asymmetry in the wedge shape, the activation wave hits the upper epicardial border first, and the last region to activate is the lower epicardial border). $APD_{90}$ measurements from the center of the wedge were of intermediate value as they are neither sites of wavefront initiation or collision.

### 5.3.4 Sensitivity of APD predictions to layer thickness

Differences in the distribution of the myocyte subtypes may also modify $APD_{90}$ and TDR measurements through the wall of the canine LV wedge. In order to investigate this, we altered the thickness of the midmyocardial cell layer (Figure 5.4). The model predicted a global increase in $APD_{90}$ measurements that correlated with the thickness of the midmyocardial cell layer. However, the model did not predict any distinct differences in TDR (Table 2), consistent with a dominant role of intercellular coupling in minimizing repolarizing gradients.

### 5.3.5 Effect of reduced coupling

Reduced intercellular coupling secondary to some forms of heart disease has been proposed to predisposing the tissue to arrhythmia formation by increasing TDR. Our simulations predict that reduced coupling leads to a greater dispersion of both activation and repolarization (Figure 5.5) as compared with measurements with

normal coupling (Table 1), but compared with the differences in activation time, the changes were small.

### 5.3.6 Effect of reversal of pacing

When the pacing site is located in the middle of the epicardium, epicardial $APD_{90}$ measurements were prolonged at all cycle lengths compared with "normal" endocardial pacing (Figure 5.6). Conversely, predictions of endocardial $APD_{90}$ were shorter. These results are consistent with the modifying effect of the pacing site on measurements of $APD_{90}$. The resulting variation of $APD_{90}$ across the canine wall is very small. Epicardial pacing does however increase TDR at all pacing rates (Table 1).

### 5.3.7 Arrhythmia formation due to the I1768V *SCN5A* mutation

Simulations of activation and recovery in the canine LV wedge reveal that the I1768V mutation disrupts repolarization patterns in a rate and myocyte-subtype dependent manner (Figure 5.7). At 2 Hz, endocardial regions experience an EAD that results in a triggered epicardial AP and an "R on T" extrasystole on the ECG. When the pacing rate is slowed to 1 Hz, 2 successive endocardial EADs occur, triggering 2 epicardial APs. Upon closer inspection, the complete endocardium appears to experience the EADs, and the triggered beat is initiated in a region of the midmyocardium that has recovered and propagates over all of the non-refractory tissue.

We also investigated the proarrhythmic consequences of a sudden slowing of pacing rate (similar to a pause in pacing). In the normal canine wedge with BCL = 500ms, slowing to 2000 ms resulted in slightly increased TDR (from 13.0 to 25.3 ms). However, the same protocol applied in the presence of the I1768V mutation resulted in a brief episode of polymorphic ventricular tachycardia (PVT) that terminated

spontaneously after 1.5 seconds. This was followed by ~2 seconds of PVT that subsequently stabilized to monomorphic VT. The wedge remained in this condition despite endocardial pacing for the remainder of the simulation (~ 4 seconds) (Figure 5.8). As evident from the action potential tracings, the PVT was associated with the continuing "triggers" of EADs originating from the endocardium, and fluctuations between epicardial EADs and triggered beats.

## 5.4 Discussion

Mechanistic descriptions of CICR are lacking from many previous models of the cardiac action potential. Those that do are computationally intractable for upward integration into 2D and 3D models of coupled myocardium. In this study, we use a simplified mechanistic model of CICR as part of our models of the canine LV action potential. These models can faithfully reproduce experimentally measured properties of ECC and whole cell phenomena, and yet remain computationally efficient (65). The models were used to study the role of electrotonic coupling in modulating intrinsic differences in the $APD_{90}$ of canine ventricular myocytes during normal electrical activation and recovery, as well as the role of cellular heterogeneities in arrhythmia formation due to the I1768V *SCN5A* mutation.

This model is relevant far outside the scope of this investigation e.g the model could also be used as a tool to predict the arrhythmic mechanisms of electrical remodeling in heart failure, or to investigate the pro- or anti-arrhythmic effects of gene therapy and pharmacologic interventions. This is also the first report (of which the authors are aware) of an ionic model integrated into a 3D tissue model that incorporates 1) local control mechanisms of $Ca^{2+}$ handling and 2) descriptions of intrinsic cellular heterogeneities based on detailed experimental investigations into the molecular basis of these heterogeneities. Previous modeling work of this kind has

been limited to ionic models lacking mechanistic insight into the basis of CICR, and as such, their predictive ability is limited, especially with regards to arrhythmia formation.

### 5.4.1 Transmural heterogeneities

Cardiac myocytes isolated from the endocardium, midmyocardium and epicardium of the canine left ventricle exhibit distinct electrophysiological properties (9). However, in intact tissue, the resulting electrical gradients are much smaller due to electrotonic coupling (220). Controversy exists as to the extent that M-cells contribute to dispersion of repolarization in intact tissue. The presence of midmyocardial cells is evident in many wedge preparations (9) (219), yet other studies failed to detect transmural electrical gradients *in vivo* (15).

In this study, we simulated electrical activation and recovery in a 3D monodomain model of a heterogeneous canine left ventricular wedge. Our model predictions of epicardial and endocardial $APD_{90}$ match very well with corresponding measurements in canine wedge preparations (261) for the pacing rates under consideration. Furthermore, predicted TDR also matches reported experimental values (111).

Our results point to a transmural gradient in late repolarization proceeding from the epicardium to the endocardium. This supports the argument that electrotonic effects dominate over intrinsic cellular heterogeneities in determining the sequence of repolarization. However, we also predict that M-cells may contribute to dispersion of early repolarization. These results are consistent with our previous modeling studies in which that the greatest transmural differences occurred during Phase 2 (rather than Phase 3) repolarization.

Many of our results are consistent with and extend several prior model analyses. A previous 1D model of action potential propagation demonstrated that electrotonic

coupling had a diminishing effect on heterogeneity in the intact myocardium which depends strongly on the extent of intercellular coupling (43). Clayton et al (41) have conducted similar investigations into the contributions of heterogeneities to normal propagation and reentry. This study extends their investigations by accounting for transmural heterogeneities in a more mechanistic manner, as well as making the analysis apply specifically to canine, a species displaying some of the most distinctive (and humanlike) transmural heterogeneities. In general, previous studies have relied upon a large $I_{Ks}$ density, both for timely repolarization, and for conferral of subtype dependent $APD_{90}$ measurements (41, 61, 197, 239). In contrast, here we use a model where the heterogeneities with the biggest impact on $APD_{90}$ are $I_{Kv43}$ and $I_{NaL}$.

The intrinsic electrical properties of individual cells can be modified by their location with respect to the beginning and end of propagation and collision of wavefronts (251). Here, we observed that $APD_{90}$ measurements may be influenced by the positioning of the recording electrodes relative to the pattern of activation, which may explain some of the variability in experimental recordings.

Increasing the thickness of the M-cell region resulted in longer average $APD_{90}$ measurements, but no increase in TDR. This may be of relevance in the whole heart where there may be variation in ventricular myocyte subtype distribution. For instance, M-cells were found in the deep subepicardium in the lateral free wall of the left ventricle (9). Longer APDs in this region may lead to an increase in overall dispersion of repolarization within the ventricle. Reducing intercellular coupling and epicardial pacing tended to lead to an increase in TDR. These perturbations are both thought to be proarrhythmic.

Our results are in contrast to many experimental measurements in which the regions where the greatest $APD_{90}$ measurements were made in the deep subendocardium. The degree of TDR observed in experimental preparations also

appears to depend on the methods used to estimate the parameter. Other factors that may influence electrical measurements are the use of various anesthesia (5) or electro-mechanical uncouplers (88). The use of mathematical modeling may help to interpret these experiments.

Transmural heterogeneity of cell-cell coupling also exists, and is accounted for to some extent in our model (see Limitations section for a more detailed discussion). A sharp transition of $APD_{90}$ is observed in the layer between the subepicardium and midmyocardium (261). These observations suggest the presence of a resistive barrier, although it is unclear whether this is due to changes in extracellular matrix or gap junctional resistance. A transmural gradient of connexin43 (Cx43) expression has been measured across the left ventricular free wall of mouse and rat hearts (257) and canine (151). In these studies, measurements of subepicardial Cx43 expression were significantly reduced relative to midmyocardial and subendocardial layers. The laminar arrangement of myocytes with transmural variation in the orientation of so-called cleavage planes may also play a role in heterogeneity of electrotonic coupling (99). Layers of tightly coupled ventricular myocytes run are oriented in the radial direction with muscle branching permitting interlayer electrical connectivity. Reduced branching in the midmyocardium may play a role in creating convoluted paths of activation. This ventricular structural anisotropy is thought to play a role in arrhythmogenesis (99) and defibrillation (229).

### 5.4.2 Mechanisms of arrhythmia formation

Another goal of this study was to investigate how a LQT3 mutation promotes arrhythmia formation in the intact ventricular myocardium. The exact mechanisms of ventricular arrhythmia in LQTS patients, in particular induction of TdP, remain poorly understood. It is generally accepted that mere QT prolongation is not proarrhythmic,

but that increased dispersion of repolarization that accompanies long QT intervals leads to an unstable electrical substrate (11). It is hypothesized that amplification of intrinsic electrical heterogeneities may underlie increased repolarization gradients. Although there exist apical-basal (48) and RV-LV (242) differences in cellular electrical properties, *transmural* heterogeneities are arguably the most distinct and well studied.

Owing to the infeasibility of breeding large mammals with specific gene defects, explorations into the mechanisms of arrhythmia formation in LQTS are typically carried out in pharmacologically altered ventricular wedge preparations (often, but not always, canine). Drugs that block or enhance the function of specific ion channels are assumed to represent certain variants of LQTS (e.g. $I_{Ks}$ – LQT1, $I_{Kr}$ – LQT2 and $I_{NaL}$ – LQT3). In many instances, results from these investigations are lumped together, despite evidence that different ion channel mutations might produce distinctive ECG patterns (169).

Investigators have typically reported EADs originating from Purkinje fibers or M-cells (11). However, M-cells are often defined as the region(s) where $APD_{90}$ is longest (termed "functional" M-cells), which adds confusion to the debate over the role of M-cells in arrhythmogenesis (111). In patients with LQTS, onset of TdP frequently develops in a pause-dependent fashion (238). Optical imaging in pharmacologically altered canine ventricular wedges (representative of LQT2 and LQT3) suggested an increase in $APD_{90}$ dispersion following a pause as compared with baseline (111).

Here, the model predicted incidences of endocardial EADs as a result of the increased rate of recovery from inactivation of the $Na^+$ channel due to the I1768V *SCN5A* mutation. These EADs propagated to adjacent regions and elicited triggered responses ("R on T" extrasystoles). They also appeared to induce a short episode of a TdP-like polymorphic ventricular tachycardia following a sudden reduction in pacing

rate. These results are similar to observations of phase 2 EADs in a rabbit ventricular wedge model of acquired LQTS (262) as well as spontaneous premature beats in a canine ventricular wedge model of acquired LQT3 (111).

The relevance of these results is likely to extend to arrhythmia formation in humans. Similar gradients of Kv4.3 and KChIP2 isoforms have been observed in human hearts (130), suggestive of a common mechanism of $I_{Kv43}$ channel regulation. M-cells are also observed in humans, with similar characteristics, although the spike-and-dome morphology is less pronounced (54, 104).

### 5.4.3 Limitations

One of the major limitations of the FE models described in this study is that we have used the monodomain approximation for all simulations of electrical propagation. Here, the resistance for transmembrane potential "diffusion" represents the global average of intra-, extra- and inter-cellular resistances. Of the three, intercellular resistance is likely to be the greatest, as charged particles must diffuse through gap junctions. As a result, the level of coupling may be overestimated in these and other simulations that employ a continuum approach. This may explain some of the discrepancies between experimentally measured repolarization gradients and our predictions.

The $Ca^{2+}$ handling employed in this whole cell model presents an improved approach to previous models. However, it fails to incorporate $[Ca]_{SR}$ dependent release of SR $Ca^{2+}$ through the RyR, one of the mechanisms underlying delayed afterdepolarizations (DADs). We consider it unlikely that the conditions used in this study would facilitate the development of DADs in vivo and thus it is not a severe limitation.

Although we endeavored to account for all experimentally measured transmurally heterogeneous ionic currents, we did not include regional variation of the $Na^{+}$-$Ca^{2+}$ exchanger current ($I_{NaCa}$). A recent report described the presence of a transmural gradient of $I_{NaCa}$ in the canine LV free wall (decreasing from epicardium to endocardium) (255). However, a prior investigation into $I_{NaCa}$ gradients measured the greatest current densities in midmyocardial cells (274). Moreover, a recent study reported a reversal of the $I_{NaCa}$ gradient in normal guinea pig hearts, decreasing from endocardium to epicardium (246) (although this may be due to interspecies variability). It is therefore difficult to establish the true nature of the transmural gradient of $I_{NaCa}$ from these reports.

The estimated volume of M cells in the left ventricular wall has been suggested to be 30% (54). However, experimental reports provide no clear indications as to how these M-cells are arranged. Previous modeling work has demonstrated a minimal effect of midmyocardial cell arrangement on patterns of activation and recovery in 2D tissue slices (41). Our results are consistent with these and we therefore do not consider the exact configuration of the layers to play a significant role in our results.

### 5.4.4 Conclusions

Here, we present a multiscale model linking a genetic mutation to its clinical electrocardiographic phenotype. This study is the first of which we are aware that utilizes a model based on biophysical and molecular interactions to explore the consequences of transmural heterogeneities of ion channel *and* $Ca^{2+}$ handling proteins in normal and diseased hearts. These mechanistic models are ideal for further investigations into the pro and anti-arrhythmic effects of pharmacologic interventions and for elucidating the mechanisms of arrhythmia.

**Table 5.1:** Transmural dispersion of repolarization in ms under normal conditions, with reduced coupling and with epicardial pacing.

| | Basic cycle length (ms) | | |
|---|---|---|---|
| | 500 | 1000 | 2000 |
| Normal | 13.0 | 12.7 | 33.9 |
| Reversal of pacing | 34.4 | 29.9 | 42.3 |
| Reduced coupling | 23.2 | 18.6 | 32.4 |

**Table 5.2:** Transmural dispersion of repolarization as a function of midmyocardial layer thickness. BCL = 1000 ms.

| Midmyocardial layer thickness (%) | 81.25 | 68.75 | 56.25 | 43.75 | 31.25 | 18.75 | 6.25 |
|---|---|---|---|---|---|---|---|
| TDR (ms) | 9.2 | 12.6 | 13.8 | 13.0 | 12.7 | 10.4 | 11.4 |

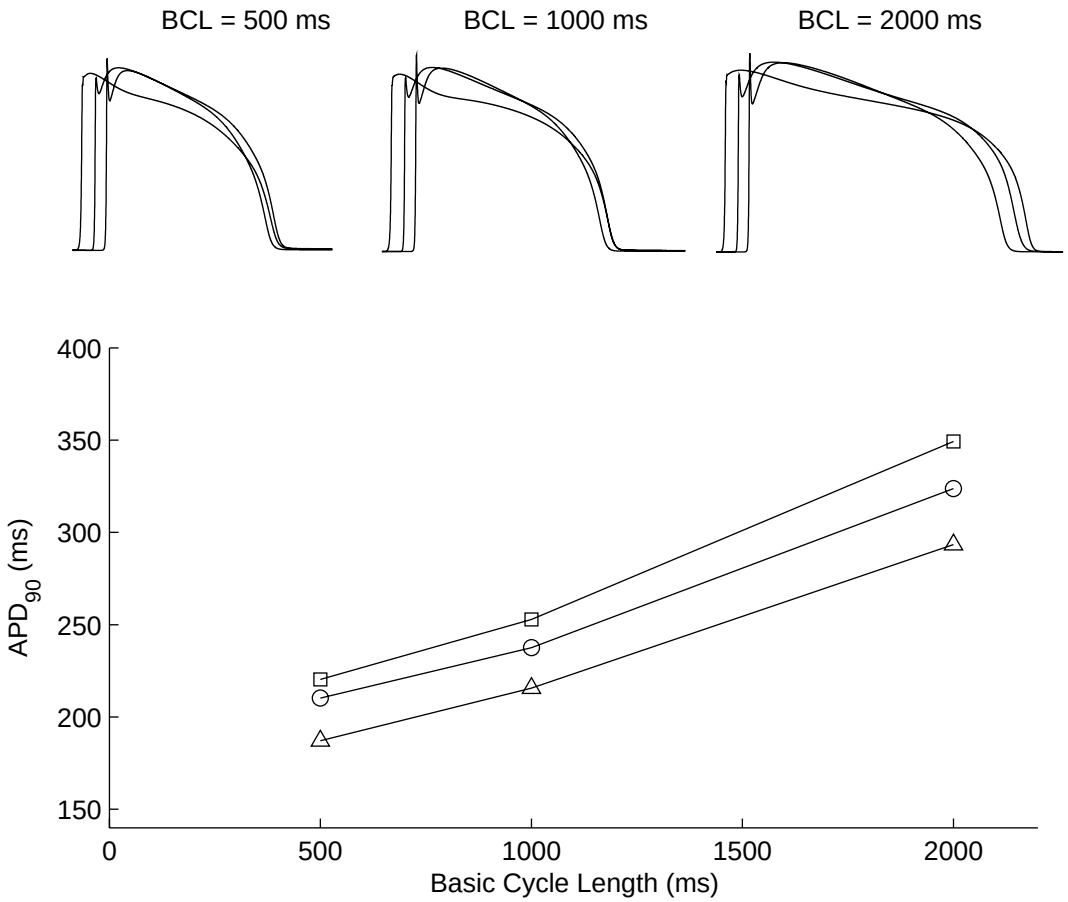


**Figure 5.1:** $APD_{90}$-rate relations in the canine LV wedge model at sites in the epicardium (Δ), endocardium (□) and midmyocardium (○). Three measurements in each region were recorded and averaged.

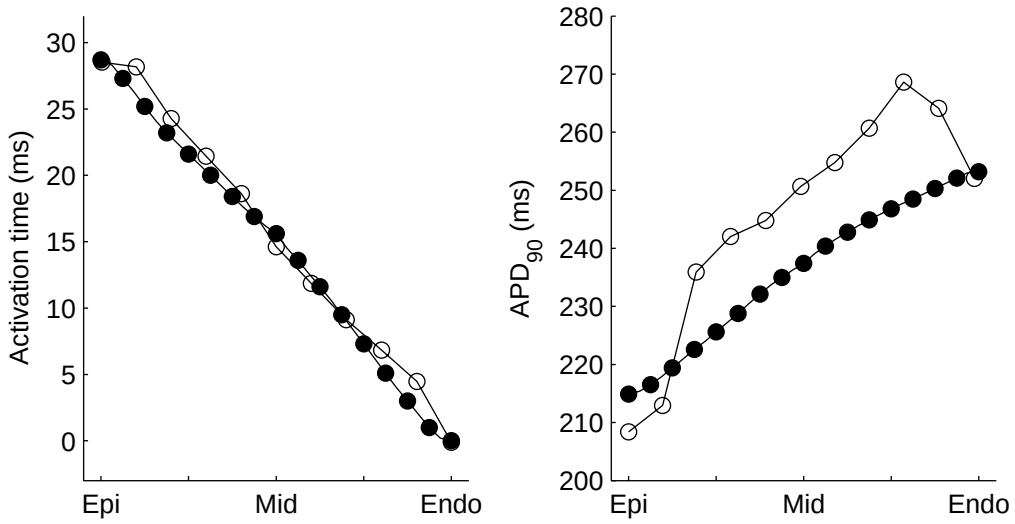


**Figure 5.2:** Distribution of $APD_{90}$ across the wall of a canine LV wedge model paced at 1000 ms (•) as compared with experimental results (○). Every second model prediction is omitted for clarity. Epi indicates epicardium; Mid, midmyocardium; Endo, endocardium.

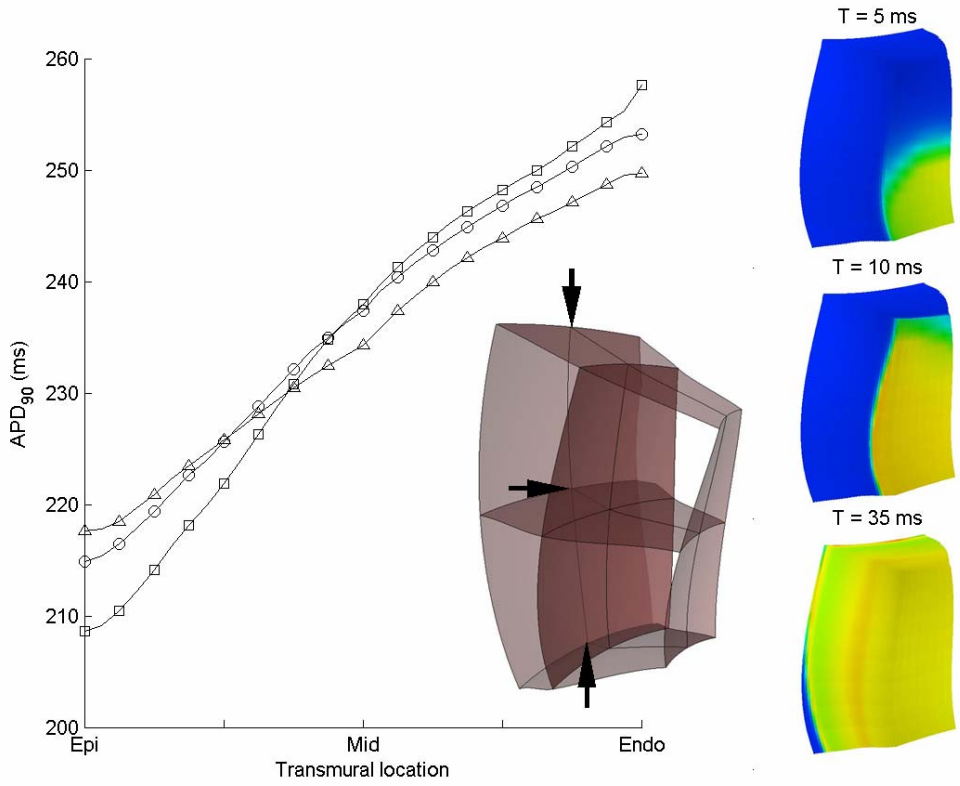


**Figure 5.3:** (Left) $APD_{90}$ measurements from the center of the wedge (○), lower face (□) and upper face(Δ). BCL = 1000ms. The arrows indicate the outermost sites of the three sets of measurement locations. (Right) Activation patterns at 5, 10 and 35 ms after the initial stimulus.

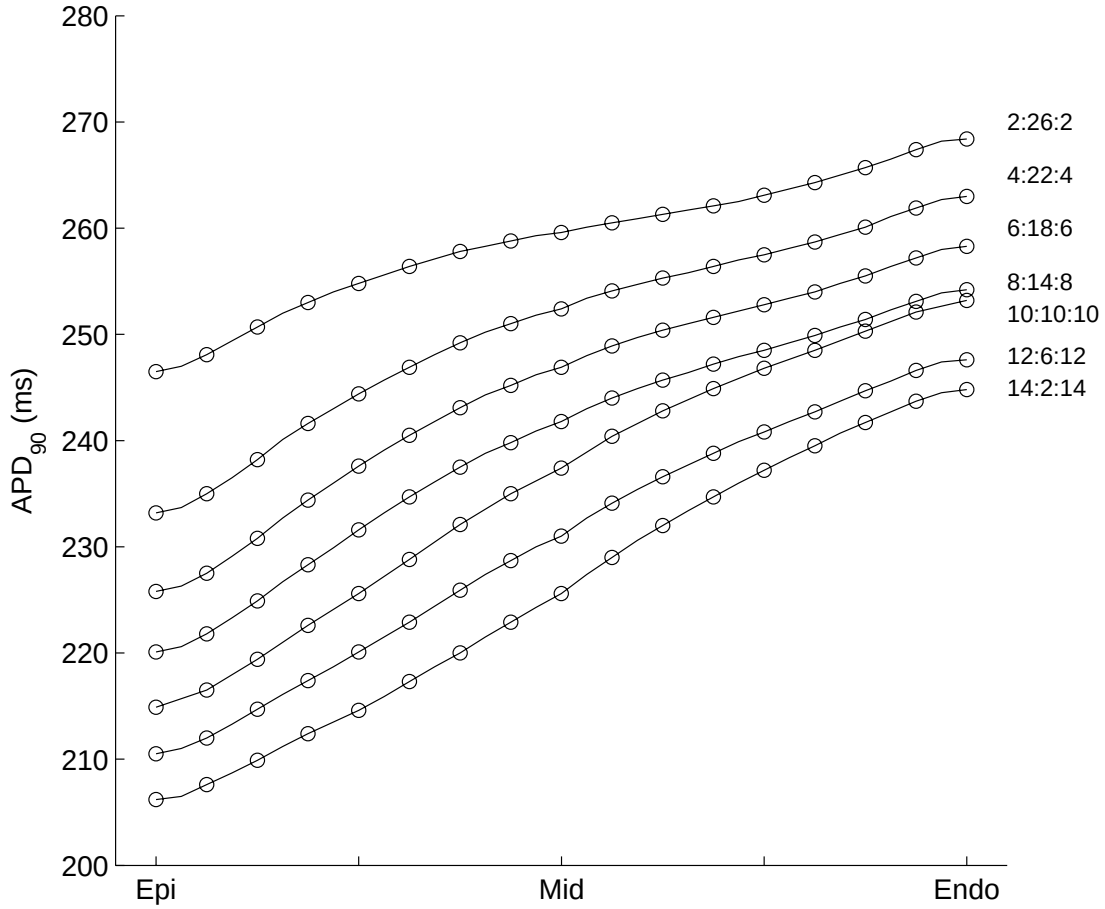


**Figure 5.4:** Altered layer thicknesses and $APD_{90}$ through the wall of a canine LV wedge. The layer thicknesses (Epi:M:Endo) were: 2:26:2, 4:22:4, 6:18:6, 8:14:8, 10:10:10, 12:6:12, 14:2:14. TDR for the 7 cases was: 9.2, 12.6, 13.8, 13.0, 12.7, 10.4, 11.4 respectively.

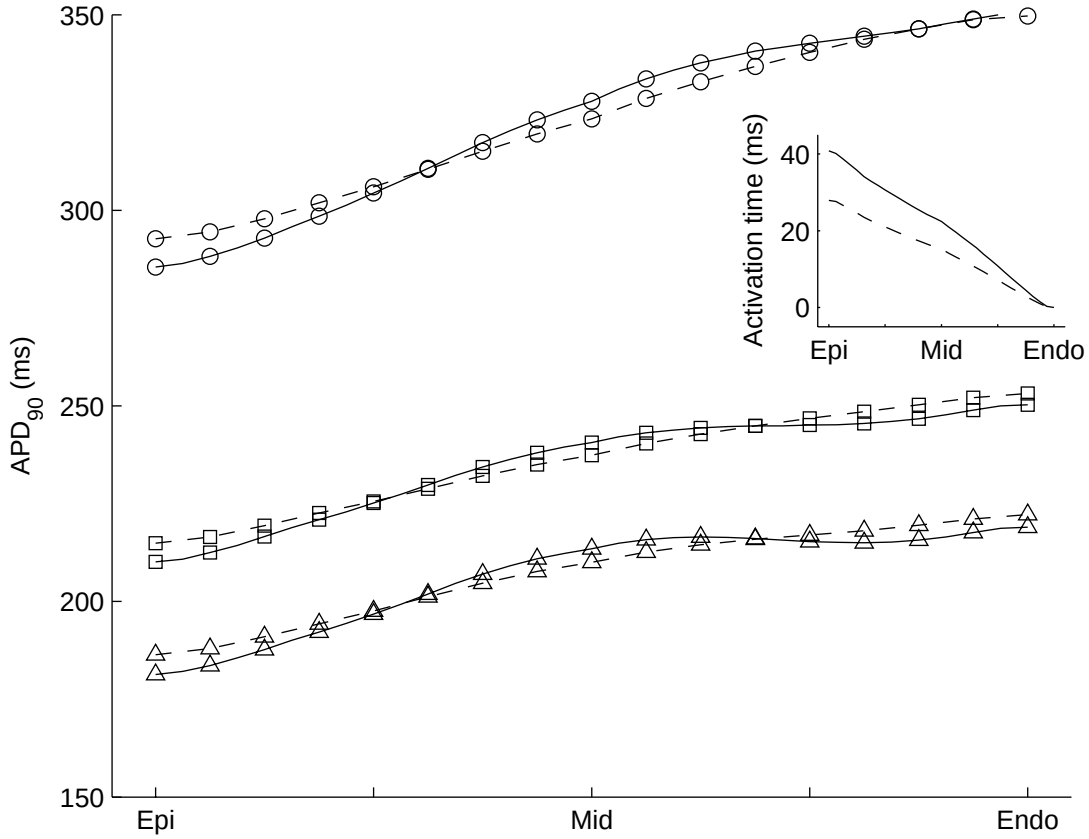


**Figure 5.5:** Reduced coupling leads to a greater variation in $APD_{90}$ across the wall of a canine LV wedge. It also leads to greater dispersion of activation (see inset).

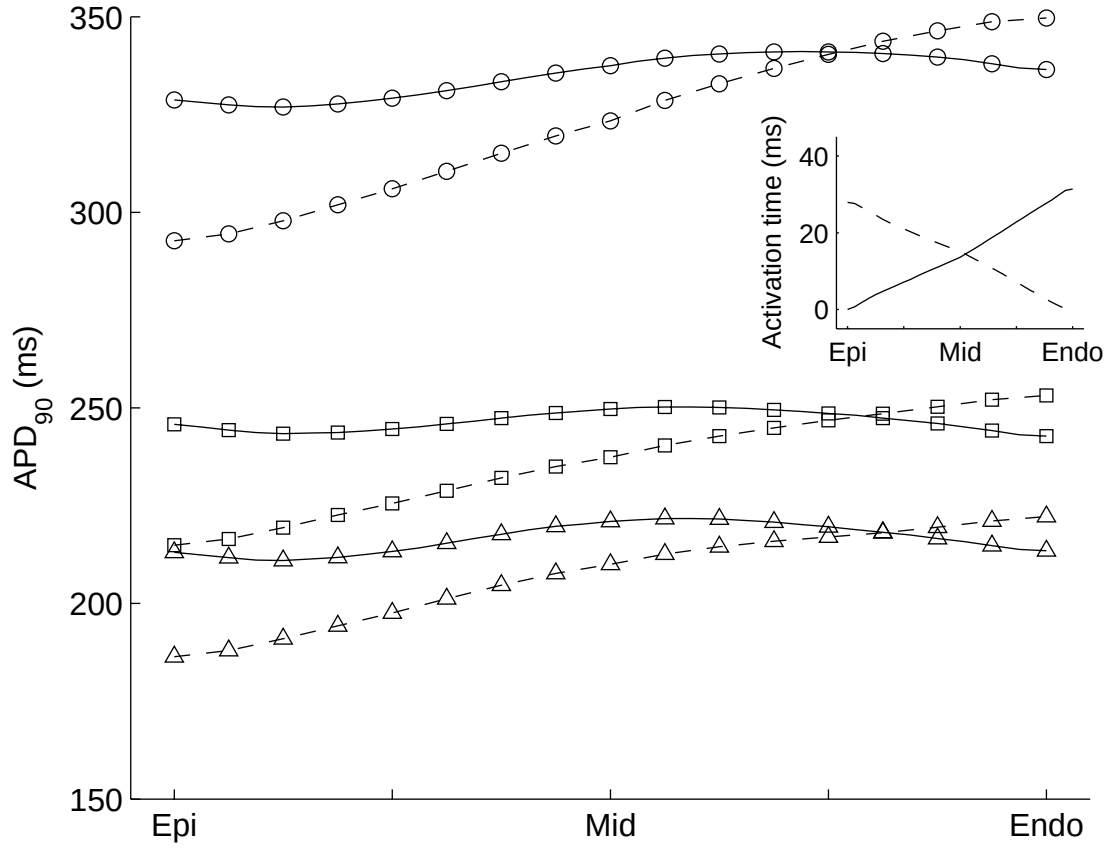


**Figure 5.6:** Epicardial pacing greatly alters the distribution of $APD_{90}$ across the wall of a canine LV wedge. Activation times between the endocardium and epicardium are reversed (see inset).

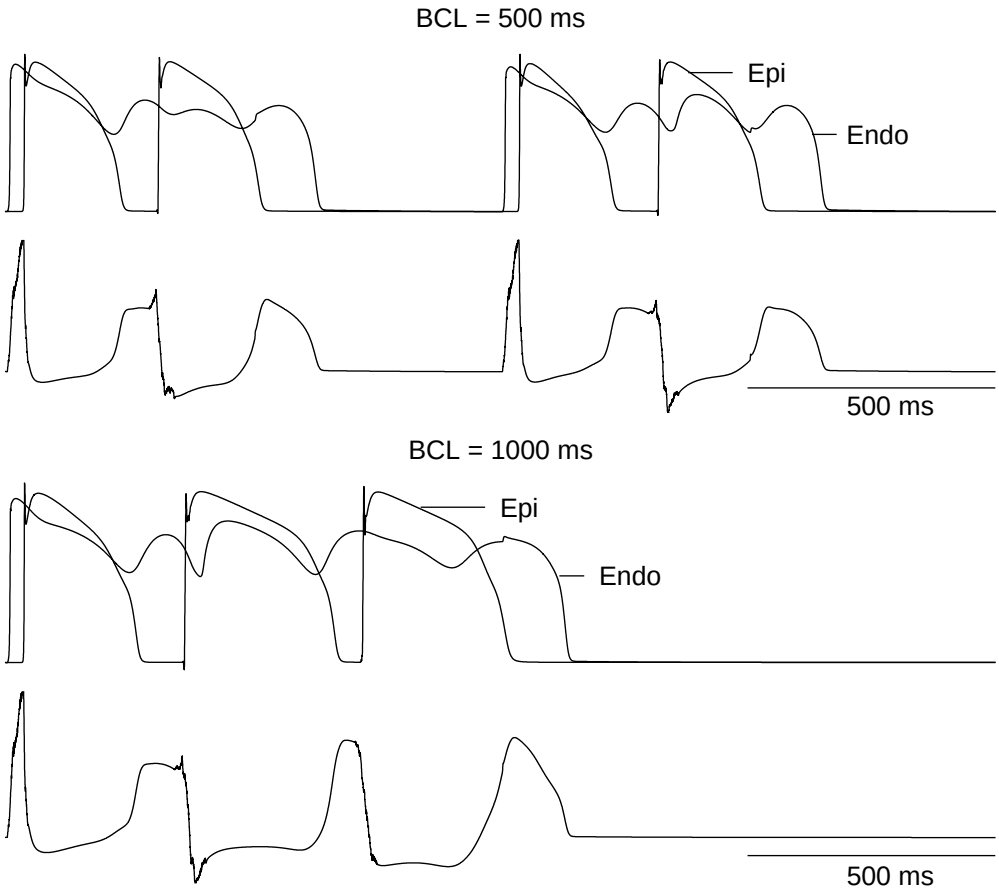


**Figure 5.7:** Abnormal triggered beats on the epicardium resulting from endocardial EADs with corresponding ECG recordings at basic cycle lengths of 500 and 1000 ms.

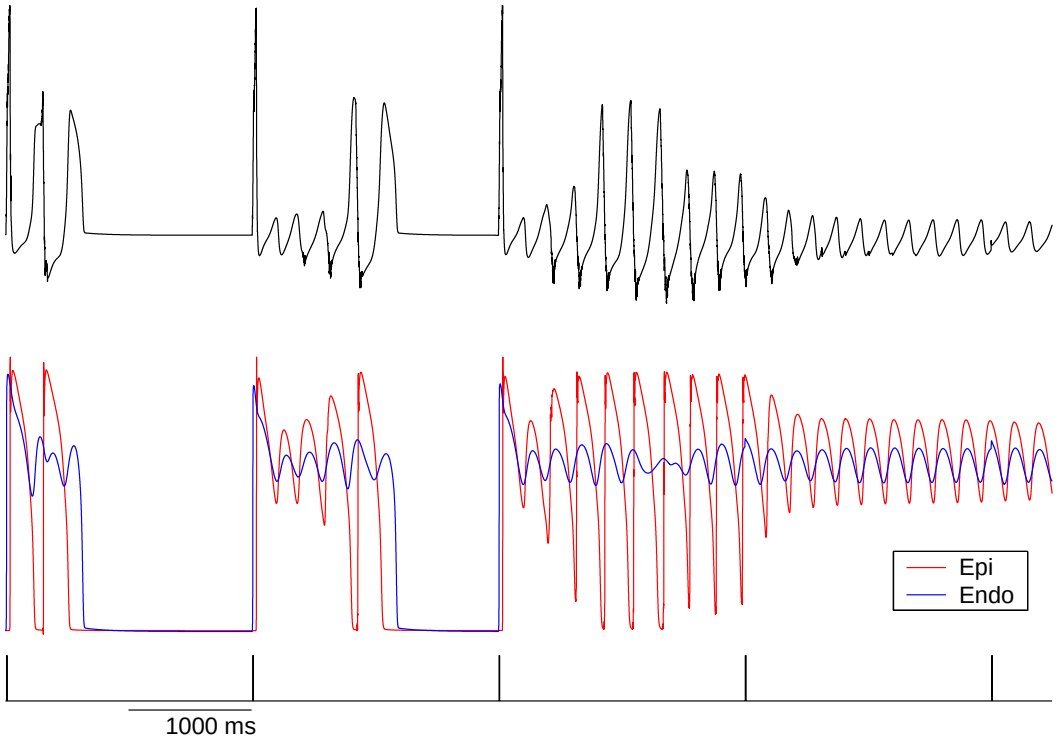


**Figure 5.8:** ECG and action potential tracings from the I1768V mutant wedge displaying repolarization-related disrhythmias following a sudden change in BCL from 500 ms to 2000 ms.

# CHAPTER 6

## Summary and Conclusions

To understand normal cardiac electrophysiology and how it becomes dysfunctional requires knowledge of the multiscale and heterogeneous nature of the heart. High resolution experimental measurements of the global spread of activation and recovery patterns remains elusive due to tissue damage from recording electrodes. Computational modeling can aid in interpreting this sparse mapping data and can be used to provide insights in the biophysical phenomena underlying the physiology and pathophysiology of cardiac electrical activity. Models inevitably make simplifications and assumptions and careful validation against experimental data is vital in confirming the predicative ability of the model. A more complete knowledge of normal cardiac electrophysiology and the mechanisms underlying arrhythmia will help to increase the likelihood of clinical success in controlling serious ventricular arrhythmias with pharmacologic agents.

Despite intensive investigation, the cellular mechanisms for most cardiac arrhythmias have not been clearly established. In particular, the contributions of transmural cellular heterogeneities to ventricular arrhythmogenesis are unknown. Thus, the objective of this dissertation was to create biophysically detailed multiscale models to investigate the proarrhythmic consequences of several different heritable ion channel mutations on action potential propagation and recovery in heterogeneous tissue.

## 6.1 Contributions to understanding arrhythmia mechanisms

The exact mechanisms of ventricular arrhythmia in LQTS patients, in particular induction of TdP, remain poorly understood. It is generally accepted that mere QT prolongation is not proarrhythmic, but that increased dispersion of repolarization accompanying long QT intervals leads to an unstable electrical substrate (11). It is hypothesized that amplification of intrinsic electrical heterogeneities may underlie increased repolarization gradients. Although there exist apical-basal (48) and RV-LV (242) differences in cellular electrical properties, *transmural* heterogeneities are arguably the most distinct and well studied.

Incorporating the molecular consequences of the KCNQ1-G589D defect into a mathematical model of the rabbit ventricular myocyte, we found increased APD and a susceptibility to afterdepolarizations only with sympathetic stimulation (189). Extending spatially to model a rabbit ventricular wedge preparation, we examined the role of interactions between these cellular mechanisms, cell-type heterogeneities, and fiber angle distributions on action potential propagation and simulated ECGs. These analyses suggest a mechanistic link from the KCNQ1-G589D gene defect to TDR and possible T-wave abnormalities in the ventricle, clinical indicators of arrhythmic risk in LQT syndrome.

The SCN5A-I1768V mutation appears to result in much more severe clinical phenotype. Here, our canine model predicts incidents of endocardial EADs as a result of the increased rate of recovery from inactivation of the mutant $Na^+$ channel. These EADs propagated to adjacent regions and elicited triggered responses ("R on T" extrasystoles). They also appeared to induce a short episode of a TdP-like polymorphic ventricular tachycardia following a sudden reduction in pacing rate. These results are similar to observations of phase 2 EADs in a rabbit ventricular

wedge model of acquired LQTS (262) as well as spontaneous premature beats in a canine ventricular wedge model of acquired LQT3 (111).

The relevance of these results is likely to extend to arrhythmia formation in humans. Interspecies variability of cardiac ion channel function and regulation does is not great between larger mammals (e.g. humans, canine, rabbit). Specifically, similar gradients of Kv4.3 and KChIP2 isoforms have been observed in human hearts (130), suggestive of a common mechanism of $I_{Kv43}$ channel regulation. M-cells are also observed in humans, with similar characteristics, although the spike-and-dome morphology is less pronounced (54, 104).

## 6.2 Contributions to high performance computing of cardiac electrophysiology

Integration across multiple physical scales and biological functions in simulating cardiac electrophysiology is now feasible in current cardiac models. These structurally and functionally integrated models of cardiac electrophysiological function combine data-intensive cellular systems models with compute-intensive anatomically detailed multiscale simulations. Numerical models help in generating hypotheses in an iterative manner together with experiments and are on the threshold of becoming helpful tools in the clinic.

Here, we present multiscale models linking genetic mutations to clinical electrocardiographic phenotypes. This study is the first of which we are aware that utilizes a model based on biophysical and molecular interactions to explore the consequences of transmural heterogeneities of ion channel and $Ca^{2+}$ handling proteins in normal and diseased hearts. These mechanistic models are ideal for further investigations into the pro and anti-arrhythmic effects of pharmacologic interventions and for elucidating the mechanisms of arrhythmia.

## 6.3 Limitations

One of the major limitations of the FE models described in this dissertation is that we have used the monodomain approximation for all simulations of electrical propagation. While this is appropriate for the scope of the investigations, future studies may require the full bidomain model.

Although we successfully employed data parallelization techniques to decrease simulation execution times, further efforts are required to decrease memory requirements for simulations in larger 3D tissue models.

## 6.4 Future Directions

Both the models and the novel computational methods developed are applicable outside the scope of this thesis. Potential future applications for the rabbit model are somewhat limited due to the phenomenological formulation of the $Ca^{2+}$ handling equations. Among other things, this model fails to account for $Ca^{2+}$-dependent inactivation of $I_{CaL}$. Intracellular $Ca^{2+}$ cycling is an important regulator of normal and abnormal ECC. This motivated the transition to the Greenstein model for subsequent investigations of arrhythmogenesis.

We modified the Greenstein model of canine midmyocardial ECC by 1) replacing the Hodgkin-Huxley formulation of $I_{Na}$ with an existing Markov model of Nav1.5 that incorporated a sustained component of this current, $I_{NaL}$; 2) including a $Ca^{2+}$-dependent inactivated open state of the Kv4.3 channel and 3) modifying parameters to reflect experimentally measured transmural heterogeneities of ionic currents. This model has the potential to be extended in a number of ways. Markov models of ion channels permit investigations into the consequences of subtle gating transitions (arising from e.g. regulation by accessory subunits, ion channel defects or pharmacologic interventions) on whole cell ECC.

This model may also be used to address the complex issue of arrhythmia mechanisms in failing hearts. Ventricular tachyarrhythmias occur in 85% of patients with congestive heart failure (CHF). Nearly half of all deaths in patients with CHF are due to these arrhythmias degenerating to VF, leading to SCD. The failing heart undergoes a complex series of changes with unpredictable and sometimes paradoxical consequences. Biophysically detailed models of whole cell ECC with realistic Ca2+-handling and regulation by the SNS integrated into a 3D model of heterogeneous ventricular tissue may aid in gaining an understanding of the underlying mechanisms of electrical instability in these patients.

The methods developed in this thesis may also be used to perform simulations of action potential propagation in models of the full right and left ventricles. Here, it will also be important to include other sources of electrical heterogeneity including those arising from the Purkinje fibers (47), interventricular heterogeneities (242), apical-basal heterogeneities (217).

Our results also suggest a number of potential opportunities for further *experimental* investigation, including additional examination of transient outward currents in canine endocardial myocytes and the detailed nature of the transmural heterogeneity of $I_{NaCa.}$

# APPENDIX A

## Restitution properties of rabbit epicardial myocytes

The restitution properties of the cardiac action potential and conduction velocity have been shown to play a role in the stability of reentrant arrhythmia. Restitution is defined as the influence of the preceding diastolic interval (DI) on either APD or CV. Cells and tissues with properties corresponding to portions of the APD restitution curve that are steep (> 1) are thought to be electrically unstable in that they will experience electrical *alternans* (oscillations between long and short APDs). Recent clinical studies have linked alternans with VF formation (175, 206). However, not all preparations with restitution curves > 1 exhibit alternans (20), and alternans can occur without the presence of a steep restitution slope (37). Simulations have indicated that electronic coupling and memory effects may play a role in modifying the degree of stability of waves (35). $Ca^{2+}$ cycling also appears to be a critical determinant of APD alternans and restitution steepness (62). Recently, Taggart et al demonstrated that the adrenergic agonists isoprenaline and adrenaline increased the steepness of the slope of the action potential duration (APD) restitution curve (218).

Families of S1-S2 restitution curves were measured from simulations of APs from rabbit epicardial, midmyocardial and endocardial myocytes. These curves were obtained by pacing at a fixed cycle length until steady-state, and then introducing a subsequent stimulus after a certain DI. The DI and APD of the ensuing beat constitute a single point on a restitution curve. By varying the DI, a full restitution curve is obtained.

At pacing rate of both 1 and 3 Hz, the model predicted some steepening of the restitution curve at short diastolic intervals in response to isoproteronol (Figure A.1).

However, it was not as marked as in experimental preparations (218). The model also failed to predict restitution of intracellular $Ca^{2+}$ release (Figure A.2), as observed by Goldhaber et al (62), which we surmise may account for the altered dynamic properties following application of isoproteronol. Specifically, we speculate that steepening of the restitution curve at small diastolic intervals arises in part from elevated diastolic $Ca^{2+}$ (from the previous $Ca^{2+}$ transient) that reduces $I_{CaL}$ via a $Ca^{2+}$-dependent mechanism. The application of $\beta_1$ adrenergic agonists increases the rate of intracellular $Ca^{2+}$ uptake in the SR, thereby shortening the $Ca^{2+}$ transient. This will contribute to a steeper dependence of $APD_{90}$ on DI at very short S1-S2 intervals (while $[Ca^{2+}]_i$ is still decreasing) but a flattening at longer DIs (once $[Ca^{2+}]_i$ has returned to diastolic levels).

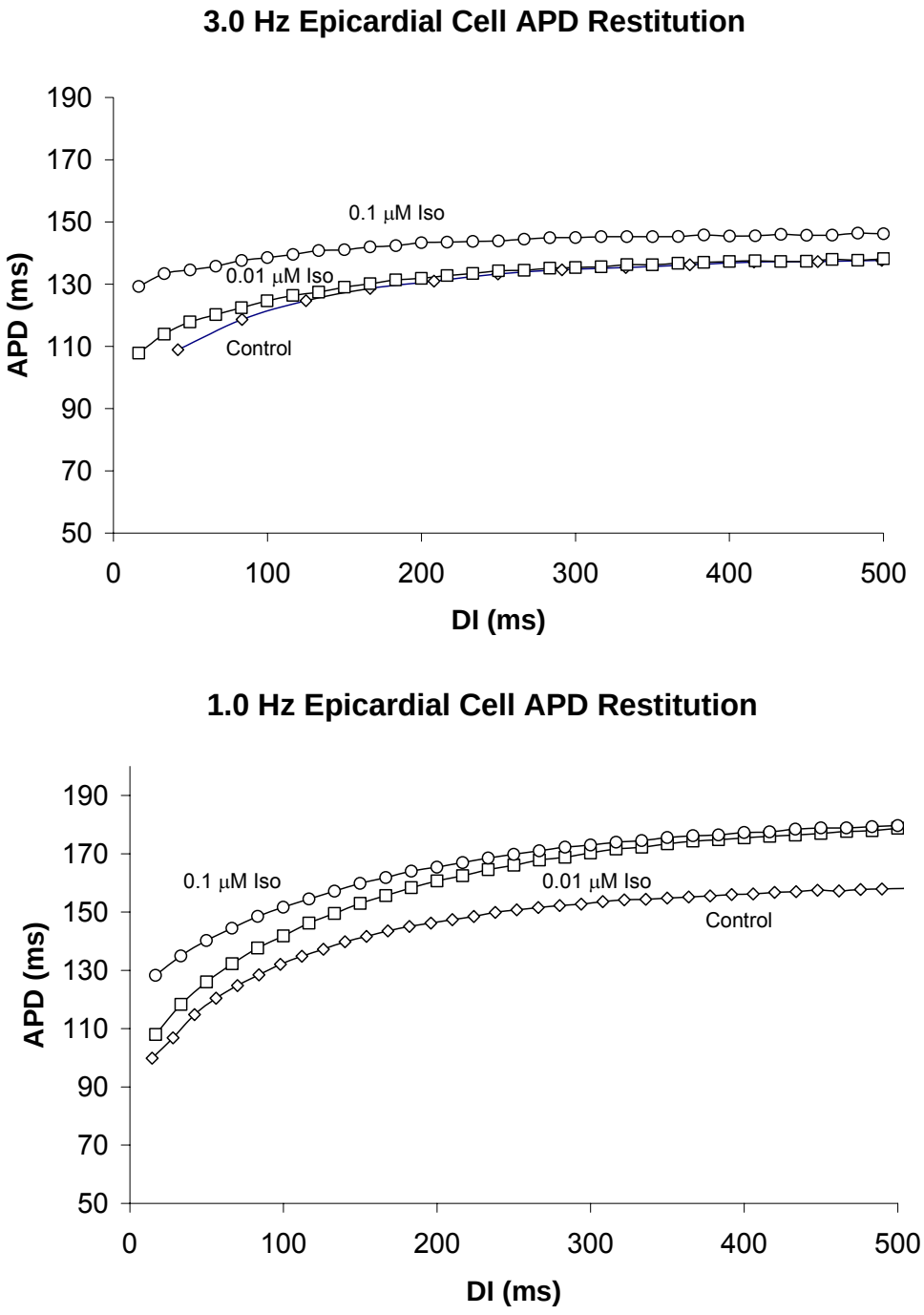


**Figure A.1:** Restitution curves for rabbit epicardial left ventricular myocytes predicted by the Saucerman model at both 3Hz and 1Hz for various concentrations of isoproteronol.

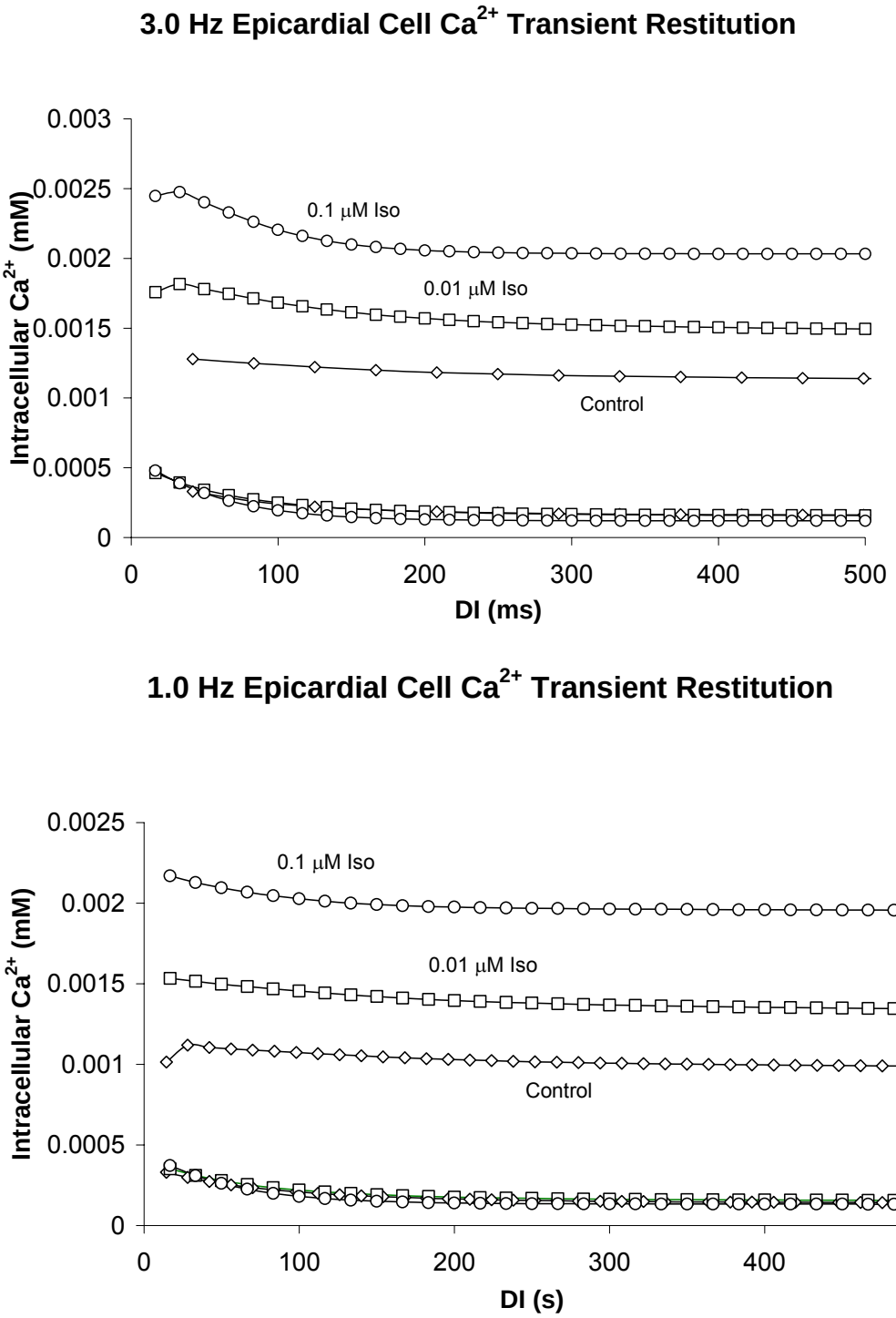


**Figure A.2:** Dynamic response of SR $Ca^{2+}$ release in rabbit epicardial left ventricular myocytes predicted by the Saucerman model at both 3 Hz and 1 Hz for various concentrations of isoproteronol.

# APPENDIX B

## Heterogeneity of cardiac innervation and TDR

From investigations into the anatomy of the cardiac nervous system, it appears that sympathetic nerves follow the common pulmonary artery into the plexus supplying the main left coronary artery, where they are distributed to the myocardium in superficial epicardial layers (271). Experimental evidence suggests that the overlap in the location of sympathetic nerves and the coronary network extends into the myocardium (271). The distribution of β-adrenergic receptors appears to be nonuniform, with the highest density occurring in the most innervated regions of the heart (34). This results in a transmural gradient of receptor density, decreasing from epicardium to endocardium (34).

We performed preliminary investigations into the consequences of heterogeneity of adrenergic activation. Despite relatively large differences in NE application (Figure B.1), our model results pointed to very small differences in TDR, both with the experimentally measured heterogeneity of sympathetic nerve terminals, and a reverse in this gradient (Figure B.2). Although larger gradients may result from local application of NE which are likely to elicit a more severe response, it is also somewhat of an unphysiological perturbation.

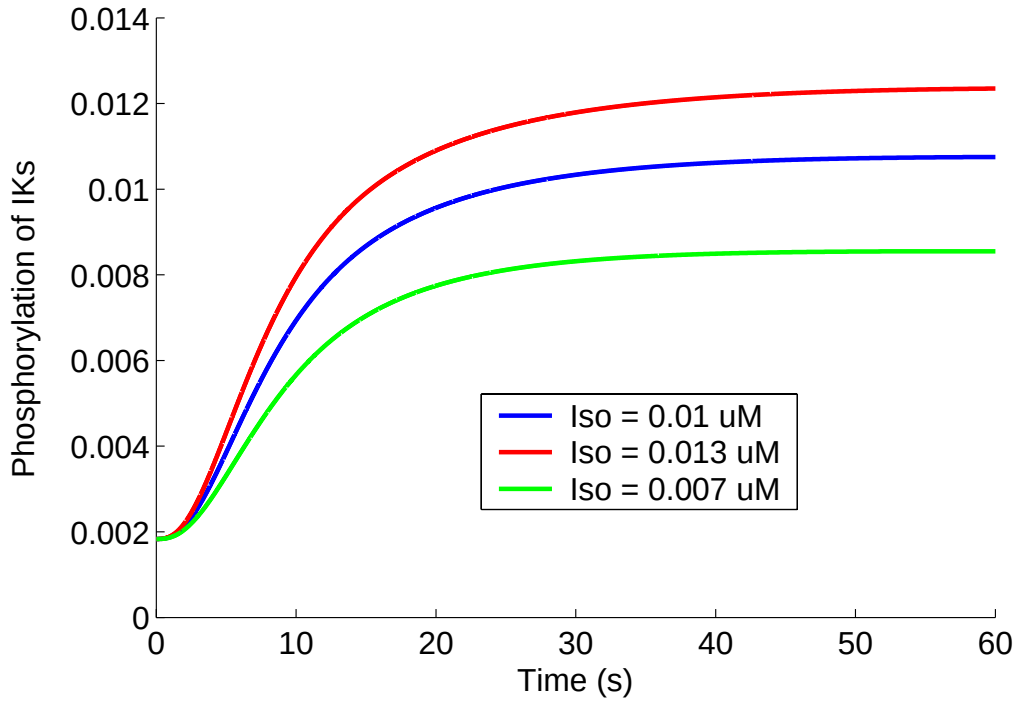


**Figure B.1:** Phosphorylation of $I_{Ks}$ on the epicardium (red), midmyocardium (blue) and endocardium (green). This gradient represents the steepest point on the dose response curve.

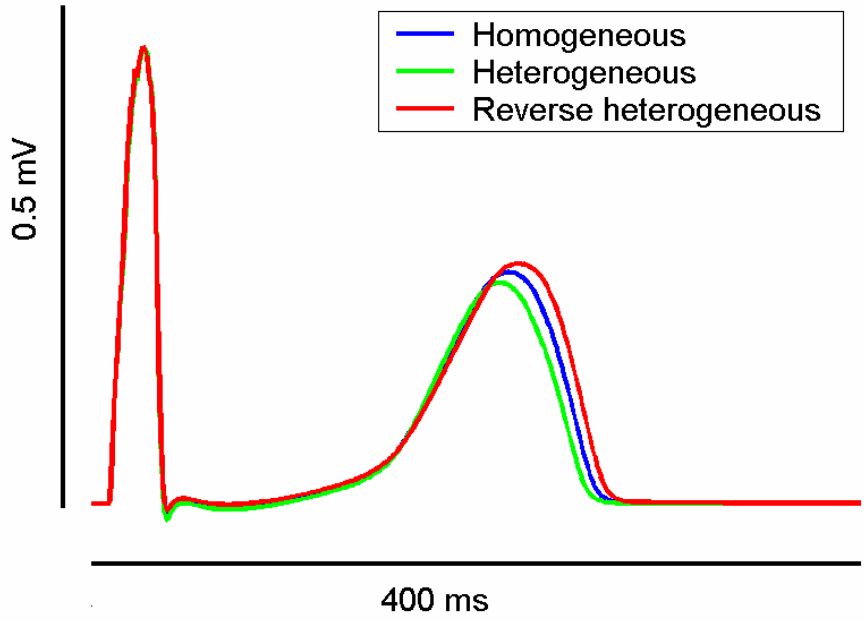


**Figure B.2:** Simulated ECGs from rabbit LV wedges with homogeneous, heterogeneous and reverse heterogeneous concentrations of isoproteronol.

# APPENDIX C

## Markov models of Kv4.3 and Nav1.5

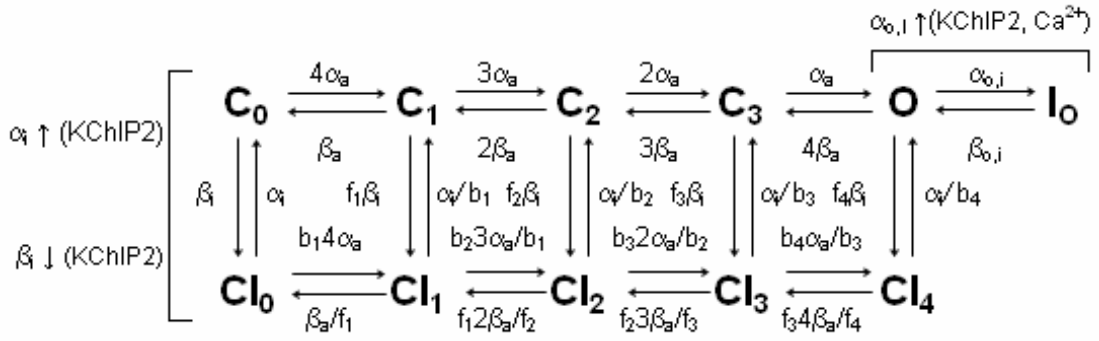


**Figure C.1:** Proposed Kv4.3 gating model including the effects of KChIP2 isoforms as suggested by Patel et al (148), but with parameters of Greenstein et al (67). $C_n$, closed states; $CI_n$, inactivated closed states; O, open state; and $I_O$, open inactivated state. KChIP2 isoforms alter gating kinetics by accelerating recovery from closed state inactivation (increasing $\alpha_i$), slowing closed state inactivation (decreasing $\beta_i$) and promoting a $Ca^{2+}$-dependent open state inactivation. Transition rates $\alpha_a$, $\beta_a$, $\alpha_i$, $\beta_i$ and $\beta_{o,i}$ are voltage-dependent, $\alpha_{o,i}$ is $Ca^{2+}$-dependent, and scaling factors ($f_1$-$f_4$, $b_1$-$b_4$) modify the interaction between activation and inactivation (67).

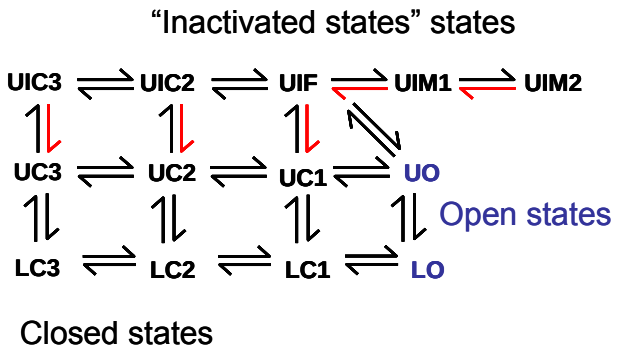


**Figure C.2:** Proposed Nav1.5 gating model of Clancy et al. The upper (U) states are part of the "background" mode whereas the lower (L) states constitute the "burst" mode. The transitions shown in red are those modified by the I1768V mutation.

# APPENDIX D

# Numerical convergence

## D.1 Numerical instabilities

Functional biophysical processes often occur on different time and spatial scales. Operator splitting (OS) methods are powerful tools for the multiscale analysis of biophysical phenomena, as they allow the use of specialized codes for different processes. Reaction-diffusion equations, such as the monodomain equation for electrical propagation, are often solved with OS methods. Operator splitting replaces the continuous interaction between diffusion and reaction with discrete interactions. The diffusion component tends to induce stability and act over long time scales, whereas the reaction term tends to induce instability and act over short time scales. Thus the reaction equations tend to be solved in smaller "sub" time-steps.

The penalty of using OS is that it may limit the numerical accuracy and order of convergence and can lead to subtle instabilities that are difficult to detect. With reaction-diffusion equations, instability usually manifests as unphysiological oscillations in time/space. Using larger diffusion steps leads to blow-up of the reaction solution. The situation when the diffusion component is highly stable and the reaction component unstable is particularly dangerous. We therefore performed careful analyses of the stability and accuracy of the FE solutions obtained with both the Puglisi-Bers and the modified Greenstein ionic models.

## D.2 Timing convergence

For the Puglisi-Bers ionic model, an OS timestep of 0.1 ms yielded stable and converged solutions. The ODEs of the ionic model were solved using RADAU5, which uses an implicit Runge-Kutta method of order 5 and adaptive time-stepping. This solver was designed for stiff equations, such as those representing ion channel gating.

One of the differences between the Puglisi-Bers and the modified Greenstein model is the replacement of Hodgkin-Huxley formulations with Markov models of ion channel function. For the fast acting $Na^+$ channel, this increased the stiffness of the system and lead to situations where the solution of the ODEs became unstable and errored out during periods when large gradients of transmembrane potential existed (as the wavefront propagates transmurally). These errors were eliminated by using an OS timestep of 0.01ms. We therefore implemented a basic adaptive time-stepping method whereby the timestep was decreased transiently during wavefront propagation (for ~50ms) and increased again once the entire mesh was activated. This successfully eliminated RADAU5 errors without too great a penalty on solution time.

Even with the adaptive time-stepping, we still observed some small amplitude, but disconcerting, oscillations at a few points on the boundaries of large 3D meshes. However, we were able to confirm that these oscillations did not affect the measurements made in the center of the mesh, which is where we recorded electrical data, or to the rendering of the solution. We therefore concluded that these meshes were borderline stable. This finding highlights yet another issue modelers must consider when implementing increasingly complex biophysically detailed models in 3D anatomical models.

We also investigated the differences in numerical convergence (with respect to time) when using 1) homogeneous and 2) heterogeneous initial conditions (ICs). In both cases, the ICs were obtained after running the single cell models for several beats until a steady-state was reached. When homogeneous ICs are used, the initial beat is discarded as the APD is not within 2% of the subsequent beats (see Figure D.1). However, when the ODE ICs are set to converged states from single cell models for the relevant ventricular myocyte subtype, the first beat was already converged to 0.5% (Figure D.2). Therefore, unless otherwise indicated, the ICs for all FE models were heterogeneous.

## D.3 Spatial resolution

The required spatial resolution for a converged solution was determined by repetitive refinement of a 3D linear 1×4×5 mm mesh. The results (Figure D.3) demonstrated that spatial convergence to less than 0.5% error was achieved at a resolution of 0.3 mm and to less than 1% error at a resolution of 0.6 mm (in terms of both activation time and action potential duration). Similar results were obtained in a 2D mesh (data not shown).

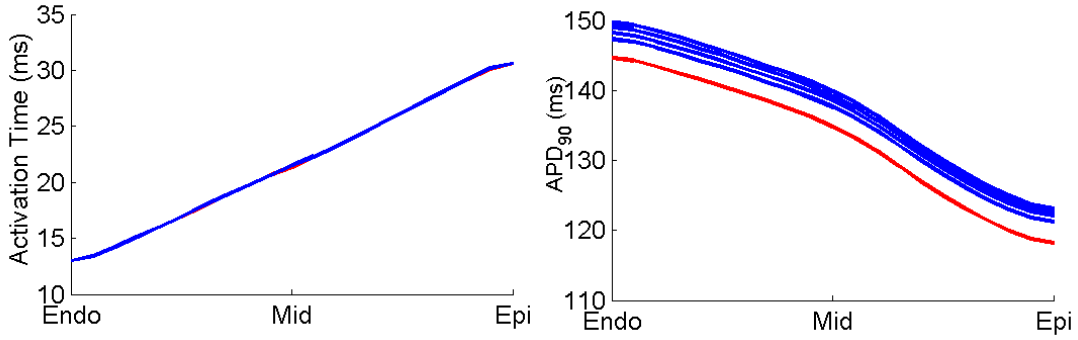


**Figure D.1:** The first 5 beats of a 2D heterogeneous model demonstrating the numerical convergence with homogeneous ICs. Recordings from the first beat are shown in red, and subsequent beats in blue.

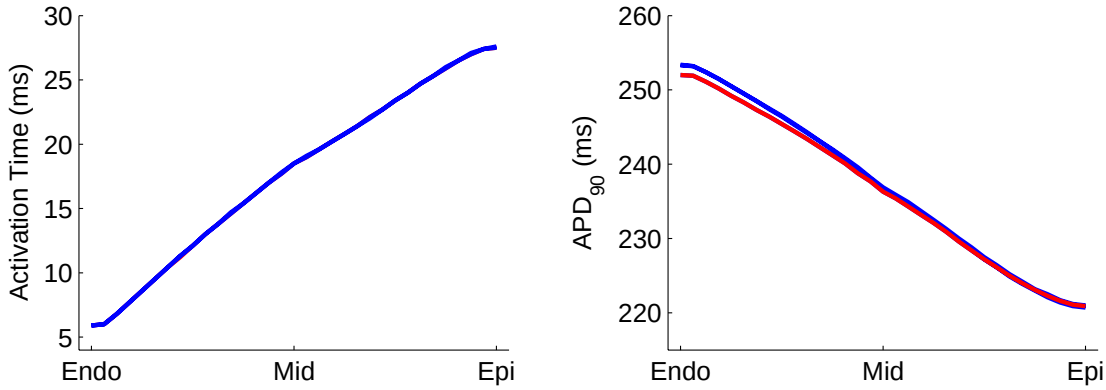


**Figure D.2:** The first 3 beats of a 3D heterogeneous model demonstrating the numerical convergence with heterogeneous ICs. Recordings from the first beat are shown in red, and subsequent beats in blue

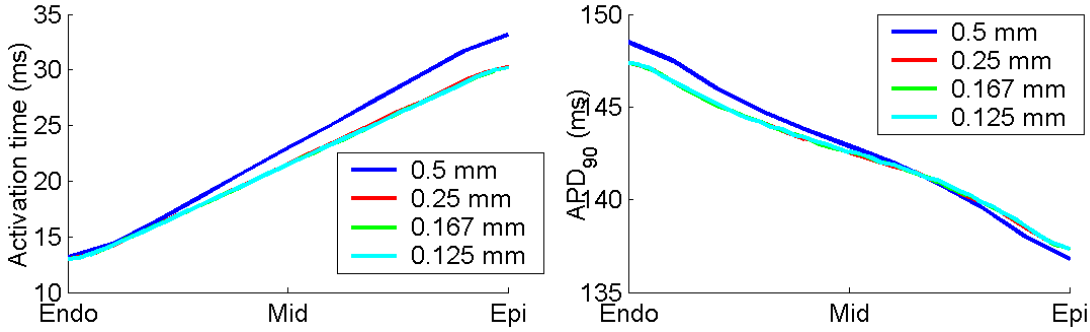


**Figure D.3:** Spatial convergence to less than 0.5% error was achieved at a resolution of 0.3 mm and to less than 1% error at a resolution of 0.6 mm (in terms of both activation time and $APD_{90}$).

# APPENDIX E

## Stimulus protocols

We investigated the strength-duration relationship for the single cell models by altering the stimulus duration and magnitude over a wide range and noting those values of the cross product which just elicited an action potential. The resulting strength-duration curve is a rectangular hyperbola as shown in Figure E.1. For single cell simulations, we selected a stimulus of 10 A/F for duration 5 ms which lies on the curve. This is consistent with the simulations in the original manuscripts (64) (159). The membrane time constant was calculated from the graph as ~18ms.

For all the FE models we attempted to stimulate as small a region as possible in order to avoid stimulus artifacts (Figure E.2). Once again, we selected a stimulus close to threshold. We also investigated the sensitivity of the FE model to suprathreshold stimuli. The threshold stimulus was 20 A/F for 5 seconds (Figure E.3). In general, with larger stimuli, the stimulus nodes produce a larger overshoot, a longer AP, and have a slightly greater conduction velocity. As the distance from the stimulus site increases, so too does the effect of the longer AP.

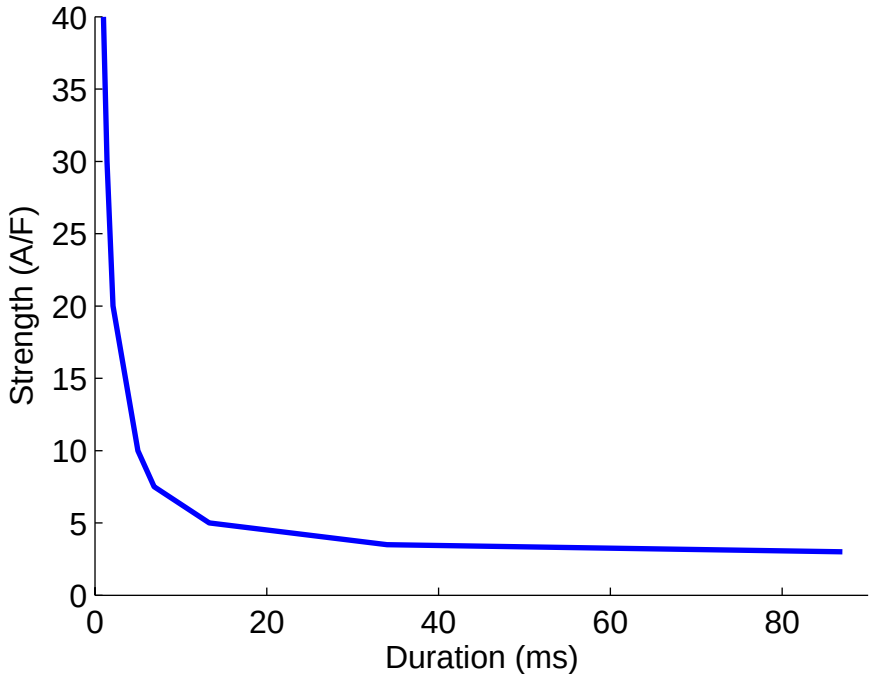


**Figure E.1:** Stimulus strength-duration curve for the modified Greenstein model.

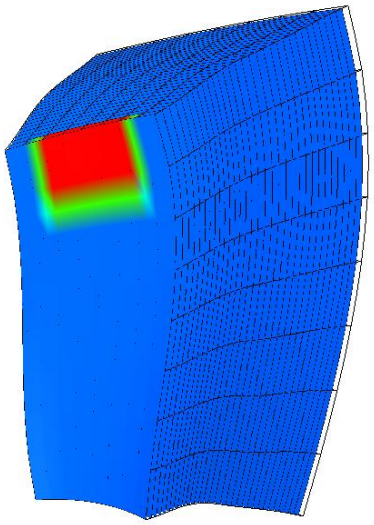

**Figure E.2:** Stimulus site for the canine left ventricular wedge studies.

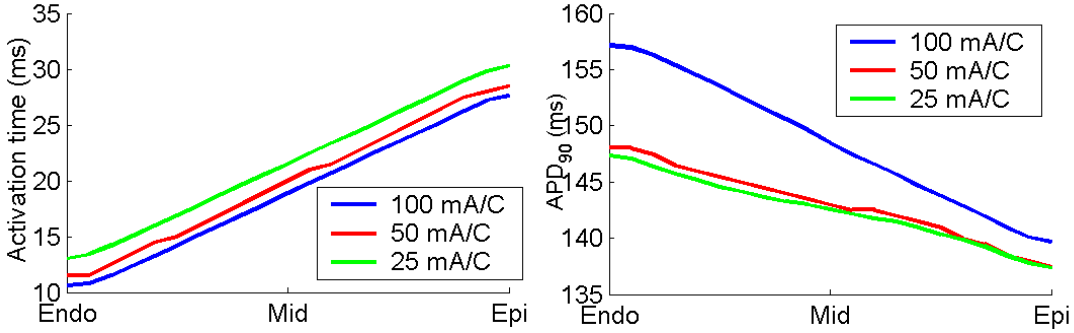


**Figure E.3:** Activation time and $APD_{90}$ as a function of suprathreshold stimulus.

# APPENDIX F

## Parallelization considerations

Parallelization techniques can be roughly divided into two categories: *data* parallelization and *control* parallelization. In data parallel applications, the same computations are performed on data that is partitioned among several processors. An example of this is in the solution of the ODEs representing the local cellular processes. If local values of membrane potential are known, the currents passing through the ion channels of a cell in one location can be calculated independently of those occurring within a cell in another location. Distributing these calculations over many processors makes feasible the integration of sophisticated ionic models (with large numbers of ODEs) into tissue and organ scale models. As the ODE calculation time grows with the sophistication of the ionic model, the solution of the linear systems do not change size or complexity. Thus for complex ionic models, the data parallel solution of the ODE portion of the problem is also where improvements in speed are most needed.

In some instances, such as for the linear solution of partial differential equations, the data is not independent and either algebraic or geometric parallelization can be employed. In algebraic parallelization of the linear solve, the global matrix is factorized on several processors, via a special parallel linear solver, such as the distributed memory version of SuperLU (106), whereas in geometric parallelization methods, as the name suggests, regions of the full mesh are distributed over the processors. The main challenge of such domain decomposition techniques is the assignment of appropriate boundary constraints to the inner non-physical boundaries. This technique requires iteration toward a converged solution with frequent updates at the boundaries.

In control parallelization, instructions (not data) are partitioned to separate processors. This can be used to help overcome the computational hurdles for creating a functionally integrated model. These problems are typically solved with different time and space scales (87, 137, 232) and therefore require schemes for synchronizing calculations and translating meshes. For smaller spatial scales, as needed for electrophysiological problems, linear hexahedral elements in the finite element method are sufficient for convergence, since higher order elements (e.g. cubic Hermite) are specifically designed to gain enough accuracy with few elements in a mesh and for the solution of higher order differential equations. Control parallelization can be exploited to allow the electrical and mechanical portions of the problem to be solved on different (groups of) processors with carefully developed communication between instances of these major problem classes.

# APPENDIX G

## Electrotonic interactions

Intrinsic electrical heterogeneities are minimized by the electrotonic interactions between electrically coupled cardiac myocytes in intact tissue. Intercellular coupling is permitted by gap junction channels composed of connexins. As adjacent cardiac myocytes become electrically uncoupled, e.g. by a drop in intracellular pH, junctional resistance ($R_j$) increases. This promotes arrhythmia formation by decreasing conduction velocity and increasing dispersion of repolarization.

Active properties of the cell membrane during the course of an action potential result in a dynamic membrane resistance ($R_m$), impacting the spread of spatial current flow during recovery (249). Although the highest measurements of $R_m$ are recorded during Phase 3 of the ventricular action potential, relatively high $R_m$ during the plateau provides a substrate in which these small net currents can modulate the AP waveform (209).

For our simulations, we used diffusion coefficients of 2.4 $cm^2s^{-1}$ in the fiber direction and 0.6 $cm^2s^{-1}$ in the transverse direction. These values correspond to conductivities of 0.48 S/m and 0.12 S/m respectively. The longitudinal conductivity is in agreement with other simulations (213)and experiments (29).

# APPENDIX H

## Finite element equations

Propagating action potentials can be described by a non-linear reaction diffusion equation:

$$\frac{\partial V_m}{\partial t} = \nabla \cdot D \nabla V_m - \frac{I_{ion}}{C_m}$$

where $V_m$ is the transmembrane voltage (mV), $I_{ion}$ is the sum of the currents that cross the membrane through ion channels ($\mu A/cm^2$), $C_m$ is the capacitance of the membrane ($\mu F/cm^2$), $D$ is the diffusion coefficient ($cm^2/ms$). The passive spread of current is governed by the diffusive term and the ionic currents (from the ionic model) by the reactive term. This parabolic system of partial different equations is solved using a hybrid collocation-Galerkin finite element method (173).

The transmembrane potential $V_m$, global coordinates, local fiber direction, and parameters of the governing equation are all approximated at each point within the domain by Lagrange or Hermite finite element interpolation. Each variable is interpolated using parameters defined at the global nodes of the finite element mesh. The value of a variable at any point within the domain is obtained by mapping the global parameters to element parameters and then forming a linear combination with the interpolating basis functions. Thus, the finite element seeks an approximate solution to the reaction-diffusion equation in the form:

$$V_m \approx \hat{V}_m = \sum \Psi_i V_{mi}$$

where Ψ are the basis functions. The element basis functions, are functions of the element coordinates only. The transmembrane potential field is always interpolated with Hermite basis functions. The solution method attempts to minimize the difference between the actual (unknown) and approximated solution.

We begin by rewriting the governing equation in component form:

$$\frac{\partial V_m}{\partial t} = \frac{\partial}{\partial x_i}\left( D^{ij} \frac{\partial V_m}{\partial x_j} \right) - \frac{I_{ion}}{C_m}$$

Here the components of the diffusion tensor are functions of the global coordinates, $x_i$. It is more convenient for us to express them with respect to the local fiber coordinate system, $v_p$, as the diffusion tensor then becomes diagonal:

$$\frac{\partial V_m}{\partial t} = D^{qr} \frac{\partial v^p}{\partial x_j} \frac{\partial}{\partial v_p}\left( \frac{\partial x^j}{\partial v_r} \frac{\partial V_m}{\partial x_q} \right) - \frac{I_{ion}}{C_m}$$

We then transform the spatial derivatives of $V_m$ to the local finite element coordinate system, $\xi$:

$$\frac{\partial V_m}{\partial t} = A^l \frac{\partial V_m}{\partial \xi_l} + B^{lm} \frac{\partial^2 V_m}{\partial \xi_l \partial \xi_m} - \frac{I_{ion}}{C_m}$$

where

$$A^l = B^{lm} \frac{\partial^2 x^j}{\partial \xi_n \partial \xi_m} \frac{\partial \xi^n}{\partial x_j} + D^{qr} \frac{\partial^2 \xi^m}{\partial v_p \partial v_r} \frac{\partial v^p}{\partial \xi_m} \frac{\partial \xi^l}{\partial v_q} + D^{qr} \frac{\partial^2 \xi^l}{\partial v_q \partial v_r}$$

and

$$B^{lm} = D^{qr} \frac{\partial \xi^l}{\partial v_q} \frac{\partial \xi^m}{\partial v_r}$$

In order to evolve a solution in time, a system of ODEs must be derived from this equation. Here we use the collocation method to satisfy the PDE at a discrete set of points. This method yields sparser finite element matrices than the Galerkin method (173).

$$\psi_{\mu(\varepsilon)} \Gamma_b^{\mu(\varepsilon)} \frac{dV_m}{dt} = \left( A^l \frac{\partial \psi_{\mu(\varepsilon)}}{\partial \xi_l} + B^{lm} \frac{\partial^2 \Psi_{\mu(\varepsilon)}}{\partial \xi_l \partial \xi_m} \right) \Gamma_b{}^{\mu(\varepsilon)} V_m - \frac{I_{ion}}{C_m}$$

Thus we end up with a system of equations of the form:

$$M \frac{dV_m}{dt} + KV_m = \frac{-I_{ion}}{C_m}$$

We must also discretize in time as well as space. Here we use a finite difference scheme:

$$M \frac{V_m^{n+1} - V_m^n}{\Delta t} + K\left[\theta V_m^{n+1} + (1-\theta) V_m^n\right] = \frac{-I_{ion}}{C_m}$$

where $\theta$ is a weighting symbol. If $\theta = 1$, the method is termed "fully implicit". When $\theta = 0$, the method is termed "explicit". We rearrange this equation to yield:

$$\left[M + \theta \Delta t K\right] V_m^{n+1} = \left[M - (1-\theta)\Delta t K\right] V_m^n - \Delta t \frac{I_{ion}}{C_m}$$

These equations form a sparse linear system which is solved with the linear solver SuperLU. The coefficient matrices do not contain any time-varying terms and thus the matrix factorization step need only be performed once. The right hand side term is updated every time step from the solution of the ODEs representing the ionic model.

Cubic Hermite interpolation results in $2^n$ parameters for each global node (where n is the spatial dimension). If we place $2^n$ collocation points within each element, the number of unknown parameters equals the number of equations, except for on the boundaries. To resolve this, we formulate Galerkin finite element equations for the boundaries. Here, we assume a no flux boundary condition:

$$\frac{\partial V_m}{\partial n} = 0$$

The Galerkin formulation is as follows:

$$\frac{\partial}{\partial t}\left(\frac{\partial V_m}{\partial n}\right) = \frac{\partial}{\partial t}\left(\frac{\partial \xi^l}{\partial x_i}\frac{\partial \xi^m}{\partial x_j}\frac{\partial Vm}{\partial \xi_m}\delta^{ij}\right) = 0$$

The term $\partial\xi^l/\partial x_i$ is the single contravariant base vector of the finite element coordinate system normal to the boundary. The boundary flux is made orthogonal to the global basis function, $\Psi_{\sigma(\varepsilon)}\Gamma_c^{\sigma(\varepsilon)}$:

$$\left(\int \frac{\partial \xi^l}{\partial x_i}\frac{\partial \xi^m}{\partial x_j}\delta^{ij}\frac{\partial \psi_{\mu(\varepsilon)}}{\partial \xi_m}\psi_{\sigma(\varepsilon)}dS\right)\Gamma_b^{\mu(\varepsilon)}\Gamma_c^{\sigma(\varepsilon)}\frac{\partial V_m}{\partial t} = 0$$

# REFERENCES


1. **Ackerman MJ, Khositseth A, Tester DJ, Hejlik JB, Shen WK, and Porter CB.** Epinephrine-induced QT interval prolongation: a gene-specific paradoxical response in congenital long QT syndrome. *Mayo Clin Proc* 77: 413-421, 2002.

2. **Akar FG, Yan GX, Antzelevitch C, and Rosenbaum DS.** Unique topographical distribution of M cells underlies reentrant mechanism of torsade de pointes in the long-QT syndrome. *Circulation* 105: 1247-1253, 2002.

3. **Allessie MA, Bonke FI, and Schopman FJ.** Circus movement in rabbit atrial muscle as a mechanism of trachycardia. *Circulation Research* 33: 54-62, 1973.

4. **An WF, Bowlby MR, Betty M, Cao J, Ling HP, Mendoza G, Hinson JW, Mattsson KI, Strassle BW, Trimmer JS, and Rhodes KJ.** Modulation of A-type potassium channels by a family of calcium sensors. *Nature* 403: 553-556, 2000.

5. **Antzelevitch C.** Heterogeneity of cellular repolarization in LQTS: the role of M cells. *Eur Heart J Suppl* 3: K2-K16, 2001.

6. **Antzelevitch C.** Ion channels and ventricular arrhythmias: cellular and ionic mechanisms underlying the Brugada syndrome. *Curr Opin Cardiol* 14: 274-279, 1999.

7. **Antzelevitch C and S S.** Clinical relevance of cardiac arrhythmias generated by afterdepolarizations. Role of M cells in the generation of U waves, triggered activity and torsade de pointes. *J Am Coll Cardiol* 23: 259-277, 1994.

8. **Antzelevitch C and Dumaine R.** Electrical heterogeneity in the heart: Physiological, pharmacological and clinical implications. In: *Handbook of Physiology, Section 2: The Cardiovascular System. Vol 1, The Heart*. Bethesda, MD: American Physiological Society, 2001, p. 654-692.

9. **Antzelevitch C and Fish J.** Electrical heterogeneity within the ventricular wall. *Basic Res Cardiol* 96: 517-527, 2001.

10. **Antzelevitch C and Oliva A.** Amplification of spatial dispersion of repolarization underlies sudden cardiac death associated with catecholaminergic polymorphic VT, long QT, short QT and Brugada syndromes. *J Intern Med* 259: 48-58, 2006.

11. **Antzelevitch C and Shimizu W.** Cellular mechanisms underlying the long QT syndrome. *Curr Opin Cardiol* 17: 43-51, 2002.

12. **Antzelevitch C and Shimizu W.** Cellular mechanisms underlying the long QT syndrome. *Curr Opin Cardiol* 17: 43-51, 2002.

13. **Antzelevitch C, Shimizu W, Yan GX, and Sicouri S.** Cellular basis for QT dispersion. *J Electrocardiol* 30 Suppl: 168-175, 1998.

14. **Antzelevitch C, Shimizu W, Yan GX, Sicouri S, Weissenburger J, Nesterenko VV, Burashnikov A, Di Diego J, Saffitz J, and Thomas GP.** The M cell: its contribution to the ECG and to normal and abnormal electrical function of the heart. *J Cardiovasc Electrophysiol* 10: 1124-1152, 1999.

15. **Anyukhovsky EP, Sosunov EA, and Rosen MR.** Regional differences in electrophysiological properties of epicardium, midmyocardium, and endocardium. In vitro and in vivo correlations. *Circulation* 94: 1981-1988, 1996.

16. **Anyukhovsky EP, Sosunov EA, and Rosen MR.** Regional Differences in Electrophysiological Properties of Epicardium, Midmyocardium, and Endocardium: In Vitro and In Vivo Correlations. *Circulation* 94: 1981-1988, 1996.

17. **Arts T, Costa KD, Covell JW, and McCulloch AD.** Relating myocardial laminar architecture to shear strain and muscle fiber orientation. *American Journal of Physiology-Heart and Circulatory Physiology* 280: H2222-H2229, 2001.

18. **Bahring R, Boland LM, Varghese A, Gebauer M, and Pongs O.** Kinetic analysis of open- and closed-state inactivation transitions in human Kv4.2 A-type potassium channels. *J Physiol* 535: 65-81, 2001.

19. **Bahring R, Dannenberg J, Peters HC, Leicher T, Pongs O, and Isbrandt D.** Conserved Kv4 N-terminal domain critical for effects of Kv channel-interacting protein 2.2 on channel expression and gating. *J Biol Chem* 276: 23888-23894, 2001.

20. **Banville I and Gray RA.** Effect of action potential duration and conduction velocity restitution and their spatial dispersion on alternans and the stability of arrhythmias. *J Cardiovasc Electrophysiol* 13: 1141-1149, 2002.

21. **Beck EJ, Bowlby M, An WF, Rhodes KJ, and Covarrubias M.** Remodelling inactivation gating of Kv4 channels by KChIP1, a small-molecular-weight calcium-binding protein. *J Physiol* 538: 691-706, 2002.

22. **Beeler GW and Reuter H.** Reconstruction of Action Potential of Ventricular Myocardial Fibers. *Journal of Physiology-London* 268: 177-210, 1977.

23. **Belik ME, Usyk TP, and McCulloch AD.** Computational methods for cardiac electrophysiology. In: *Handbook of numerical analyses, computational models for the human body*. Amsterdam: Elsevier, 2004, p. 676.

24. **Berenfeld O and Jalife J.** Purkinje-muscle reentry as a mechanism of polymorphic ventricular arrhythmias in a 3-dimensional model of the ventricles. *Circulation Research* 82: 1063-1077, 1998.

25. **Berne R and Levy M.** *Cardiovascular Physiology*. St Louis: Mosby, 2001.

26. **Bers DM.** Cardiac excitation-contraction coupling. *Nature* 415: 198-205, 2002.

27. **Bers DM and Guo T.** Calcium signaling in cardiac ventricular myocytes. *Ann N Y Acad Sci* 1047: 86-98, 2005.

28. **Bohle T, Brandt MC, Lindner M, and Beuckelmann DJ.** Identification of gating modes in single native Na+ channels from human atrium and ventricle. *Circ Res* 91: 421-426, 2002.

29. **Brown AM, Lee KS, and Powell T.** Voltage clamp and internal perfusion of single rat heart muscle cells. *J Physiol* 318: 455-477, 1981.

30. **Brunet S, Aimond F, Li H, Guo W, Eldstrom J, Fedida D, Yamada KA, and Nerbonne JM.** Heterogeneous expression of repolarizing, voltage-gated K+ currents in adult mouse ventricles. *J Physiol* 559: 103-120, 2004.

31. **Burashnikov A and Antzelevitch C.** Block of I(Ks) does not induce early afterdepolarization activity but promotes beta-adrenergic agonist-induced delayed afterdepolarization activity. *J Cardiovasc Electrophysiol* 11: 458-465, 2000.

32. **Cao JM, Chen LS, KenKnight BH, Ohara T, Lee MH, Tsai J, Lai WW, Karagueuzian HS, Wolf PL, Fishbein MC, and Chen PS.** Nerve sprouting and sudden cardiac death. *Circ Res* 86: 816-821, 2000.

33. **Cao J-M, Fishbein MC, Han JB, Lai WW, Lai AC, Wu T-J, Czer L, Wolf PL, Denton TA, Shintaku IP, Chen P-S, and Chen LS.** Relationship Between Regional Cardiac Hyperinnervation and Ventricular Arrhythmia. *Circulation* 101: 1960-1969, 2000.

34. **Cavallotti C, Bruzzone P, and Mancone M.** Catecholaminergic nerve fibers and beta-adrenergic receptors in the human heart and coronary vessels. *Heart Vessels* 17: 30-35, 2002.

35. **Cherry EM and Fenton FH.** Suppression of alternans and conduction blocks despite steep APD restitution: electrotonic, memory, and conduction velocity restitution effects. *Am J Physiol Heart Circ Physiol* 286: H2332-2341, 2004.

36. **Chiang CE and Roden DM.** The long QT syndromes: genetic basis and clinical implications. *J Am Coll Cardiol* 36: 1-12, 2000.

37. **Chudin E, Goldhaber J, Garfinkel A, Weiss J, and Kogan B.** Intracellular Ca(2+) dynamics and the stability of ventricular tachycardia. *Biophys J* 77: 2930-2941, 1999.

38. **Clancy CE and Rudy Y.** Linking a genetic defect to its cellular phenotype in a cardiac arrhythmia. *Nature* 400: 566-569, 1999.

39. **Clancy CE, Tateyama M, Liu H, Wehrens XH, and Kass RS.** Non-equilibrium gating in cardiac Na+ channels: an original mechanism of arrhythmia. *Circulation* 107: 2233-2237, 2003.

40. **CLAYTON RH, BAILEY A, BIKTASHEV VN, and HOLDEN AV.** Re-entrant Cardiac Arrhythmias in Computational Models of Long QT Myocardium. *Journal of Theoretical Biology* 208: 215-225, 2001.

41. **Clayton RH and Holden AV.** Propagation of normal beats and re-entry in a computational model of ventricular cardiac tissue with regional differences in action potential shape and duration. *Prog Biophys Mol Biol* 85: 473-499, 2004.

42. **Colyer J and Wang JH.** Dependence of cardiac sarcoplasmic reticulum calcium pump activity on the phosphorylation status of phospholamban. *J Biol Chem* 266: 17486-17493, 1991.

43. **Conrath CE, Wilders R, Coronel R, de Bakker JMT, Taggart P, de Groot JR, and Opthof T.** Intercellular coupling through gap junctions masks M cells in the human heart. *Cardiovascular Research* 62: 407-414, 2004.

44. **Corbin JD, Sugden PH, Lincoln TM, and Keely SL.** Compartmentalization of adenosine 3':5'-monophosphate and adenosine 3':5'-monophosphate-dependent protein kinase in heart tissue. *J Biol Chem* 252: 3854-3861, 1977.

45. **Cordeiro JM, Greene L, Heilmann C, Antzelevitch D, and Antzelevitch C.** Transmural heterogeneity of calcium activity and mechanical function in the canine left ventricle. *Am J Physiol (Heart Circ Physiol)* 286: H1471-1479, 2004.

46. **Cordeiro JM, Greene L, Heilmann C, Antzelevitch D, and Antzelevitch C.** Transmural heterogeneity of calcium activity and mechanical function in the canine left ventricle. *Am J Physiol Heart Circ Physiol* 286: H1471-1479, 2004.

47. **Cordeiro JM, Spitzer KW, and Giles WR.** Repolarizing K+ currents in rabbit heart Purkinje cells. *J Physiol* 508 ( Pt 3): 811-823, 1998.

48. **de Bakker JM and OptHof T.** Is the apico-basal gradient larger than the transmural gradient? *J Cardiovasc Pharmacol* 39: 328-331, 2002.

49. **Demo SD and Yellen G.** The inactivation gate of the Shaker K+ channel behaves like an open-channel blocker. *Neuron* 7: 743-753, 1991.

50. **Deschenes I, DiSilvestre D, Juang GJ, Wu RC, An WF, and Tomaselli GF.** Regulation of Kv4.3 current by KChIP2 splice variants: a component of native cardiac I(to)? *Circulation* 106: 423-429, 2002.

51. **Deschenes I, Neyroud N, DiSilvestre D, Marban E, Yue DT, and Tomaselli GF.** Isoform-specific modulation of voltage-gated Na(+) channels by calmodulin. *Circ Res* 90: E49-57, 2002.

52. **Dixon JE, Shi W, Wang HS, McDonald C, Yu H, Wymore RS, Cohen IS, and McKinnon D.** Role of the Kv4.3 K+ channel in ventricular muscle. A molecular correlate for the transient outward current. *Circ Res* 79: 659-668, 1996.

53. **Doggrell SA and Brown L.** D-Sotalol: death by the SWORD or deserving of further consideration for clinical use? *Expert Opin Investig Drugs* 9: 1625-1634, 2000.

54. **Drouin E, Charpentier F, Gauthier C, Laurent K, and Le Marec H.** Electrophysiologic characteristics of cells spanning the left ventricular wall of human heart: evidence for presence of M cells. *J Am Coll Cardiol* 26: 185-192, 1995.

55. **Endoh M, Hiramoto T, Ishihata A, Takanashi M, and Inui J.** Myocardial alpha 1-adrenoceptors mediate positive inotropic effect and changes in phosphatidylinositol metabolism. Species differences in receptor distribution and the intracellular coupling process in mammalian ventricular myocardium. *Circ Res* 68: 1179-1190, 1991.

56. **Faber GM and Rudy Y.** Action potential and contractility changes in [Na(+)](i) overloaded cardiac myocytes: a simulation study. *Biophys J* 78: 2392-2404, 2000.

57. **Fitzhugh RA.** Impulses and physiological states in theoretical models of nerve membrane. *Biophysical Journal* 1: 445-466, 1961.

58. **Fox JJ, McHarg JL, and Gilmour RF.** Ionic mechanism of electrical alternans. *American Journal of Physiology-Heart and Circulatory Physiology* 282: H516-H530, 2002.

59. **Gao J, Wang W, Cohen IS, and Mathias RT.** Transmural gradients in na/k pump activity and [Na+]I in canine ventricle. *Biophys J* 89: 1700-1709, 2005.

60. **Geselowitz DB and Miller WT.** A bidomain model for anisotropic cardiac muscle. *Annals of Biomedical Engineering* 11: 191-206, 1983.

61. **Gima K and Rudy Y.** Ionic current basis of electrocardiographic waveforms: a model study. *Circ Res* 90: 889-896, 2002.

62. **Goldhaber JI, Xie LH, Duong T, Motter C, Khuu K, and Weiss JN.** Action potential duration restitution and alternans in rabbit ventricular myocytes: the key role of intracellular calcium cycling. *Circ Res* 96: 459-466, 2005.

63. **Gray RA, Jalife J, Panfilov A, Baxter WT, Cabo C, Davidenko JM, and Pertsov AM.** Nonstationary vortexlike reentrant activity as a mechanism of polymorphic ventricular tachycardia in the isolated rabbit heart. *Circulation* 91: 2454-2469, 1995.

64. **Greenstein JL, Hinch R, and Winslow RL.** Mechanisms of excitation-contraction coupling in an integrative model of the cardiac ventricular myocyte. *Biophys J*, 2005.

65. **Greenstein JL, Hinch R, and Winslow RL.** Mechanisms of excitation-contraction coupling in an integrative model of the cardiac ventricular myocyte. *Biophys J* 90: 77-91, 2006.

66. **Greenstein JL and Winslow RL.** An integrative model of the cardiac ventricular myocyte incorporating local control of Ca2+ release. *Biophys J* 83: 2918-2945, 2002.

67. **Greenstein JL, Wu R, Po S, Tomaselli GF, and Winslow RL.** Role of the calcium-independent transient outward current I(to1) in shaping action potential morphology and duration. *Circ Res* 87: 1026-1033, 2000.

68. **Guo W, Malin SA, Johns DC, Jeromin A, and Nerbonne JM.** Modulation of Kv4-encoded K(+) currents in the mammalian myocardium by neuronal calcium sensor-1. *J Biol Chem* 277: 26436-26443, 2002.

69. **Guth L.** Regeneration in the mammalian peripheral nervous system. *Physiol Rev* 36: 441-478, 1956.

70. **Han J, Garciadejalon P, and Moe GK.** Adrenergic Effects on Ventricular Vulnerability. *Circ Res* 14: 516-524, 1964.

71. **Han J and Moe GK.** Nonuniform Recovery of Excitability in Ventricular Muscle. *Circ Res* 14: 44-60, 1964.

72. **Healy SN and McCulloch AD.** An ionic model of stretch-activated and stretch-modulated currents in rabbit ventricular myocytes. *Europace* 7: S128-S134, 2005.

73. **Helm P, Beg MF, Miller MI, and Winslow RL.** Measuring and Mapping Cardiac Fiber and Laminar Architecture Using Diffusion Tensor MR Imaging. *Annals of the New York Academy of Sciences* 1047: 296-307, 2005.

74. **Henriquez CS.** Simulating the Electrical Behavior of Cardiac Tissue Using the Bidomain Model. *Critical Reviews in Biomedical Engineering* 21: 1-77, 1993.

75. **Hinch R, Greenstein JL, Tanskanen AJ, Xu L, and Winslow RL.** A simplified local control model of calcium-induced calcium release in cardiac ventricular myocytes. *Biophys J* 87: 3723-3736, 2004.

76. **Hodgkin AL and Huxley AF.** A quantitative description of membrane current and its application to conduction and excitation in nerve. *Journal of Physiology* 117: 500-544, 1952.

77. **Hoyt RH, Cohen ML, and Saffitz JE.** Distribution and three-dimensional structure of intercellular junctions in canine myocardium. *Circ Res* 64: 563-574, 1989.

78. **Hume JR, Duan D, Collier ML, Yamazaki J, and Horowitz B.** Anion transport in heart. *Physiol Rev* 80: 31-81, 2000.

79. **Iyer V, Mazhari R, and Winslow RL.** A computational model of the human left-ventricular epicardial myocyte. *Biophys J* 87: 1507-1525, 2004.

80. **Jafri MS, Rice JJ, and Winslow RL.** Cardiac Ca2+ dynamics: The roles of ryanodine receptor adaptation and sarcoplasmic reticulum load. *Biophysical Journal* 74: 1149-1168, 1998.

81. **James AF, Tominaga T, Okada Y, and Tominaga M.** Distribution of cAMP-activated chloride current and CFTR mRNA in the guinea pig heart. *Circ Res* 79: 201-207, 1996.

82. **Jurkiewicz NK and Sanguinetti MC.** Rate-dependent prolongation of cardiac action potentials by a methanesulfonanilide class III antiarrhythmic agent. Specific block of rapidly activating delayed rectifier K+ current by dofetilide. *Circ Res* 72: 75-83, 1993.

83. **Kaab S, Dixon J, Duc J, Ashen D, Nabauer M, Beuckelmann DJ, Steinbeck G, McKinnon D, and Tomaselli GF.** Molecular basis of transient outward potassium current downregulation in human heart failure: a decrease in Kv4.3 mRNA correlates with a reduction in current density. *Circulation* 98: 1383-1393, 1998.

84. **Kass RS and Moss AJ.** Long QT syndrome: novel insights into the mechanisms of cardiac arrhythmias. *J Clin Invest* 112: 810-815, 2003.

85. **Katra RP and Laurita KR.** Cellular mechanism of calcium-mediated triggered activity in the heart. *Circ Res* 96: 535-542, 2005.

86. **Kerckhoffs RCP, Bovendeerd PHM, Prinzen FW, Smits K, and Arts T.** Intra- and interventricular asynchrony of electromechanics in the ventricularly paced heart. *Journal of Engineering Mathematics* 47: 201-216, 2003.

87. **Kerckhoffs RCP, Faris O, Bovendeerd PHM, Prinzen FW, Smits K, McVeigh ER, and Arts T.** Electromechanics of paced left ventricle simulated by straightforward mathematical model: comparison with experiments. *American Journal of Physiology-Heart and Circulatory Physiology* 289: H1889–H1897, 2005.

88. **Kettlewell S, Walker NL, Cobbe SM, Burton FL, and Smith GL.** The electrophysiological and mechanical effects of 2,3-butane-dione monoxime and cytochalasin-D in the Langendorff perfused rabbit heart. *Exp Physiol* 89: 163-172, 2004.

89. **Kop WJ, Krantz DS, Nearing BD, Gottdiener JS, Quigley JF, O'Callahan M, DelNegro AA, Friehling TD, Karasik P, Suchday S, Levine J, and Verrier RL.** Effects of acute mental stress and exercise on T-wave alternans in patients with implantable cardioverter defibrillators and controls. *Circulation* 109: 1864-1869, 2004.

90. **Kuo HC, Cheng CF, Clark RB, Lin JJ, Lin JL, Hoshijima M, Nguyen-Tran VT, Gu Y, Ikeda Y, Chu PH, Ross J, Giles WR, and Chien KR.** A defect in the Kv channel-interacting protein 2 (KChIP2) gene leads to a complete loss of I(to) and confers susceptibility to ventricular tachycardia. *Cell* 107: 801-813, 2001.

91. **Lampert R, Shusterman V, Burg MM, Lee FA, Earley C, Goldberg A, McPherson CA, Batsford WP, and Soufer R.** Effects of psychologic stress on repolarization and relationship to autonomic and hemodynamic factors. *J Cardiovasc Electrophysiol* 16: 372-377, 2005.

92. **Langtangen HP.** *Computational Partial Differential Equations*: Springer, 2003.

93. **Laurita KR, Katra R, Wible B, Wan X, and Koo MH.** Transmural heterogeneity of calcium handling in canine. *Circ Res* 92: 668-675, 2003.

94. **Laurita KR and Katra RP.** Delayed after depolarization-mediated triggered activity associated with slow calcium sequestration near the endocardium. *J Cardiovasc Electrophysiol* 16: 418-424, 2005.

95. **Leenhardt A, Lucet V, Denjoy I, Grau F, Ngoc DD, and Coumel P.** Catecholaminergic polymorphic ventricular tachycardia in children. A 7-year follow-up of 21 patients. *Circulation* 91: 1512-1519, 1995.

96. **Legrice IJ, Hunter PJ, and Smaill BH.** Laminar structure of the heart: a mathematical model. *Am J Physiol Heart Circ Physiol* 272: H2466-2476, 1997.

97. **LeGrice IJ, Hunter PJ, and Smaill BH.** Laminar structure of the heart: A mathematical model. *American Journal of Physiology-Heart and Circulatory Physiology* 41: H2466-H2476, 1997.

98. **Legrice IJ, Smaill BH, Chai LZ, Edgar SG, Gavin JB, and Hunter PJ.** Laminar Structure of the Heart - Ventricular Myocyte Arrangement and Connective-Tissue Architecture in the Dog. *American Journal of Physiology-Heart and Circulatory Physiology* 38: H571-H582, 1995.

99. **LeGrice IJ, Smaill BH, Chai LZ, Edgar SG, Gavin JB, and Hunter PJ.** Laminar structure of the heart: ventricular myocyte arrangement and connective tissue architecture in the dog. *Am J Physiol* 269: H571-582, 1995.

100. **LeGrice IJ, Smaill BH, Chai LZ, Edgar SG, Gavin JB, and Hunter PJ.** Laminar structure of the heart: ventricular myocyte arrangement and connective tissue architecture in the dog. *Am J Physiol* 269: H571-582, 1995.

101. **Leon LJ and Horacek BM.** Computer-Model of Excitation and Recovery in the Anisotropic Myocardium .3. Arrhythmogenic Conditions in the Simplified Left-Ventricle. *Journal of Electrocardiology* 24: 33-41, 1991.

102. **Leroy SS and Russell M.** Long QT syndrome and other repolarization-related dysrhythmias. *AACN Clin Issues* 15: 419-431, 2004.

103. **Levi-Montalcini R.** The Nerve Growth Factor. *Ann N Y Acad Sci* 118: 149-170, 1964.

104. **Li GR, Feng J, Yue L, and Carrier M.** Transmural heterogeneity of action potentials and Ito1 in myocytes isolated from the human right ventricle. *Am J Physiol* 275: H369-377, 1998.

105. **Li GR, Feng JL, Carrier M, and Nattel S.** Transmural Electrophysiologic Heterogeneity in the Human Ventricle. *Circulation* 92: 750-750, 1995.

106. **Li XYS and Demmel JW.** SuperLU_DIST: A scalable distributed-memory sparse direct solver for unsymmetric linear systems. *Acm T Math Software* 29: 110-140, 2003.

107. **Linz KW and Meyer R.** Control of L-type calcium current during the action potential of guinea-pig ventricular myocytes. *J Physiol* 513 ( Pt 2): 425-442, 1998.

108. **Litovsky SH and Antzelevitch C.** Rate dependence of action potential duration and refractoriness in canine ventricular endocardium differs from that of epicardium: role of the transient outward current. *J Am Coll Cardiol* 14: 1053-1066, 1989.

109. **Liu D-W and Antzelevitch C.** Characteristics of the delayed rectifier current (IKr and IKs) in canine ventricular epicardial, midmyocardial, and endocardial myocytes : A weaker IKs contributes to the longer action potential of the M cell. *Circ Res* 76: 351-365, 1995.

110. **Liu DW, Gintant GA, and Antzelevitch C.** Ionic bases for electrophysiological distinctions among epicardial, midmyocardial, and endocardial myocytes from the free wall of the canine left ventricle. *Circ Res* 72: 671-687, 1993.

111. **Liu J and Laurita KR.** The mechanism of pause-induced torsade de pointes in long QT syndrome. *J Cardiovasc Electrophysiol* 16: 981-987, 2005.

112. **Lu HR, Vlaminckx E, Van De Water A, and Gallacher DJ.** Both beta-adrenergic receptor stimulation and cardiac tissue type have important roles in elucidating the functional effects of I(Ks) channel blockers in vitro. *J Pharmacol Toxicol Methods* 51: 81-90, 2005.

113. **Luo CH and Rudy Y.** A Dynamic-Model of the Cardiac Ventricular Action-Potential .1. Simulations of Ionic Currents and Concentration Changes. *Circulation Research* 74: 1071-1096, 1994.

114. **Luo C-H and Rudy Y.** A dynamic model of the cardiac ventricular action potential I. Simulations of ionic currents and concentration changes. *Circ Res*: 1071-1096, 1994.

115. **Magnano AR, Holleran S, Ramakrishnan R, Reiffel JA, and Bloomfield DM.** Autonomic modulation of the u wave during sympathomimetic stimulation and vagal inhibition in normal individuals. *Pacing Clin Electrophysiol* 27: 1484-1492, 2004.

116. **Magnano AR, Holleran S, Ramakrishnan R, Reiffel JA, and Bloomfield DM.** Autonomic nervous system influences on QT interval in normal subjects. *J Am Coll Cardiol* 39: 1820-1826, 2002.

117. **Maltsev VA and Undrovinas AI.** A multi-modal composition of the late Na+ current in human ventricular cardiomyocytes. *Cardiovasc Res* 69: 116-127, 2006.

118. **Marban E, Robinson SW, and Wier WG.** Mechanisms of arrhythmogenic delayed and early afterdepolarizations in ferret ventricular muscle. *J Clin Invest* 78: 1185-1192, 1986.

119. **Marx SO, Kurokawa J, Reiken S, Motoike H, D'Armiento J, Marks AR, and Kass RS.** Requirement of a macromolecular signaling complex for beta adrenergic receptor modulation of the KCNQ1-KCNE1 potassium channel. *Science* 295: 496-499, 2002.

120. **Mazhari R, Nuss HB, Armoundas AA, Winslow RL, and Marban E.** Ectopic expression of KCNE3 accelerates cardiac repolarization and abbreviates the QT interval. *J Clin Invest* 109: 1083-1090, 2002.

121. **McConville P, Spencer RG, and Lakatta EG.** Temporal dynamics of inotropic, chronotropic and metabolic responses during {beta}1- and {beta}2-adrenergic receptor stimulation in the isolated, perfused rat heart. *Am J Physiol Endocrinol Metab*, 2005.

122. **McCulloch AD.** Functionally and structurally integrated computational modeling of ventricular physiology. *Japanese Journal of Physiology* 54: 531-539, 2004.

123. **McIntosh MA, Cobbe SM, Kane KA, and Rankin AC.** Action potential prolongation and potassium currents in left-ventricular myocytes isolated from hypertrophied rabbit hearts. *J Mol Cell Cardiol* 30: 43-53, 1998.

124. **McIntosh MA, Cobbe SM, and Smith GL.** Heterogeneous changes in action potential and intracellular Ca2+ in left ventricular myocyte sub-types from rabbits with heart failure. *Cardiovasc Res* 45: 397-409, 2000.

125. **Michailova A and McCulloch A.** Model study of ATP and ADP buffering, transport of Ca(2+) and Mg(2+), and regulation of ion pumps in ventricular myocyte. *Biophys J* 81: 614-629, 2001.

126. **Moak JP, Reder RF, Danilo P, Jr., and Rosen MR.** Developmental changes in the interactions of cholinergic and beta-adrenergic agonists on electrophysiologic properties of canine cardiac Purkinje fibers. *Pediatr Res* 20: 613-618, 1986.

127. **Movsesian MA, Komas N, Krall J, and Manganiello VC.** Expression and activity of low Km, cGMP-inhibited cAMP phosphodiesterase in cardiac and skeletal muscle. *Biochem Biophys Res Commun* 225: 1058-1062, 1996.

128. **Mullerborer BJ, Erdman DJ, and Buchanan JW.** Electrical Coupling and Impulse Propagation in Anatomically Modeled Ventricular Tissue. *Ieee Transactions on Biomedical Engineering* 41: 445-454, 1994.

129. **Nabauer M, Beuckelmann DJ, Uberfuhr P, and Steinbeck G.** Regional Differences in Current Density and Rate-Dependent Properties of the Transient Outward Current in Subepicardial and Subendocardial Myocytes of Human Left Ventricle. *Circulation* 93: 168-177, 1996.

130. **Nabauer M, Beuckelmann DJ, Uberfuhr P, and Steinbeck G.** Regional differences in current density and rate-dependent properties of the transient outward current in subepicardial and subendocardial myocytes of human left ventricle. *Circulation* 93: 168-177, 1996.

131. **Nadal MS, Ozaita A, Amarillo Y, Vega-Saenz de Miera E, Ma Y, Mo W, Goldberg EM, Misumi Y, Ikehara Y, Neubert TA, and Rudy B.** The CD26-related dipeptidyl aminopeptidase-like protein DPPX is a critical component of neuronal A-type K+ channels. *Neuron* 37: 449-461, 2003.

132. **Nakamura TY, Pountney DJ, Ozaita A, Nandi S, Ueda S, Rudy B, and Coetzee WA.** A role for frequenin, a Ca2+-binding protein, as a regulator of Kv4 K+-currents. *Proc Natl Acad Sci U S A* 98: 12808-12813, 2001.

133. **Nam GB, Burashnikov A, and Antzelevitch C.** Cellular mechanisms underlying the development of catecholaminergic ventricular tachycardia. *Circulation* 111: 2727-2733, 2005.

134. **Narayan SM, Smith JM, Lindsay BD, Cain ME, and Davila-Roman VG.** Relation of T-wave alternans to regional left ventricular dysfunction and eccentric hypertrophy secondary to coronary heart disease. *Am J Cardiol* 97: 775-780, 2006.

135. **Nash MP, Thornton JM, Sears CE, Varghese A, O'Neill M, and Paterson DJ.** Ventricular activation during sympathetic imbalance and its computational reconstruction. *J Appl Physiol* 90: 287-298, 2001.

136. **Nerbonne JM and Kass RS.** Molecular physiology of cardiac repolarization. *Physiol Rev* 85: 1205-1253, 2005.

137. **Nickerson DP, Smith N, and Hunter P.** New developments in a strongly coupled cardiac electromechanical model. *Europace* 7: 5118-5127, 2005.

138. **Nielsen PM, Le Grice IJ, Smaill BH, and Hunter PJ.** Mathematical model of geometry and fibrous structure of the heart. *Am J Physiol* 260: H1365-1378, 1991.

139. **Nielsen PMF, Legrice IJ, Smaill BH, and Hunter PJ.** Mathematical-Model of Geometry and Fibrous Structure of the Heart. *American Journal of Physiology* 260: H1365-H1378, 1991.

140. **Noble D and Rudy Y.** Models of cardiac ventricular action potentials: iterative interaction between experiment and simulation. *Philosophical Transactions of the Royal Society of London Series a-Mathematical Physical and Engineering Sciences* 359: 1127-1142, 2001.

141. **Noble D, Varghese A, Kohl P, and Noble P.** Improved guinea-pig ventricular cell model incorporating a diadic space, IKr and IKs, and length- and tension-dependent processes. *Can J Cardiol* 14: 123-134, 1998.

142. **Nolasco JB and Dahlen RW.** A graphic method for the study of alternation in cardiac action potentials. *J Appl Physiol* 25: 191-196, 1968.

143. **Pandit SV, Clark RB, Giles WR, and Demir SS.** A mathematical model of action potential heterogeneity in adult rat left ventricular myocytes. *Biophysical Journal* 81: 3029-3051, 2001.

144. **Panfilov AV.** Modeling of re-entrant patterns in an anatomical model of the heart. In: *Computational biology of the heart*, edited by Panfilov AV and Holden AV. Chichester, UK: Wiley, 1997.

145. **Patel SP and Campbell DL.** Transient outward potassium current, 'Ito', phenotypes in the mammalian left ventricle: underlying molecular, cellular and biophysical mechanisms. *J Physiol* 569: 7-39, 2005.

146. **Patel SP, Campbell DL, Morales MJ, and Strauss HC.** Heterogeneous expression of KChIP2 isoforms in the ferret heart. *J Physiol* 539: 649-656, 2002.

147. **Patel SP, Campbell DL, and Strauss HC.** Elucidating KChIP effects on Kv4.3 inactivation and recovery kinetics with a minimal KChIP2 isoform. *J Physiol* 545: 5-11, 2002.

148. **Patel SP, Parai R, and Campbell DL.** Regulation of Kv4.3 voltage-dependent gating kinetics by KChIP2 isoforms. *J Physiol* 557: 19-41, 2004.

149. **Peterson BZ, DeMaria CD, Adelman JP, and Yue DT.** Calmodulin is the Ca2+ sensor for Ca2+ -dependent inactivation of L-type calcium channels. *Neuron* 22: 549-558, 1999.

150. **Pham Q, Quan KJ, and Rosenbaum DS.** T-wave alternans: marker, mechanism, and methodology for predicting sudden cardiac death. *J Electrocardiol* 36 Suppl: 75-81, 2003.

151. **Poelzing S, Akar FG, Baron E, and Rosenbaum DS.** Heterogeneous connexin43 expression produces electrophysiological heterogeneities across ventricular wall. *Am J Physiol Heart Circ Physiol* 286: H2001-2009, 2004.

152. **Pollard AE and Bar RC.** Computer simulations of activation in an anatomical based model of the human ventricular conduction system. *IEEE Transactions on Biomedical Engineering* 38: 982-986, 1991.

153. **Pool R.** Heart like a wheel. *Science* 247: 1294-1295, 1990.

154. **Postma AV, Denjoy I, Hoorntje TM, Lupoglazoff JM, Da Costa A, Sebillon P, Mannens MM, Wilde AA, and Guicheney P.** Absence of calsequestrin 2 causes severe forms of catecholaminergic polymorphic ventricular tachycardia. *Circ Res* 91: e21-26, 2002.

155. **Priebe L and Beuckelmann DJ.** Simulation study of cellular electric properties in heart failure. *Circ Res* 82: 1206-1223, 1998.

156. **Priebe L and Beuckelmann DJ.** Simulation study of cellular electric properties in heart failure. *Circulation Research* 82: 1206-1223, 1998.

157. **Priori SG and Corr PB.** Mechanisms underlying early and delayed afterdepolarizations induced by catecholamines. *Am J Physiol* 258: H1796-1805, 1990.

158. **Priori SG, Napolitano C, Memmi M, Colombi B, Drago F, Gasparini M, DeSimone L, Coltorti F, Bloise R, Keegan R, Cruz Filho FE, Vignati G, Benatar A, and DeLogu A.** Clinical and molecular characterization of patients with catecholaminergic polymorphic ventricular tachycardia. *Circulation* 106: 69-74, 2002.

159. **Puglisi JL and Bers DM.** LabHEART: an interactive computer model of rabbit ventricular myocyte ion channels and Ca transport. *Am J Physiol Cell Physiol* 281: C2049-2060, 2001.

160. **Puglisi JL and Bers DM.** LabHEART: an interactive computer model of rabbit ventricular myocyte ion channels and Ca transport. *American Journal of Physiology-Cell Physiology* 281: C2049-C2060, 2001.

161. **Qu Z and Garfinkel A.** An advanced algorithm for solving partial differential equation in cardiac conduction. *IEEE Trans Biomed Eng* 46: 1166-1168, 1999.

162. **Reese TG, Weisskoff RM, Smith RN, Rosen BR, Dinsmore RE, and Wedeen VJ.** Imaging Myocardial Fiber Architecture in-Vivo with Magnetic-Resonance. *Magnetic Resonance in Medicine* 34: 786-791, 1995.

163. **Ren X, Shand SH, and Takimoto K.** Effective association of Kv channel-interacting proteins with Kv4 channel is mediated with their unique core peptide. *J Biol Chem* 278: 43564-43570, 2003.

164. **Rice JJ, Jafri MS, and Winslow RL.** Modeling gain and gradedness of Ca2+ release in the functional unit of the cardiac diadic space. *Biophys J* 77: 1871-1884, 1999.

165. **Rijcken J, Bovendeerd PHM, Schoofs AJG, van Campen DH, and Arts T.** Optimization of cardiac fiber orientation for homogeneous fiber strain during ejection. *Annals of Biomedical Engineering* 27: 289-297, 1999.

166. **Rivolta I, Clancy CE, Tateyama M, Liu H, Priori SG, and Kass RS.** A novel SCN5A mutation associated with long QT-3: altered inactivation kinetics and channel dysfunction. *Physiol Genomics* 10: 191-197, 2002.

167. **Roberts R.** Genomics and cardiac arrhythmias. *J Am Coll Cardiol* 47: 9-21, 2006.

168. **Roden DM, Lazzara R, Rosen M, Schwartz PJ, Towbin J, and Vincent GM.** Multiple mechanisms in the long-QT syndrome. Current knowledge, gaps, and future directions. The SADS Foundation Task Force on LQTS. *Circulation* 94: 1996-2012, 1996.

169. **Roden DM, Lazzara R, Rosen M, Schwartz PJ, Towbin J, and Vincent GM.** Multiple Mechanisms in the Long-QT Syndrome: Current Knowledge, Gaps, and Future Directions. *Circulation* 94: 1996-2012, 1996.

170. **Rodriguez B, Eason JC, and Trayanova N.** Differences between left and right ventricular anatomy determine the types of reentrant circuits induced by an external electric shock. A rabbit heart simulation study. *Progress in Biophysics & Molecular Biology*: Epub ahead of print, 2005.

171. **Rodriguez B, Li L, Eason JC, Efimov IR, and Trayanova NA.** Differences between left and right ventricular chamber geometry affect cardiac vulnerability to electric shocks. *Circulation Research* 97: 168-175, 2005.

172. **Rogers JM MA.** A collocation--Galerkin finite element model of cardiac action potential propagation. *IEEE Trans Biomed Eng* 41: 743-757, 1994.

173. **Rogers JM and McCulloch AD.** A collocation--Galerkin finite element model of cardiac action potential propagation. *IEEE Trans Biomed Eng* 41: 743-757, 1994.

174. **Rosati B, Pan Z, Lypen S, Wang HS, Cohen I, Dixon JE, and McKinnon D.** Regulation of KChIP2 potassium channel beta subunit gene expression underlies the gradient of transient outward current in canine and human ventricle. *J Physiol* 533: 119-125, 2001.

175. **Rosenbaum DS, Jackson LE, Smith JM, Garan H, Ruskin JN, and Cohen RJ.** Electrical alternans and vulnerability to ventricular arrhythmias. *N Engl J Med* 330: 235-241, 1994.

176. **Ross AA and Streeter DD, Jr.** Myocardial fiber disarray. *Circulation* 60: 1425-1426, 1979.

177. **Rossow CF, Dilly KW, and Santana LF.** Differential Calcineurin/NFATc3 Activity Contributes to the Ito Transmural Gradient in the Mouse Heart. *Circ Res*, 2006.

178. **Ruppersberg JP, Frank R, Pongs O, and Stocker M.** Cloned neuronal IK(A) channels reopen during recovery from inactivation. *Nature* 353: 657-660, 1991.

179. **Saint DA, Ju YK, and Gage PW.** A persistent sodium current in rat ventricular myocytes. *J Physiol* 453: 219-231, 1992.

180. **Sakmann BF, Spindler AJ, Bryant SM, Linz KW, and Noble D.** Distribution of a persistent sodium current across the ventricular wall in guinea pigs. *Circ Res* 87: 910-914, 2000.

181. **Salata JJ and Wasserstrom JA.** Effects of quinidine on action potentials and ionic currents in isolated canine ventricular myocytes. *Circ Res* 62: 324-337, 1988.

182. **Sampson KJ and Henriquez CS.** Electrotonic influences on action potential duration dispersion in small hearts: a simulation study. *Am J Physiol Heart Circ Physiol* 289: H350-360, 2005.

183. **Sampson KJ and Henriquez CS.** Electrotonic influences on action potential duration dispersion in small hearts: a simulation study. *American Journal of Physiology-Heart and Circulatory Physiology* 289: H350-H360, 2005.

184. **Sampson KJ and Henriquez CS.** Simulation and prediction of functional block in the presence of structural and ionic heterogeneity. *Am J Physiol Heart Circ Physiol* 281: H2597-2603, 2001.

185. **Sanguinetti MC and Jurkiewicz NK.** Two components of cardiac delayed rectifier K+ current. Differential sensitivity to block by class III antiarrhythmic agents. *J Gen Physiol* 96: 195-215, 1990.

186. **Sarkozy A and Brugada P.** Sudden cardiac death and inherited arrhythmia syndromes. *J Cardiovasc Electrophysiol* 16 Suppl 1: S8-20, 2005.

187. **Saucerman JJ, Brunton LL, Michailova AP, and McCulloch AD.** Modeling beta-adrenergic control of cardiac myocyte contractility in silico. *J Biol Chem* 278: 47997-48003, 2003.

188. **Saucerman JJ, Brunton LL, Michailova AP, and McCulloch AD.** Modeling beta-adrenergic control of cardiac myocyte contractility in silico. *J Biol Chem* 278: 47997-48003, 2003.

189. **Saucerman JJ, Healy SN, Belik ME, Puglisi JL, and McCulloch AD.** Proarrhythmic Consequences of a KCNQ1 AKAP-Binding Domain Mutation: Computational Models of Whole Cells and Heterogeneous Tissue. *Circ Res* 95: 1216-1224, 2004.

190. **Saucerman JJ and McCulloch AD.** Mechanistic systems models of cell signaling networks: a case study of myocyte adrenergic regulation. *Prog Biophys Mol Biol* 85: 261-278, 2004.

191. **Saucerman JJ, Zhang J, Martin JM, X PL, E SA, Y TR, and D MA.** Systems analysis of PKA-mediated phosphorylation gradients in live cardiac myocytes. *submitted to PNAS, 2006*.

192. **Schwaiblmair M, von Scheidt W, Uberfuhr P, Ziegler S, Schwaiger M, Reichart B, and Vogelmeier C.** Functional significance of cardiac reinnervation in heart transplant recipients. *J Heart Lung Transplant* 18: 838-845, 1999.

193. **Schwartz PJ, Priori SG, Spazzolini C, Moss AJ, Vincent GM, Napolitano C, Denjoy I, Guicheney P, Breithardt G, Keating MT, Towbin JA, Beggs AH, Brink P, Wilde AA, Toivonen L, Zareba W, Robinson JL, Timothy KW, Corfield V, Wattanasirichaigoon D, Corbett C, Haverkamp W, Schulze-Bahr E, Lehmann MH, Schwartz K, Coumel P, and Bloise R.** Genotype-phenotype correlation in the long-QT syndrome: gene-specific triggers for life-threatening arrhythmias. *Circulation* 103: 89-95, 2001.

194. **Schwartz PJ, Priori SG, Spazzolini C, Moss AJ, Vincent GM, Napolitano C, Denjoy I, Guicheney P, Breithardt G, Keating MT, Towbin JA, Beggs AH, Brink P, Wilde AA, Toivonen L, Zareba W, Robinson JL, Timothy KW, Corfield V, Wattanasirichaigoon D, Corbett C, Haverkamp W, Schulze-Bahr E, Lehmann MH, Schwartz K, Coumel P, and Bloise R.** Genotype-phenotype correlation in the long-QT syndrome: gene-specific triggers for life-threatening arrhythmias. *Circulation* 103: 89-95, 2001.

195. **Schwartz PJ, Priori SG, Spazzolini C, Moss AJ, Vincent GM, Napolitano C, Denjoy I, Guicheney P, Breithardt G, Keating MT, Towbin JA, Beggs AH, Brink P, Wilde AAM, Toivonen L, Zareba W, Robinson JL, Timothy KW, Corfield V, Wattanasirichaigoon D, Corbett C, Haverkamp W, Schulze-Bahr E, Lehmann MH, Schwartz K, Coumel P, and Bloise R.** Genotype-Phenotype Correlation in the Long-QT Syndrome : Gene-Specific Triggers for Life-Threatening Arrhythmias. *Circulation* 103: 89-95, 2001.

196. **Scollan DF, Holmes A, Winslow R, and Forder J.** Histological validation of myocardial microstructure obtained from diffusion tensor magnetic resonance imaging. *American Journal of Physiology-Heart and Circulatory Physiology* 44: H2308-H2318, 1998.

197. **Seemann G, Sachse FB, Weiss DL, and Dossel O.** Quantitative reconstruction of cardiac electromechanics in human myocardium: Regional heterogeneity. *Journal of Cardiovascular Electrophysiology* 14: S219-S228, 2003.

198. **Shakur Y, Fong M, Hensley J, Cone J, Movsesian MA, Kambayashi J, Yoshitake M, and Liu Y.** Comparison of the effects of cilostazol and milrinone on cAMP-PDE activity, intracellular cAMP and calcium in the heart. *Cardiovasc Drugs Ther* 16: 417-427, 2002.

199. **Shamgar L, Ma L, Schmitt N, Haitin Y, Peretz A, Wiener R, Hirsch J, Pongs O, and Attali B.** Calmodulin is essential for cardiac IKS channel gating and assembly: impaired function in long-QT mutations. *Circ Res* 98: 1055-1063, 2006.

200. **Shannon TR, Ginsburg KS, and Bers DM.** Reverse mode of the sarcoplasmic reticulum calcium pump and load-dependent cytosolic calcium decline in voltage-clamped cardiac ventricular myocytes. *Biophys J* 78: 322-333, 2000.

201. **Shiferaw Y, Watanabe MA, Garfinkel A, Weiss JN, and Karma A.** Model of intracellular calcium cycling in ventricular myocytes. *Biophys J* 85: 3666-3686, 2003.

202. **Shimizu W and Antzelevitch C.** Differential effects of beta-adrenergic agonists and antagonists in LQT1, LQT2 and LQT3 models of the long QT syndrome. *J Am Coll Cardiol* 35: 778-786, 2000.

203. **Shusterman V, Beigel A, Shah SI, Aysin B, Weiss R, Gottipaty VK, Schwartzman D, and Anderson KP.** Changes in autonomic activity and ventricular repolarization. *J Electrocardiol* 32 Suppl: 185-192, 1999.

204. **Sicouri S and Antzelevitch C.** A subpopulation of cells with unique electrophysiological properties in the deep subepicardium of the canine ventricle. The M cell. *Circ Res* 68: 1729-1741, 1991.

205. **Silva J and Rudy Y.** Subunit interaction determines IKs participation in cardiac repolarization and repolarization reserve. *Circulation* 112: 1384-1391, 2005.

206. **Smith JM, Clancy EA, Valeri CR, Ruskin JN, and Cohen RJ.** Electrical alternans and cardiac electrical instability. *Circulation* 77: 110-121, 1988.

207. **Soeller C and Cannell MB.** Numerical simulation of local calcium movements during L-type calcium channel gating in the cardiac diad. *Biophys J* 73: 97-111, 1997.

208. **Somani P, Guse P, Toscano P, and Bassett AL.** Myocardial transmembrane potentials and adrenergic receptors. *Adv Myocardiol* 1: 189-207, 1980.

209. **Spitzer KW, Pollard AE, Yang L, Zaniboni M, Cordeiro JM, and Huelsing DJ.** Cell-to-Cell Electrical Interactions During Early and Late Repolarization. *J Cardiovasc Electrophysiol* 17 Suppl 1: S8-S14, 2006.

210. **Stengl M, Volders PG, Thomsen MB, Spatjens RL, Sipido KR, and Vos MA.** Accumulation of slowly activating delayed rectifier potassium current (IKs) in canine ventricular myocytes. *J Physiol* 551: 777-786, 2003.

211. **Stern MD.** Theory of excitation-contraction coupling in cardiac muscle. *Biophys J* 63: 497-517, 1992.

212. **Stevens C and Hunter PJ.** Sarcomere length changes in a 3D mathematical model of the pig ventricles. *Progress in Biophysics & Molecular Biology* 82: 229-241, 2003.

213. **Stinstra JG, Shome S, Hopenfeld B, and MacLeod RS.** Modelling passive cardiac conductivity during ischaemia. *Med Biol Eng Comput* 43: 776-782, 2005.

214. **Sundnes J, Lines GT, Mardal KA, and Tveito A.** Multigrid block preconditioning for a coupled system of partial differential equations modeling the electrical activity in the heart. *Comput Methods Biomech Biomed Engin* 5: 397-409, 2002.

215. **Sung D, Mills RW, Schettler J, Narayan SM, Omens JH, and McCulloch AD.** Ventricular filling slows epicardial conduction and increases action potential duration in an optical mapping study of the isolated rabbit heart. *J Cardiovasc Electrophysiol* 14: 739-749, 2003.

216. **Surawicz B.** U wave: facts, hypotheses, misconceptions, and misnomers. *J Cardiovasc Electrophysiol* 9: 1117-1128, 1998.

217. **Szentadrassy N, Banyasz T, Biro T, Szabo G, Toth BI, Magyar J, Lazar J, Varro A, Kovacs L, and Nanasi PP.** Apico-basal inhomogeneity in distribution of ion channels in canine and human ventricular myocardium. *Cardiovasc Res* 65: 851-860, 2005.

218. **Taggart P, Sutton P, Chalabi Z, Boyett MR, Simon R, Elliott D, and Gill JS.** Effect of adrenergic stimulation on action potential duration restitution in humans. *Circulation* 107: 285-289, 2003.

219. **Taggart P, Sutton P, Opthof T, Coronel R, and Kallis P.** Electrotonic cancellation of transmural electrical gradients in the left ventricle in man. *Progress in Biophysics and Molecular Biology* 82: 243-254, 2003.

220. **Taggart P, Sutton P, Opthof T, Coronel R, and Kallis P.** Electrotonic cancellation of transmural electrical gradients in the left ventricle in man. *Progress in Biophysics & Molecular Biology* 82: 243-254, 2003.

221. **Takano M and Noma A.** Distribution of the isoprenaline-induced chloride current in rabbit heart. *Pflugers Arch* 420: 223-226, 1992.

222. **Tan HL, Hou CJY, Lauer MR, and Sung RJ.** Electrophysiologic Mechanisms of the Long QT Interval Syndromes and Torsade de Pointes. *Ann Intern Med* 122: 701-714, 1995.

223. **Tan HL, Kupershmidt S, Zhang R, Stepanovic S, Roden DM, Wilde AA, Anderson ME, and Balser JR.** A calcium sensor in the sodium channel modulates cardiac excitability. *Nature* 415: 442-447, 2002.

224. **Tateyama M, Kurokawa J, Terrenoire C, Rivolta I, and Kass RS.** Stimulation of protein kinase C inhibits bursting in disease-linked mutant human cardiac sodium channels. *Circulation* 107: 3216-3222, 2003.

225. **Tateyama M, Rivolta I, Clancy CE, and Kass RS.** Modulation of cardiac sodium channel gating by protein kinase A can be altered by disease-linked mutation. *J Biol Chem* 278: 46718-46726, 2003.

226. **ten Tusscher KHWJ, Noble D, Noble PJ, and Panfilov AV.** A model for human ventricular tissue. *American Journal of Physiology-Heart and Circulatory Physiology* 286: H1573-H1589, 2004.

227. **Tranquillo JV, Hlavacek J, and Henriquez CS.** An integrative model of mouse cardiac electrophysiology from cell to torso. *Europace* 7 Suppl: 56-70, 2005.

228. **Trayanova N.** Discrete versus syncytial tissue behavior ina model of cardiac stimulation .1. Mathematical formulation. *Ieee Transactions on Biomedical Engineering* 43: 1129-1140, 1996.

229. **Trew M, Le Grice I, Smaill B, and Pullan A.** A finite volume method for modeling discontinuous electrical activation in cardiac tissue. *Ann Biomed Eng* 33: 590-602, 2005.

230. **Undrovinas AI, Maltsev VA, and Sabbah HN.** Repolarization abnormalities in cardiomyocytes of dogs with chronic heart failure: role of sustained inward current. *Cell Mol Life Sci* 55: 494-505, 1999.

231. **Usyk TP, LeGrice IJ, and McCulloch AD.** Computational model of three dimensional cardiac electromechanics. *Comp Visual Sci* 4: 249-257, 2002.

232. **Usyk TP and McCulloch AD.** Electromechanical model of cardiac resynchronization in the dilated failing heart with left bundle branch block. *Journal of Electrocardiology* 36: 57-61, 2003.

233. **Valdivia CR, Chu WW, Pu J, Foell JD, Haworth RA, Wolff MR, Kamp TJ, and Makielski JC.** Increased late sodium current in myocytes from a canine heart failure model and from failing human heart. *J Mol Cell Cardiol* 38: 475-483, 2005.

234. **van Bemmelen MX, Rougier JS, Gavillet B, Apotheloz F, Daidie D, Tateyama M, Rivolta I, Thomas MA, Kass RS, Staub O, and Abriel H.** Cardiac voltage-gated sodium channel Nav1.5 is regulated by Nedd4-2 mediated ubiquitination. *Circ Res* 95: 284-291, 2004.

235. **van Capelle FJ and Durrer D.** Computer simulation of arrhythmias in a network of coupled excitable elements. *Circulation Research* 47: 454-466, 1980.

236. **Verrier RL and Antzelevitch C.** Autonomic aspects of arrhythmogenesis: the enduring and the new. *Curr Opin Cardiol* 19: 2-11, 2004.

237. **Vetter FJ and McCulloch AD.** Three-dimensional analysis of regional cardiac function: a model of rabbit ventricular anatomy. *Progress in Biophysics & Molecular Biology* 69: 157-183, 1998.

238. **Viskin S, Alla SR, Barron HV, Heller K, Saxon L, Kitzis I, Hare GF, Wong MJ, Lesh MD, and Scheinman MM.** Mode of onset of torsade de pointes in congenital long QT syndrome. *J Am Coll Cardiol* 28: 1262-1268, 1996.

239. **Viswanathan PC and Rudy Y.** Cellular Arrhythmogenic Effects of Congenital and Acquired Long-QT Syndrome in the Heterogeneous Myocardium. *Circulation* 101: 1192-1198, 2000.

240. **Viswanathan PC and Rudy Y.** Pause induced early afterdepolarizations in the long QT syndrome: a simulation study. *Cardiovascular Research* 42: 530-542, 1999.

241. **Volders PG, Kulcsar A, Vos MA, Sipido KR, Wellens HJ, Lazzara R, and Szabo B.** Similarities between early and delayed afterdepolarizations induced by isoproterenol in canine ventricular myocytes. *Cardiovasc Res* 34: 348-359, 1997.

242. **Volders PG, Sipido KR, Carmeliet E, Spatjens RL, Wellens HJ, and Vos MA.** Repolarizing K+ currents ITO1 and IKs are larger in right than left canine ventricular midmyocardium. *Circulation* 99: 206-210, 1999.

243. **Vracko R, Thorning D, and Frederickson RG.** Nerve fibers in human myocardial scars. *Hum Pathol* 22: 138-146, 1991.

244. **Walker JC, Ratcliffe MB, Zhang P, Wallace AW, Fata B, Hsu EW, Saloner D, and Guccione JM.** MRI-based finite-element analysis of left ventricular aneurysm. *American Journal of Physiology-Heart and Circulatory Physiology* 289: H692-H700, 2005.

245. **Walsh KB and Kass RS.** Distinct voltage-dependent regulation of a heart-delayed IK by protein kinases A and C. *Am J Physiol* 261: C1081-1090, 1991.

246. **Wan X, Laurita KR, Pruvot EJ, and Rosenbaum DS.** Molecular correlates of repolarization alternans in cardiac myocytes. *J Mol Cell Cardiol* 39: 419-428, 2005.

247. **Wang DW, Yazawa K, George AL, Jr., and Bennett PB.** Characterization of human cardiac Na+ channel mutations in the congenital long QT syndrome. *Proc Natl Acad Sci U S A* 93: 13200-13205, 1996.

248. **Wei J, Wang DW, Alings M, Fish F, Wathen M, Roden DM, and George AL, Jr.** Congenital long-QT syndrome caused by a novel mutation in a conserved acidic domain of the cardiac Na+ channel. *Circulation* 99: 3165-3171, 1999.

249. **Weidmann S.** Effect of current flow on the membrane potential of cardiac muscle. *J Physiol* 115: 227-236, 1951.

250. **Winslow RL, Rice J, Jafri S, Marban E, and O'Rourke B.** Mechanisms of altered excitation-contraction coupling in canine tachycardia-induced heart failure, II : model studies. *Circ Res* 84: 571-586, 1999.

251. **Wolk R, Cobbe SM, Hicks MN, and Kane KA.** Functional, structural, and dynamic basis of electrical heterogeneity in healthy and diseased cardiac muscle: implications for arrhythmogenesis and anti-arrhythmic drug therapy. *Pharmacology & Therapeutics* 84: 207-231, 1999.

252. **Wong KR, Trezise AE, Bryant S, Hart G, and Vandenberg JI.** Molecular and functional distributions of chloride conductances in rabbit ventricle. *Am J Physiol* 277: H1403-1409, 1999.

253. **Xia L, Huo MM, Wei Q, Liu F, and Crozier S.** Analysis of cardiac ventricular wall motion based on a three.-dimensional electromechanical biventricular model. *Physics in Medicine and Biology* 50: 1901-1917, 2005.

254. **Xie F, Qu Z, Yang J, Baher A, Weiss JN, and Garfinkel A.** A simulation study of the effects of cardiac anatomy in ventricular fibrillation. *J Clin Invest* 113: 686-693, 2004.

255. **Xiong W, Tian Y, DiSilvestre D, and Tomaselli GF.** Transmural heterogeneity of Na+-Ca2+ exchange: evidence for differential expression in normal and failing hearts. *Circ Res* 97: 207-209, 2005.

256. **Xu X, Rials SJ, Wu Y, Salata JJ, Liu T, Bharucha DB, Marinchak RA, and Kowey PR.** Left ventricular hypertrophy decreases slowly but not rapidly activating delayed rectifier potassium currents of epicardial and endocardial myocytes in rabbits. *Circulation* 103: 1585-1590, 2001.

257. **Yamada KA, Kanter EM, Green KG, and Saffitz JE.** Transmural distribution of connexins in rodent hearts. *J Cardiovasc Electrophysiol* 15: 710-715, 2004.

258. **Yan GX and Antzelevitch C.** Cellular basis for the electrocardiographic J wave. *Circulation* 93: 372-379, 1996.

259. **Yan GX and Antzelevitch C.** Cellular basis for the normal T wave and the electrocardiographic manifestations of the long-QT syndrome. *Circulation* 98: 1928-1936, 1998.

260. **Yan GX, Rials SJ, Wu Y, Liu T, Xu X, Marinchak RA, and Kowey PR.** Ventricular hypertrophy amplifies transmural repolarization dispersion and induces early afterdepolarization. *Am J Physiol Heart Circ Physiol* 281: H1968-1975, 2001.

261. **Yan GX, Shimizu W, and Antzelevitch C.** Characteristics and distribution of M cells in arterially perfused canine left ventricular wedge preparations. *Circulation* 98: 1921-1927, 1998.

262. **Yan G-X, Wu Y, Liu T, Wang J, Marinchak RA, and Kowey PR.** Phase 2 Early Afterdepolarization as a Trigger of Polymorphic Ventricular Tachycardia in Acquired Long-QT Syndrome : Direct Evidence From Intracellular Recordings in the Intact Left Ventricular Wall. *Circulation* 103: 2851-2856, 2001.

263. **Yarbrough TL, Lu T, Lee HC, and Shibata EF.** Localization of cardiac sodium channels in caveolin-rich membrane domains: regulation of sodium current amplitude. *Circ Res* 90: 443-449, 2002.

264. **Zhang C, Xu D, Li Y, Liu N, Wang L, and Lu Z.** Effect of autonomic nervous system on the transmural dispersion of ventricular repolarization in intact canine. *J Huazhong Univ Sci Technolog Med Sci* 24: 37-40, 2004.

265. **Zhang M, Jiang M, and Tseng GN.** minK-related peptide 1 associates with Kv4.2 and modulates its gating function: potential role as beta subunit of cardiac transient outward channel? *Circ Res* 88: 1012-1019, 2001.

266. **Zhou J, Yi J, Hu N, George AL, Jr., and Murray KT.** Activation of protein kinase A modulates trafficking of the human cardiac sodium channel in Xenopus oocytes. *Circ Res* 87: 33-38, 2000.

267. **Zhou S, Chen LS, Miyauchi Y, Miyauchi M, Kar S, Kangavari S, Fishbein MC, Sharifi B, and Chen PS.** Mechanisms of cardiac nerve sprouting after myocardial infarction in dogs. *Circ Res* 95: 76-83, 2004.

268. **Zhou W, Qian Y, Kunjilwar K, Pfaffinger PJ, and Choe S.** Structural insights into the functional interaction of KChIP1 with Shal-type K(+) channels. *Neuron* 41: 573-586, 2004.

269. **Zicha S, Xiao L, Stafford S, Cha TJ, Han W, Varro A, and Nattel S.** Transmural expression of transient outward potassium current subunits in normal and failing canine and human hearts. *J Physiol* 561: 735-748, 2004.

270. **Zilberter Yu I, Starmer CF, Starobin J, and Grant AO.** Late Na channels in cardiac cells: the physiological role of background Na channels. *Biophys J* 67: 153-160, 1994.

271. **Zipes DP.** Influence of myocardial ischemia and infarction on autonomic innervation of heart. *Circulation* 82: 1095-1105, 1990.

272. **Zygmunt AC.** Intracellular calcium activates a chloride current in canine ventricular myocytes. *Am J Physiol* 267: H1984-1995, 1994.

273. **Zygmunt AC, Eddlestone GT, Thomas GP, Nesterenko VV, and Antzelevitch C.** Larger late sodium conductance in M cells contributes to electrical heterogeneity in canine ventricle. *Am J Physiol Heart Circ Physiol* 281: H689-697, 2001.

274. **Zygmunt AC, Goodrow RJ, and Antzelevitch C.** I(NaCa) contributes to electrical heterogeneity within the canine ventricle. *Am J Physiol Heart Circ Physiol* 278: H1671-1678, 2000.